TÉCNICO LISBOA

Stability analysis and impedance-based representation of VSC

Yeonjoong Kim

Thesis to obtain the Master of Science Degree in

Energy Engineering and Management

Supervisors: Prof. Gil Domingos Marques
Prof. Marc Cheah Mañé

Examination Committee

Chairperson: Prof. Duarte de Mesquita e Sousa
Supervisor: Prof. Marc Cheah Mañé
Member of the Committee: Prof. Victor Manuel de Carvalho Fernão Pires

December 2021

Acknowledgments

First, I would like to express my gratitude to supervisor Dr. Gil Domingos Marques, the professor in the department of Electrical and Computer Engineering of *Instituto Superior Técnico* (IST) and researcher in *INESC-ID*, for granting the opportunity to write my master thesis in IST and for his supervision of the contents as well as helping to comply with the qualification by IST.

Next, I would like to express my sincere thanks to Dr. Oriol Gomis-Bellmunt, the professor in the department of Electrical Engineering of *Universitat Politècnica de Catalunya* (UPC) and researcher in *CITCEA-UPC*, who willingly allowed me to be guided the master thesis at the prestigious research center CITCEA-UPC and contributed greatly to materializing the topic.

Above all, I would like to give my highest praise to my supervisor Dr. Marc Cheah Mañe, the researcher and lecturer in the department of Electrical Engineering UPC and researcher in *CITCEA-UPC*, who must have had a lot of difficulties in directing the thesis remotely. He dedicatedly had done his best to guide the thesis, providing materials needed and instructing technical knowledge as well as thesis writing, from the start to the end.

Furthermore, I appreciate to the examination committee who participated in the discussion for the thesis defense. It was an great honor to be with Dr. Duarte de Mesquita e Sousa, the professor in the department of Electrical and Computer Engineering of *Instituto Superior Técnico* (IST) who presided the discussion, and Dr. Victor Manuel de Carvalho Fernão Pires, the professor in the department of Electrical Engineering of *Instituto Politécnico de Setúbal* who participated as a member of committee, at the end of my master program.

Lastly, I am very grateful to Dr. Hasan Mehrjerdi, the professor in the department of Electrical Engineering of *the college of Engineering, Qatar University*, who provided the basis for writing the thesis through the funding of the project for this topic.

(English)

Abstract

As high levels of power electronics are integrated into the power grid, referred to as Inverter-based resources (IBRs), the importance of controlling the small-signal stability of the grid system is becoming more important and complex caused by the widen control frequency range.

The main purpose of the thesis is to present the design of the grid-connected voltage source converter (VSC) in $MATLAB/Simulink$ and how its operating conditions affect the grid stability and impedance responses.

The key result includes the validation of the linearized state-space model (SSM), its response under changes of each parameter, and its impedance representation.

Keywords

Voltage Source Converter, Grid Stability, Eigenvalue analysis, d-q Impedance

(Portuguese)

Resumo

À medida que altos níveis de eletrônica de potência são integrados na rede elétrica, conhecidos como recursos baseados em inversores (IBRs), a importância do estudo da estabilidade de rede através de pequenos sinais está a tornar-se mais importante e complexa, dada a ampla faixa de frequência de controlo.

O objetivo principal da tese é apresentar o projeto do conversor da fonte de tensão conectado à rede (VSC) em $MATLAB/Simulink$ e de como as suas condições de operação afetam a estabilidade da rede e as respostas de impedância.

O principal resultado inclui a validação do modelo de espaço de estados linearizado (SSM), a sua resposta às mudanças de cada parâmetro e sua representação de impedância.

Palavras-chave

Conversor de fonte de tensão, estabilidade da rede, análise de valores próprios, impedância d-q

Table of Contents

ACKNOWLEDGMENTS **1**

ABSTRACT **2**

KEYWORDS **2**

LIST OF FIGURES **5**

ABBREVIATION **7**

1. INTRODUCTION **8**

1.1 Energy Industry as Background 8

1.2 Statement of the Problems 9

1.3 Approach 9

1.4 Thesis outline 9

2. LITERATURE REVIEW OF POWER ELECTRONICS AND STABILITY ANALYSIS **10**

2.1 State of-the-art power electronics technologies 10

2.1.1 Application of power electronics in Microgrid 10

2.1.2 Application of power electronics in transmission grids 10

2.2 Power System Stability Analysis 12

2.2.1 Power system stability problem 12

2.2.2 Impedance-based small-signal stability analysis 13

3. NON-LINEAR MODEL OF VSC CONTROLLER **14**

3.1 Instantaneous Power Theory 14

3.2 Grid modeling 16

3.3 Design of the non-linear model 17

3.3.1 Phase Locked Loop (PLL) 17

3.3.2 Grid-connected VSC with inductive filtering components 18

3.3.3 Current Controller 21

3.4 Operation mode for VSC Control 23

3.4.1 $\boldsymbol{P} - \boldsymbol{Q}$ Mode 24

3.4.2 $\boldsymbol{V_{DC}} - \boldsymbol{Q}$ Mode 25

3.5 Non-linear model in $MATLAB/imulink$ 27

4. LINEAR MODEL OF THE VSC CONTROLLER **29**

4.1 Linearization Process 29

4.2 State-space 31

4.3 Eigenvectors and Modal matrices 32

4.4 Design of the linear model 33

4.4.1 Phase Locked Loop (PLL) 33

4.4.2 Inner Current Controller (IC) 33

4.4.3 Grid-connected VSC with inductive filtering components 34

4.4.4 Angle rotation between the grid and the converter 35

4.4.5 AC/DC Bus 36

4.4.6 VSC Control Mode for Reference Calculation 36

4.5 Linear model in $MATLAB/Simulink$ 38

4.6 Validation of the Linear VSC models 39

5. CASE STUDIES AND COMPARISON **42**

5.1 CHANGES IN CONTROL PARAMETERS 43
5.1.1 Variation of Short Circuit Power S_{SC} 43
5.1.2 Variation of Current Controller – Time Constant τ_{ic} 44
5.1.3 Variation of Grid Nominal Frequency ω_n 45
5.1.4 Variation of DC Voltage Controller – Frequency ω_V 46
5.1.5 Variation of Phase Locked Loop – Damping Ratio ξ_{PLL} 47
5.1.6 Variation of DC Voltage Controller – Damping Ratio ξ_V 48
5.2 EIGENVALUE ANALYSIS 49
5.2.1 S_{SC} Variation 50
5.2.2 τ_{ic} Variation 51
5.2.3 ω_n Variation 52
5.2.4 ω_V Variation 53
5.2.5 ξ_{PLL} Variation 54
5.2.6 ξ_V Variation 55
5.3 BODE PLOT ANALYSIS 56
5.3.1 S_{SC} Variation 57
5.3.2 τ_{ic} Variation 58
5.3.3 ω_n Variation 59
5.3.4 ω_V Variation 60
5.3.5 ξ_{PLL} Variation 61
5.3.6 ξ_V Variation 62
6. CONCLUSION 63
6.1 REVIEW OF THE CASE STUDIES 63
6.2 COMPLETION AND DISCUSSION 63
BIBLIOGRAPHY 65
APPENDIX 67
1 CLARKE TRANSFORMATION 67
2 PARK TRANSFORMATION 69

List of Figures

FIGURE 1 SOLAR PV & WIND, YOY ADDITIONS % RATE AND THE TOTAL CUMULATIVE CAPACITY IN GW 8
FIGURE 2 AN EXAMPLE OF HYBRID AC/DC MICROGRID WITH GENERATION AND STORAGE SYSTEMS 10
FIGURE 3 COMPARISON OF LCC AND VSC 11
FIGURE 4 THE HISTORY OF POWER SYSTEM STABILITY PROBLEMS 12
FIGURE 5 CLASSIFICATION OF POWER SYSTEM STABILITY PROBLEM 12
FIGURE 6 NEW STABILITY PROBLEMS IN POWER SYSTEM 13
FIGURE 7 THE THREE-PHASE 3-WIRED GRID-CONNECTED 2-LEVEL VSC 16
FIGURE 8 PLL - IMPLEMENTATION STRUCTURE 17
FIGURE 9 PLL - DESIGN STRUCTURE OF THE CLOSED LOOP SYSTEM 17
FIGURE 10 EQUIVALENT MODEL OF THE AC SIDE OF VSC 18
FIGURE 11 ELECTRICAL CIRCUIT OF THE EQUIVALENT MODEL 19
FIGURE 12 INNER CURRENT CONTROL LOOP - IMPLEMENTATION STRUCTURE 22
FIGURE 13 INNER CURRENT CONTROL LOOP - DESIGN STRUCTURE 22
FIGURE 14 MODES OF VSC OPERATION 23
FIGURE 15 GENERAL SCHEME OF THE GRID-CONNECTED VSC CONTROLLER IN $\boldsymbol{P-Q}$ OPERATION MODE 24
FIGURE 16 GENERAL SCHEME OF THE GRID-CONNECTED VSC CONTROLLER IN $\boldsymbol{V_{DC}-Q}$ OPERATION MODE 25
FIGURE 17 OUTER VOLTAGE CONTROL LOOP - IMPLEMENTATION STRUCTURE 25
FIGURE 18 OUTER VOLTAGE CONTROL LOOP - DESIGN STRUCTURE 26
FIGURE 19 NON-LINEAR MODEL WITH $\boldsymbol{P-Q}$ OPERATION MODE 27
FIGURE 20 NON-LINEAR MODEL WITH $\boldsymbol{V_{DC}-Q}$ OPERATION MODE 28
FIGURE 21 PROCEDURE OF OBTAINING INITIAL VALUE AT THE LINEARIZATION POINT 29
FIGURE 22 PLL - STATE-SPACE BLOCK 33
FIGURE 23 INNER CURRENT CONTROL LOOP – STATE-SPACE BLOCK 34
FIGURE 24 GRID-VSC CONNECTED L-FILTER – STATE-SPACE BLOCK 34
FIGURE 25 ANGLE ROTATION OF THE CONVERTER VOLTAGE – STATE-SPACE BLOCK 35
FIGURE 26 ANGLE ROTATION OF THE GRID VOLTAGE – STATE-SPACE BLOCK 35
FIGURE 27 ANGLE ROTATION OF THE GRID CURRENT – STATE-SPACE BLOCK 36
FIGURE 28 AC/DC BUS – STATE-SPACE BLOCK 36
FIGURE 29 $\boldsymbol{P-Q}$ OPERATION MODE - FEEDFORWARD IMPLEMENTATION STRUCTURE 37
FIGURE 30 $\boldsymbol{V_{DC}-Q}$ OPERATION MODE - STATE-SPACE BLOCK 37
FIGURE 31 LINEAR MODEL WITH $\boldsymbol{P-Q}$ OPERATION MODE 38
FIGURE 32 LINEAR MODEL WITH $\boldsymbol{V_{DC}-Q}$ OPERATION MODE 38
FIGURE 33 SIMULATION RESULTS OF THE CURRENTS $-\boldsymbol{i_q^c}$ 39
FIGURE 34 SIMULATION RESULTS OF THE CURRENTS $-\boldsymbol{i_d^c}$ 39
FIGURE 35 SIMULATION RESULTS OF THE CURRENT CONTROLLER INPUT VOLTAGE $-\boldsymbol{u_q^{cc}}$ 39
FIGURE 36 SIMULATION RESULTS OF THE CURRENT CONTROLLER INPUT VOLTAGE $-\boldsymbol{u_d^{cc}}$ 40
FIGURE 37 SIMULATION RESULTS OF THE CURRENT CONTROLLER OUTPUT VOLTAGE $-\boldsymbol{v_q^{cc}}$ 40
FIGURE 38 SIMULATION RESULTS OF THE CURRENT CONTROLLER OUTPUT VOLTAGE $-\boldsymbol{v_d^{cc}}$ 40
FIGURE 39 SIMULATION RESULTS OF THE CURRENT CONTROLLER OUTPUT VOLTAGE $-\boldsymbol{V_{DC}}$ 40
FIGURE 40 SIMULATION RESULTS OF THE CURRENT CONTROLLER OUTPUT VOLTAGE $-\boldsymbol{I_{DC_l}}$ 41
FIGURE 41 EFFECTS OF INCREASING GAINS OF PID CONTROL INDEPENDENTLY 42
FIGURE 42 THE CASE OF $\boldsymbol{S_{SC}}$ VARIATION 43
FIGURE 43 THE CASE OF $\boldsymbol{\tau_{ic}}$ VARIATION 44
FIGURE 44 THE CASE OF $\boldsymbol{\omega_n}$ VARIATION 45
FIGURE 45 THE CASE OF $\boldsymbol{\omega_V}$ VARIATION 46

FIGURE 46 THE CASE OF ξ_{PLL} VARIATION 47
FIGURE 47 THE CASE OF ξ_V VARIATION 48
FIGURE 48 STEP RESPONSE OF A SECOND-ORDER SYSTEM 49
FIGURE 49 STATE-SPACE VARIABLES FOR EIGENVALUE ANALYSIS 49
FIGURE 50 EIGENVALUE - S_{SC} VARIATION 50
FIGURE 51 EIGENVALUE - τ_{ic} VARIATION 51
FIGURE 52 EIGENVALUE - ω_n VARIATION 52
FIGURE 53 EIGENVALUE - ω_V VARIATION 53
FIGURE 54 EIGENVALUE - ξ_{PLL} VARIATION 54
FIGURE 55 EIGENVALUE - ξ_V VARIATION 55
FIGURE 56 BODE PLOT - S_{SC} VARIATION 57
FIGURE 57 BODE PLOT - τ_{ic} VARIATION 58
FIGURE 58 BODE PLOT - ω_n VARIATION 59
FIGURE 59 BODE PLOT - ω_V VARIATION 60
FIGURE 60 BODE PLOT - ξ_{PLL} VARIATION 61
FIGURE 61 BODE PLOT - ξ_V VARIATION 62
FIGURE 62 CLARKE TRANSFORMATION 67
FIGURE 63 THE BALANCED THREE-PHASE SYSTEM 67
FIGURE 64 CLARKE TRANSFORMATION OF THE BALANCED THREE-PHASE SYSTEM 68
FIGURE 65 PARK TRANSFORMATION BY q −AXIS ALIGNMENT 69
FIGURE 66 TRANSFORMATION BY $T(\theta)$ OF THE BALANCED THREE-PHASE SYSTEM 70

Abbreviation

AC	Alternating Current
CHIL	Controller Hardware In Loop
DC	Direct Current
DRE	Distributed Energy Resources
DSO	Distribution System Operators
EMI	Electro-Magnetic Interference
EMT	Electromagnetic Transient model
EV	Electric Vehicle
FC	Flying Capacitor
GSC	Grid Side Converter
GTO	Gate Turn-Off thyristor
HVAC	High Voltage Alternating Current
HVDC	High Voltage Direct Current
IBRs	Inverter-Based Resources
IGBT	Isolated Gate Bipolar Transistor
IGCT	Integrated Gate Commutated Thyristor
LCC	Line Commutated Converter
LTI	Linear Time-Invariant
MMC	Modular Multilevel Converters
MOSFET	Metal-Oxide Semiconductor Field-Effect Transistor
MSC	Machine Side Converter
NPC	Neutral Point Clamped
POC	Point of Common Coupling
PWM	Pulse Width Modulation
qd0	Quadrature–Direct–Zero
SCC	Short Circuit Capacity
SCR	Short Circuit Ratio
SSM	State-Space Model
SSO	Sub-Synchronous Oscillation
TSO	Transmission System Operators
VRE	Variable Renewable Energy
VSC	Voltage Source Converter
YoY	Year on Year

1. Introduction

1.1 Energy Industry as Background

The recent transition of the electrical power system from fossil fuel-base to the integration of variable renewable energy (VRE) such as solar and wind has required an evolution in the power system to support variability and uncertainty. In addition, a future grid, or a smart grid, in other words, enabling the implementation of a distributional and multi-directional energy sharing grid, requires more interconnection of high-performance power electronics for enabling power transformation and conversion.

Since most countries have set ambitious goals to scale up renewable energy in their energy mix to meet individual national strategy as well as to comply with the Paris agreement treating climate change. **Figure 1** represents the Year-on-Year (YoY) and the total installed capacity of Solar PV and Wind over the past decade.

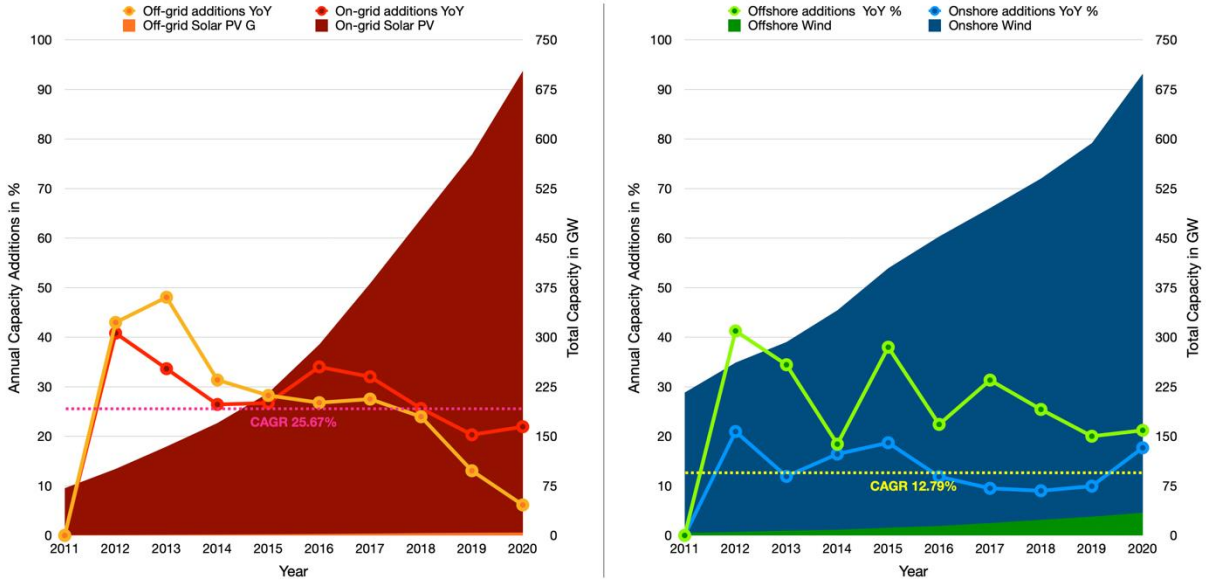

FIGURE 1 SOLAR PV & WIND, YOY ADDITIONS % RATE AND THE TOTAL CUMULATIVE CAPACITY IN GW [1]

In **Figure 1**, the global generation capacity of grid-connected solar PV and wind has been on a significant rise over the last decade. The dominating on-grid solar PV compared to off-grid solar PV and the increase in the offshore wind represents larger scales of VREs are preferred in the renewable energy market, proving both technological and economic feasibility.

Full-scale, bidirectional voltage source converter (VSC) has emerged as the key element to penetrate VRE into grid [2,3] in that they allow the improvement on the generation efficiency of VRE as well as the support for grid health with grid-forming capability. Nowadays, with the help of versatility, VSC is widely applied in microgrid interconnecting not only VRE generations but also energy storage systems (ESS) or backup generation systems, such as pumped-storage or gas turbine, to cover the intermittence and enhance the capacity factor, typically 15% in solar PV and 20 percent in wind, of VRE generation.

1.2 Statement of the Problems

Such an increasing number of utility-scale VRE power plants has brought about new kinds of risks on the power system stability accompanied by much more complexities in analysis. The reason is that high levels of power electronics have adopted operation frequency ranging widely from a couple of Hz to tens of kHz which makes complex dynamic behavior. Also, most power electronics manufacturers, who are unwilling to share internal designs of their products to the public, only supply the black-box Electromagnetic Transient (EMT) models, which have clear limits on resolving the stability of modern grid [4]. For these reasons, transmission system operators (TSO) and distribution system operators (DSO) have difficulties in system operation, predicting and responding to the system malfunction, possibly leaded to black-out.

1.3 Approach

The objective of the thesis is to analyze stability and characterize the impedance-based representation of the average model of two-level full-bridge VSC connected to a grid with the consideration of its internal dynamics and impact on the grid.

1.4 Thesis outline

The outline of the thesis is organized as follows.

I. The introduction presents the new stability issues in the power industry with energy transition as background information.
II. The literature review focuses on the state-of-the-art of a VSC, which is considered to have a key role in the present and future power grids. In addition, the new stability problems and studied methodologies presented to solve them are reviewed to find the significance of the thesis.
III. The next step is to develop the theoretical basis for the design of the non-linear model of the VSC and the linear model through the linearization from the former model. The validation of the linearization process in the simulation interval is necessarily included.
IV. For case studies, the changes in operating conditions are observed according to variations of state variables. Moreover, the bode plots of transfer functions of impedances, or admittances, as well as eigenvalue analysis are investigated to check how each variable affects the impedances and the stability of the system.
V. Lastly, the conclusion summarizes the simulation results and the recommendations for further development are to be stated.

2. Literature Review of Power electronics and Stability Analysis

2.1 State-of-the-art power electronics technologies

2.1.1 Application of power electronics in microgrid

The utilization of distributed energy resources (DRE) has given rise to the change of a classical centralized power generation system into a distributed power generation system, accompanied by the need for power converters to effectively integrate a DC system into an AC system. Power electronics, represented by inverters and converters, have successfully realized the integration between the AC and the DC grid, as shown in **Figure 2**.

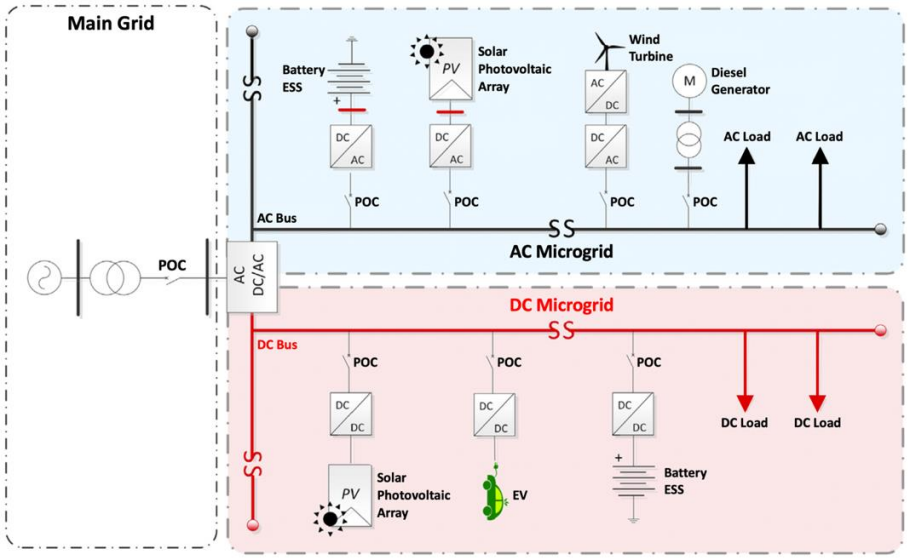

FIGURE 2 AN EXAMPLE OF HYBRID AC/DC MICROGRID WITH GENERATION AND STORAGE SYSTEMS [5]

For instance, according to 'IEC 61400-27-1' , the type-4 wind turbine requires a pair of an AC-DC converter and a DC-AC inverter for the control of active and reactive power, to extract optimum power and exchange appropriate reactive power with the grid. Since Solar PVs and hydrogen fuel cells generate DC voltage, DC-AC inverters are needed when they directly inject power into the AC grid. Similarly, the energy storage systems consisting of electrical battery cells also require bidirectional converters, either AC/DC or DC/DC, to charge batteries or inject power to the grid, while most electric vehicle (EV) charge stations need unidirectional converters with adequate DC voltage output.

2.1.2 Application of power electronics in transmission grids

Not only for the AC/DC power conversion in microgrids but converter technology is also applied in transmission systems. Regarding the kind of semiconductors, the comparison of the characteristics of the classical Line-Commutated Converter (LCC) system and the VSC system is shown in **Figure 3**.

	LCC	VSC
Types of switches	Thyristor, Line-commutated	GTO, MOSFET, IGBT, IGCT, Self-commutated
Control	Switch turn ON only, current control	Gate turn ON and OFF, voltage control
DC Voltage	±800 kV, the Max. recorded ±1100kV	±500 kV, Mostly ±320 kV
Station size	Large	Small, around 50% of LCC

Overloading capability	Small, A bit higher than VSC	Small, semiconductor physics
Active and reactive power control	Active power dependent, LCC consumes as much as 50~60% reactive power of transmitted active power.	Independent, Active and reactive power are independently controlled.
Converter / System loss	Low, low switching frequency ~0.8% / 2.5~4.5%	High, higher switching frequency ~1.6% / 4 ~6 %
Power flow	Yes, slow, Reversing polarity	Yes, fast, w/o reversing polarity
AC Fault-Ride through	No, or limitedly available	Yes, Excellent and fast
Black start capability	No, or limited capability, Always the minimum of 3% of power rating required.	Yes, fully capable, No minimum power is required.
Harmonic generation	High, AC and DC harmonic filters needed	Low, Minimal filters needed
AC filter	Yes, Filtering Reactor and shunt capacitor	No, (with MMC type) or only minimal filtering required.
DC filter	Yes, Smoothing reactor + DC-filter	Yes, DC capacitor (optional)
Connection to AC grid	Converter + Transformer	Series reactor + Transformer
AC system strength	Strong $SCR \geq 2$	Weak or black AC $SCR \approx 0$
DC grid applicability	Possible but very limited	Yes
Rated power of a single level converter	Very high, Up to 12000 MW	Moderate, From 50 to 2500 MW
Multi-terminal configuration	Complex, Limited to 3 terminals	Simple, No limitation
Transmission Length	Long-range, Average 1650 km, Max. 3300 km	Medium range, Average 200 ~ 500 km

FIGURE 3 COMPARISON OF LCC AND VSC [6,7]

Each converter topology has clear advantages and disadvantages and there exist some investigations on the hybrid of LCC and VSC systems [8]. However, when it comes to the formation of DC microgrid or the transmission system for offshore wind turbines, VSC has recently been in very preference due to the following reasons:

- Control of voltage depending on the application where it is connected
- Independent active and reactive power control
- Black-start capability to support grid-forming
- Bidirectional power flow without reversing the polarity
- Reduced size of filters compared to other converter technologies

VSC can be classified referring to the number of levels. The most common topology is a two-level VSC usually applied in low voltage. However, in high voltage, a multi-level VSC is used for the following reasons:

- To avoid or minimize the use of series and parallel connected semiconductors
- Applying several voltage levels on the AC side to lower harmonic
- Allow lower switching frequency
- Lower dv/dt, lower Electro-Magnetic Interference (EMI).

Depending on the arrangement and the connection point of semiconductors, Multilevel converters can be classified into three types; Neutral Point Clamped (NPC) and Flying Capacitor (FC), and Modular Multilevel Converters (MMC).

2.2 Power System Stability Analysis

2.2.1 Power system stability problem

The whole history of power system stability problems since its first recognition in 1920 and several cases of studies to figure out problems at those periods are shown in **Figure 4**.

- The first recognition of the **power system stability problems** in the 1920s.	Steinmetz, 1920; Evans and Bergvall, 1924; Wilkins, 1926;
v	
- **Frequency stability problems** had been reported in the 1970s and 1980s. - The development of the modal analysis techniques such as *eigenvalue analysis*.	Martins, 1986; Kundur et al., 1990
- The development of the *long-term dynamic simulation.*	Davidson et al., 1975; Converti et al., 1976; Ontario Hydro, 1989; Stubbe et al., 1989; Inoue et al., 1995
v	
- **Voltage instability** has emerged as a significant concern to collapse several power systems since the late 1970s.	IEEE, 1990; Kundur, 1994; Taylor, 1994
- Increasing address of voltage stability in system planning and operation, with powerful analytical tools.	Gao et al., 1992; Morison et al., 1993
v	
- **Dynamic characteristics of modern power systems**, particularly wind. - To satisfy ride-through capability - Operation of systems under **extremely stressed conditions**, due to the competition of power electronics manufacturers.	At present

FIGURE 4 THE HISTORY OF POWER SYSTEM STABILITY PROBLEMS [9]

Figure 5 shows the overall classification of the power system stability problems. Different from the traditional classification, two subclasses of 'Resonance stability' and 'Converter-driven stability' are added to deal with the use of converter-integrated generation systems, to extend the frequency scale of interest.

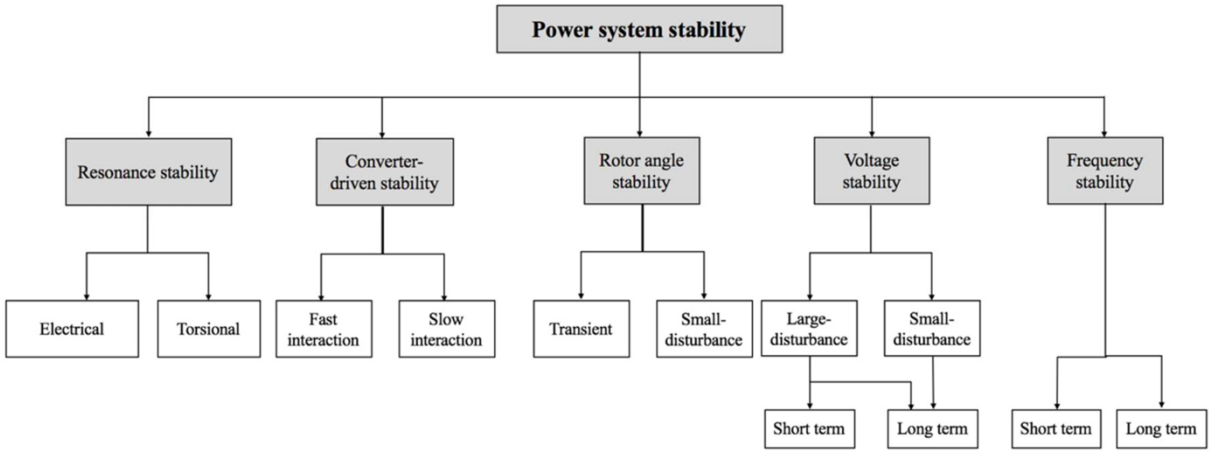

FIGURE 5 CLASSIFICATION OF POWER SYSTEM STABILITY PROBLEM [10]

In recent years, the industry has shifted its effort and attention from transient to small-signal stability issue which has emerged as much more critical, primarily to address the modern trend of high levels of Inverter-Based Resources (IBRs) in a power grid [11,12] for following reasons:

- Large-scale system interconnection
- Extensive operation closer to transmission limits
- Interconnection of new generation techniques such as wind and solar
- Changing load characteristics
- Regulatory requirements for enforcing small-signal stability criteria

In detail, the instability caused by controller is classified into, depending on the frequency domain, sub-synchronous resonance, near-synchronous resonance, and super-synchronous resonance. The operation frequency band of each control technique is shown in **Figure 6**.

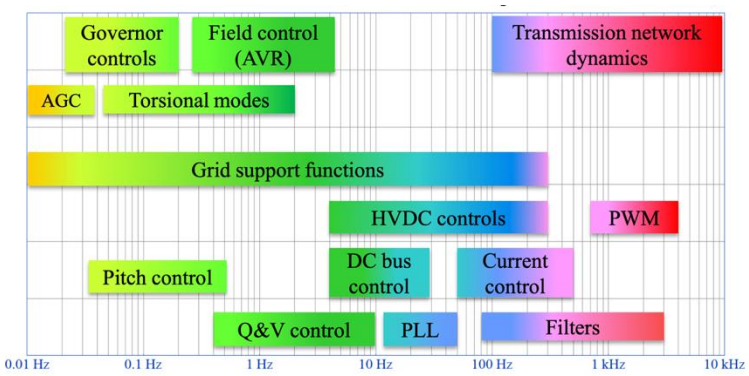

FIGURE 6 NEW STABILITY PROBLEMS IN POWER SYSTEM [13]

Considering that the frequency commercialized worldwide is either 50 or 60 Hz, near-synchronous resonance results from the interactions of relatively slower control loops such as $\boldsymbol{P-Q}$ and $\boldsymbol{V_{DC}-Q}$ power control, or the voltage magnitude and frequency at the point of interconnection. Furthermore, the connection of power electronics to a weak power grid which is referred to have low system strength and high grid impedance also increases the risk of near-synchronous resonance. On the other hand, super-synchronous resonance results from faster control loops such as current control loop and phase locked loop (PLL), PWM, and filter sizing, causing harmonic resonance issues.

2.2.2 Impedance-based small-signal stability analysis

Since the measurement of voltages and currents at desired points of systems is relatively easy, impedance-based analysis has advantages on data accessibility and does not necessarily require detailed design specifications of power electronics. For those who are not provided with such design specifications but need a stability analysis tool, impedance-based stability analysis is very practical and useful in the industry [14]. Since the first introduction of impedance-based modeling in 1976 by Prof. R.D. Middlebrook with the purpose to study dynamics of converter-based DC power supply and its source with filters [15], the attempts to adopt the impedance method to three-phase AC systems were made; d-q impedance method by M.Belkhayat in 1997 [16], sequence-impedance method by J.Sun in 2009 [17], and phasor impedance method by S.Shah in 2017 [18].

3. Non-linear model of VSC Controller

The modeling of VSC is performed with $MATLAB/Simulink$. For the simplification of the design, the following assumptions are made in the model design process:

I. Three-phase AC voltages of the grid and the PWM-modulated VSC are perfectly balanced, and identical to sinusoidal form through proper filtering.

II. The power exchanged with the AC side of VSC is equal to the power exchanged with the DC side of VSC, by ignoring any power loss in VSC.

III. A closed-loop dynamic function aims to obtain as close to the first-order response as possible. If the dynamic function is closer to second-order response, an overdamped response is prioritized, or at least, an underdamped response with $\xi > 1/\sqrt{2}$ is considered to limit the over peak.

IV. VSC follows a cascade control design so that the inner loop operates in at least ten times faster frequency than the outer loop.

V. The gain parameters of the VSC controller are expressed concerning model parameters and calculated by the control design tool of $MATLAB/Simulink$.

3.1 Instantaneous Power Theory

With the three-phase grid with three wires, the VSC is expected to be composed of three branches and a two-stage IGBT (Isolated Gate Bipolar Transistor). The generation or storage source could be connected to the DC side of the converter, which can be simply modeled as a DC voltage source, or as a current source with a shunt capacitor. The AC side can be modeled by the Thevenin equivalent model of the grid source or even more simplified as an AC voltage source with inductances which enables it to be considered as an AC source.

In the balanced three-phase system, the instantaneous voltage and current are expressed as

$$\begin{aligned} x_a(t) &= \sqrt{2}X\cos(\omega t + \phi) \\ x_b(t) &= \sqrt{2}X\cos\left(\omega t + \phi - \tfrac{2\pi}{3}\right) \\ x_c(t) &= \sqrt{2}X\cos\left(\omega t + \phi + \tfrac{2\pi}{3}\right) \end{aligned} \tag{1}$$

By the transformation of the sinusoidal signals in abc −frame to phasors in $\alpha\beta 0$ −frame, the three signals are expressed as

$$\begin{aligned} x_\alpha &= \sqrt{2}X\cos(\omega t + \phi) \\ x_\beta &= -\sqrt{2}X\cos(\omega t + \phi) \\ x_0 &= 0 \end{aligned} \tag{2}$$

Neglecting the zero components that are always 0 in the balanced three-phase system (2), the phasor representation of the rest two signals in $\alpha\beta$ are expressed as

$$\sqrt{2}\underline{V}_{\alpha\beta} = v_\alpha - jv_\beta \tag{3}$$

$$\sqrt{2}\underline{I}_{\alpha\beta} = i_\alpha - ji_\beta \tag{4}$$

the power expression of the three-phase system is given as

$$\underline{S} = P + jQ = 3\underline{V}_{\alpha\beta}\underline{I}^*_{\alpha\beta} = 3\left(\frac{v_\alpha - jv_\beta}{\sqrt{2}}\right)\left(\frac{i_\alpha + ji_\beta}{\sqrt{2}}\right) \tag{5}$$

When decoupling active and reactive power from (5), active and reactive power can be expressed as

$$P = \frac{3}{2}\left(v_\alpha i_\alpha + v_\beta i_\beta\right) \tag{6}$$

$$Q = \frac{3}{2}\left(v_\alpha i_\beta + v_\beta i_\alpha\right) \tag{7}$$

In the case of the Park transformation, the angle θ can be replaced to the electrical angle so that written as, $\theta = \omega t + \phi$. By voltage and current transformation to $qd0$ −frame, voltage and current phasers is defined, as like the case of the Clarke transformation, as

$$\underline{V}_{qd} = \frac{v_q - jv_d}{\sqrt{2}} \tag{8}$$

$$\underline{I}_{qd} = \frac{i_q - ji_d}{\sqrt{2}} \tag{9}$$

3.2 Grid modeling

The grid is represented by the Thevenin equivalent model, comprised of the voltage source and the impedances as shown in **Figure 7**.

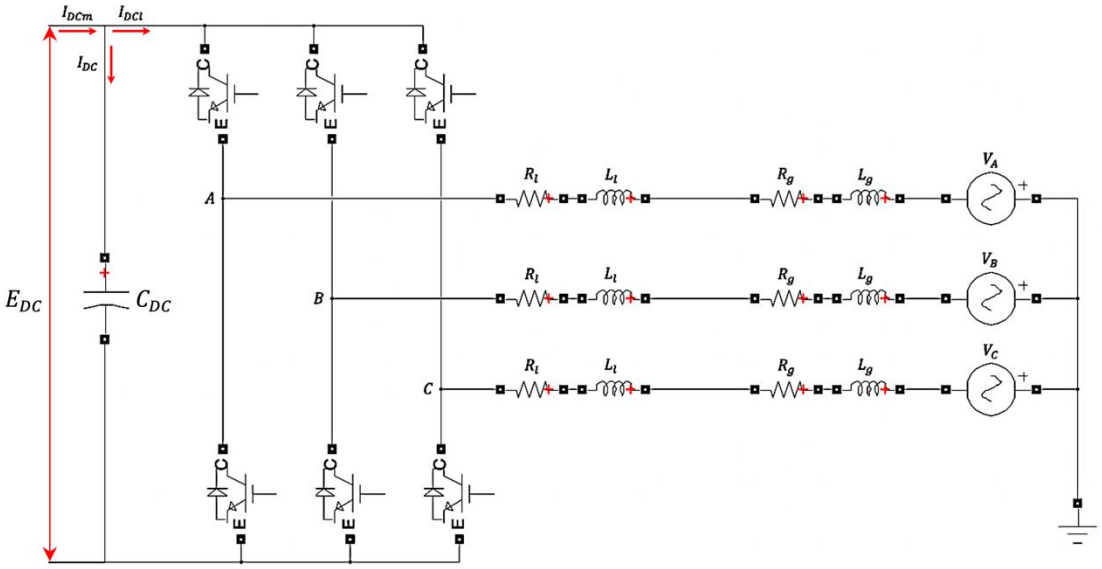

FIGURE 7 THE THREE-PHASE 3-WIRED GRID-CONNECTED 2-LEVEL VSC

To determine the voltage stiffness of the grid at the point of common coupling (POC), a classical three-phase fault analysis is to be performed. From the analysis, the short circuit current I_{SC} at the rated voltage of the system is calculated so that the short circuit power (S_{SC}), typically in MVA or KVA, is to be calculated as expressed in the following:

$$S_{SC} = E_{g_{RMS}}^{P-N} \cdot I_{SC} = \frac{E_{gRMS}^{P-N\ 2}}{Z_{SC}} = \frac{E_{gRMS}^{P-N\ 2}}{X_{L_g}} \tag{10}$$

where

V_{Rated}^{P-P} is the phase-to-phase rated voltage, I_{SC} is the short circuit current, and Z_{SC} is the short circuit impedance.

The grid impedance angle ratio seen at the POC bus is defined as

$$X_L/R\ ratio = \frac{X_L}{R_{POC}} = 10 \tag{11}$$

where

X_L and R_{POC} are the Thevenin equivalent of the reactance and the resistance at POC, respectively [19].

When applying to the grid modeling, the grid inductance L_g and the grid resistance R_g is expressed as

$$L_g = \frac{X_{L_g}}{2\pi f} = \frac{E_{gRMS}^{P-N\ 2}}{2\pi f \cdot S_{SC}} \tag{12}$$

$$R_g = \frac{1}{X_L/R\ ratio} \cdot X_{L_g} = \frac{1}{10} \cdot \frac{E_{gRMS}^{P-N\ 2}}{S_{SC}} \tag{13}$$

The other design parameters are $S_{SC} = 100\,kVA$, $E_{g_{RMS}}^{P-N} = 400\,V$, $R_L = 0.5\,\Omega$, $X_L = 5.4\,mH$, and $f = 50\,Hz$.

3.3 Design of the non-linear model

3.3.1 Phase Locked Loop (PLL)

The first step of the modeling is the Phase Locked Loop (PLL) that enables tracking the angle and the angular velocity of the grid for the synchronization of VSC to grid reference. With the input of the grid voltage in the $qd0$ frame, then the grid angle $\theta°$ is obtained as the output.

To obtain the grid voltage in the $qd0$ frame, the Park transformation is used which combines the Clarke transformation with an angle ($\theta°$) rotation. The constant variables in $qd0$ −rotating frame are obtained from oscillating three-phase vectors in the abc −frame.

By aligning the a-axis of abc to the q-axis of $qd0$ −frame, the d-axis is always perpendicular to the q-axis which implies $v_d = 0$ is guaranteed by PLL.

When Θ is the real angle and $\hat{\Theta}$ is the estimated angle, the implementation and the design structure of the block diagram of the PLL is represented in **Figure 8** and **Figure 9**, respectively.

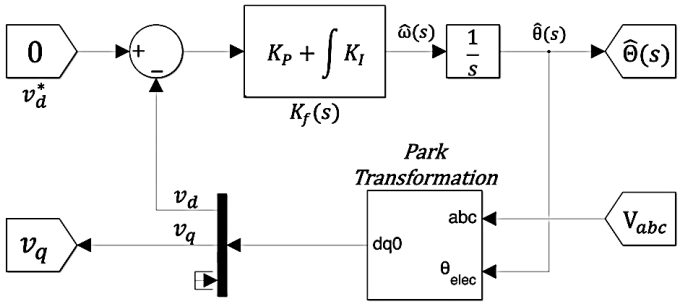

FIGURE 8 PLL - IMPLEMENTATION STRUCTURE

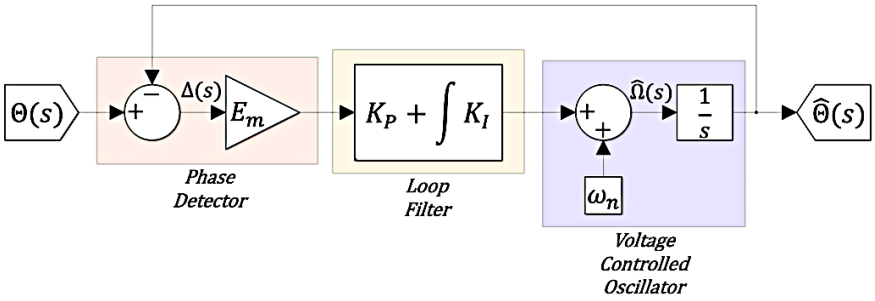

FIGURE 9 PLL - DESIGN STRUCTURE OF THE CLOSED LOOP SYSTEM [20]

PLL is a non-linear system, however, it can be linearized by applying the small-angle assumption expressed as

$$\lim_{\theta \to 0}(\sin\theta) \approx \lim_{\theta \to 0}(\theta) = 0$$
$$\lim_{\theta \to 0}(\cos\theta) \approx \lim_{\theta \to 0}\left(1 - \frac{\theta^2}{2}\right) = 1 \quad (14)$$

When the closed-loop system of the PLL is considered as the second-order system, it can be written in the second-order transfer function as

$$H_c(s) = \frac{\hat{\theta}(s)}{\theta(s)} = \frac{2\xi\omega_n s + {\omega_n}^2}{s^2 + 2\xi\omega_n + {\omega_n}^2} \quad (15)$$

where

the input $\theta(s)$ is the real grid angle, the output $\hat{\theta}(s)$ is the estimated grid angle, ω_n is the electrical angular velocity, and ζ is the damping ratio.

From this second-order system, the PI controller for the PLL can be defined as

$$K_f(s) = K_p^{PLL}\left(\frac{\frac{1}{\tau_{PLL}} + s}{s}\right) \tag{16}$$

where

τ_{PLL} is the PLL time constant. The proportional and integral gains for the PLL can be designed by defining electrical angular velocity as ω_n and PLL damping ratio as ζ_{PLL} which are expressed as (17) and (18), respectively.

$$\omega_n = \sqrt{\frac{K_p^{PLL} E_m}{\tau_{PLL}}} \tag{17}$$

$$\zeta_{PLL} = \sqrt{\frac{\tau_{PLL} K_p^{PLL} E_m}{2}} \tag{18}$$

where

E_m is the admitted peak voltage value, which corresponds to the phase-to-neutral grid RMS voltage multiplied by $\sqrt{2}$, or the phase-to-phase grid RMS voltage multiplied by $\sqrt{2}/\sqrt{3}$ in the three-phase system.

$$E_m = \sqrt{2} \cdot E_{g_{RMS}}^{P-N} = \frac{\sqrt{2}}{\sqrt{3}} \cdot E_{g_{RMS}}^{P-P} = \sqrt{2} \cdot 400\ V$$

By the rearrangement of (17) and (18), the PLL time constant can be expressed as $\tau_{PLL} = \frac{2\zeta_{PLL}}{\omega_n}$ and thus, K_p^{PLL} and K_i^{PLL} can be written as

$$K_p^{PLL} = \frac{2\zeta_{PLL}\omega_n}{E_m} \tag{19}$$

$$K_i^{PLL} = \frac{K_P^{PLL}}{\tau_{PLL}} = \frac{{\omega_n}^2}{E_m} \tag{20}$$

As stated for the initial condition, $\omega_n = 50\ Hz$ and $\zeta_{PLL} = 1/\sqrt{2}$.

3.3.2 Grid-connected VSC with inductive filtering components

For the convenience of the design, the very simplified equivalent model of the VSC can be implemented with the assumption that the IGBT valves controlled with PWM create the perfect sinusoidal waveform of AC so that it is simply represented with a three-phase AC source as shown in **Figure 10**.

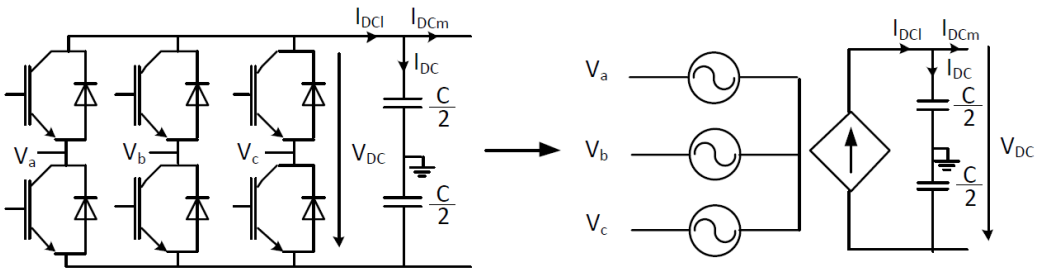

FIGURE 10 EQUIVALENT MODEL OF THE AC SIDE OF VSC

The equivalent scheme of **Figure 10** is illustrated in **Figure 11**.

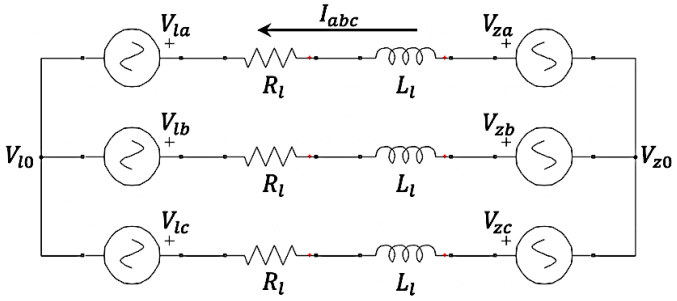

FIGURE 11 ELECTRICAL CIRCUIT OF THE EQUIVALENT MODEL

and its equation expression is

$$\begin{bmatrix} v_{za} \\ v_{zb} \\ v_{zc} \end{bmatrix} - \begin{bmatrix} v_{la} \\ v_{lb} \\ v_{lc} \end{bmatrix} - (v_{0l} - v_{0z}) \begin{bmatrix} 1 \\ 1 \\ 1 \end{bmatrix} = \begin{bmatrix} R_l & 0 & 0 \\ 0 & R_l & 0 \\ 0 & 0 & R_l \end{bmatrix} \begin{bmatrix} i_a \\ i_b \\ i_c \end{bmatrix} + \begin{bmatrix} L_l & 0 & 0 \\ 0 & L_l & 0 \\ 0 & 0 & L_l \end{bmatrix} \frac{d}{dt} \begin{bmatrix} i_a \\ i_b \\ i_c \end{bmatrix} \tag{21}$$

As it is the balanced system, being noted that $v_{0l} - v_{0z} = 0$, so (21) can be written in a more compact form which neglects neutral points as

$$v_{zabc} - v_{labc} = \begin{bmatrix} R_l & 0 & 0 \\ 0 & R_l & 0 \\ 0 & 0 & R_l \end{bmatrix} i_{abc} + \begin{bmatrix} L_l & 0 & 0 \\ 0 & L_l & 0 \\ 0 & 0 & L_l \end{bmatrix} \frac{d}{dt} i_{abc} \tag{22}$$

The correlation formula between the grid voltage v_{zabc} and the converter voltage v_{labc} can be defined with the Park transformation matrix $T(\theta)$ and its inverse $T(\theta)^{-1}$ which are **오류! 참조 원본을 찾을 수 없습니다.** and **오류! 참조 원본을 찾을 수 없습니다.**, respectively. Also, this correlation applies to the currents, i_{abc} and i_{qd0} as

$$\begin{aligned} v_{z-qd0} &= T(\theta) \cdot v_{z-abc} & v_{l-qd0} &= T(\theta) \cdot v_{z-abc} & i_{qd0} &= T(\theta) \cdot i_{abc} \\ v_{z-abc} &= T(\theta)^{-1} \cdot v_{z-qd0} & v_{l-abc} &= T(\theta)^{-1} \cdot v_{z-qd0} & i_{abc} &= T(\theta)^{-1} \cdot i_{qd0} \end{aligned} \tag{23}$$

By applying the property of matrix multiplication, it can be also written that

$$T(\theta) \cdot (\alpha \cdot \boldsymbol{I}) \cdot T^{-1}(\theta) = \alpha \cdot \boldsymbol{I} \tag{24}$$

where

α is a scalar, and $\boldsymbol{I}$ is an identity matrix.

With the consideration of the small-angular assumption (14), the following transformation matrix of $T(\theta)$ can be rearranged as

$$\boldsymbol{T(\theta)} = \frac{2}{3}\begin{bmatrix} \cos(\theta) & \cos\left(\theta-\frac{2\pi}{3}\right) & \cos\left(\theta+\frac{2\pi}{3}\right) \\ \sin(\theta) & \sin\left(\theta-\frac{2\pi}{3}\right) & \sin\left(\theta+\frac{2\pi}{3}\right) \\ \frac{1}{2} & \frac{1}{2} & \frac{1}{2} \end{bmatrix}$$

$$= \frac{2}{3}\begin{bmatrix} \cos(\theta) & \cos(\theta)\cos\left(\frac{2\pi}{3}\right)+\sin(\theta)\sin\left(\frac{2\pi}{3}\right) & \cos(\theta)\cos\left(\frac{2\pi}{3}\right)-\sin(\theta)\sin\left(\frac{2\pi}{3}\right) \\ \sin(\theta) & \sin(\theta)\cos\left(\frac{2\pi}{3}\right)-\cos(\theta)\sin\left(\frac{2\pi}{3}\right) & \sin(\theta)\cos\left(\frac{2\pi}{3}\right)+\cos(\theta)\sin\left(\frac{2\pi}{3}\right) \\ \frac{1}{2} & \frac{1}{2} & \frac{1}{2} \end{bmatrix} \tag{25}$$

$$= \frac{2}{3}\begin{bmatrix} \cos(\theta) & -\frac{1}{2}\cos(\theta)+\frac{\sqrt{3}}{2}\sin(\theta) & -\frac{1}{2}\cos(\theta)-\frac{\sqrt{3}}{2}\sin(\theta) \\ \sin(\theta) & -\frac{1}{2}\sin(\theta)-\frac{\sqrt{3}}{2}\cos(\theta) & -\frac{1}{2}\sin(\theta)+\frac{\sqrt{3}}{2}\cos(\theta) \\ \frac{1}{2} & \frac{1}{2} & \frac{1}{2} \end{bmatrix} \approx \frac{1}{3}\begin{bmatrix} 2 & -1 & -1 \\ 0 & -\sqrt{3} & \sqrt{3} \\ 1 & 1 & 1 \end{bmatrix}$$

In addition, according to the definition of the angle θ and the electrical angular velocity ω_e, the relationship between them is established as

$$\theta = \omega_e \cdot \int dt + \phi$$
$$\frac{d}{dt}\theta = \omega_e \tag{26}$$

When substituting (26), the derivative of its inverse $\frac{d}{dt}T(\theta)^{-1}$ can be rearranged as

$$\boldsymbol{\frac{d}{dt}T(\theta)^{-1}} = \frac{d}{dt}\begin{bmatrix} \cos(\theta) & \sin(\theta) & 1 \\ \cos\left(\theta-\frac{2\pi}{3}\right) & \sin\left(\theta-\frac{2\pi}{3}\right) & 1 \\ \cos\left(\theta+\frac{2\pi}{3}\right) & \sin\left(\theta+\frac{2\pi}{3}\right) & 1 \end{bmatrix}$$

$$= \frac{d}{dt}\begin{bmatrix} \cos(\theta) & \sin(\theta) & 1 \\ -\frac{1}{2}\cos(\theta)+\frac{\sqrt{3}}{2}\sin(\theta) & -\frac{1}{2}\sin(\theta)-\frac{\sqrt{3}}{2}\cos(\theta) & 1 \\ -\frac{1}{2}\cos(\theta)-\frac{\sqrt{3}}{2}\sin(\theta) & -\frac{1}{2}\sin(\theta)+\frac{\sqrt{3}}{2}\cos(\theta) & 1 \end{bmatrix} \tag{27}$$

$$= \frac{d}{dt}\begin{bmatrix} 1 & \theta & 1 \\ -\frac{1}{2}+\frac{\sqrt{3}}{2}\theta & -\frac{1}{2}\theta-\frac{\sqrt{3}}{2} & 1 \\ -\frac{1}{2}-\frac{\sqrt{3}}{2}\theta & -\frac{1}{2}\theta+\frac{\sqrt{3}}{2} & 1 \end{bmatrix} = \omega_e\begin{bmatrix} 0 & 1 & 0 \\ \frac{\sqrt{3}}{2} & -\frac{1}{2} & 0 \\ -\frac{\sqrt{3}}{2} & -\frac{1}{2} & 0 \end{bmatrix}$$

$$\boldsymbol{T(\theta)}\begin{bmatrix} L_l & 0 & 0 \\ 0 & L_l & 0 \\ 0 & 0 & L_l \end{bmatrix}\boldsymbol{\frac{d}{dt}T(\theta)^{-1}} = \frac{L_l\omega_e}{3}\begin{bmatrix} 2 & -1 & -1 \\ 0 & -\sqrt{3} & \sqrt{3} \\ 1 & 1 & 1 \end{bmatrix}\begin{bmatrix} 0 & 1 & 0 \\ \frac{\sqrt{3}}{2} & -\frac{1}{2} & 0 \\ -\frac{\sqrt{3}}{2} & -\frac{1}{2} & 0 \end{bmatrix} = \begin{bmatrix} 0 & L_l\omega_e & 0 \\ -L_l\omega_e & 0 & 0 \\ 0 & 0 & 0 \end{bmatrix} \tag{28}$$

Being reminded of (25) and (29), the equation expression (22) in abc −frame can be successfully transformed to the equation in $qd0$ −frame, following from (29) to (33).

Firstly, $\boldsymbol{T(\theta)}$ is multiplied on both sides of (22).

$$\boldsymbol{T(\theta)}v_{zabc} - \boldsymbol{T(\theta)}v_{labc} = \boldsymbol{T(\theta)}\begin{bmatrix} R_l & 0 & 0 \\ 0 & R_l & 0 \\ 0 & 0 & R_l \end{bmatrix}\boldsymbol{i_{abc}} + \boldsymbol{T(\theta)}\begin{bmatrix} L_l & 0 & 0 \\ 0 & L_l & 0 \\ 0 & 0 & L_l \end{bmatrix}\boldsymbol{\frac{d}{dt}i_{abc}} \tag{29}$$

Secondly, the voltages and the currents in abc frame are transformed to those in $qd0$ frame as (23).

$$v_{zqd0} - v_{lqd0} = \boldsymbol{T(\theta)} \begin{bmatrix} R_l & 0 & 0 \\ 0 & R_l & 0 \\ 0 & 0 & R_l \end{bmatrix} \boldsymbol{T(\theta)^{-1} \cdot i_{qd0}} + \boldsymbol{T(\theta)} \begin{bmatrix} L_l & 0 & 0 \\ 0 & L_l & 0 \\ 0 & 0 & L_l \end{bmatrix} \frac{\boldsymbol{d}}{\boldsymbol{dt}} \left(\boldsymbol{T(\theta)^{-1} \cdot i_{qd0}} \right) \tag{30}$$

Thirdly, the first term of the right-hand side is simplified by (24), and the second term is divided into two terms by the differential of $\boldsymbol{T(\theta)^{-1} \cdot i_{qd0}}$.

$$v_{zqd0} - v_{lqd0} = \begin{bmatrix} R_l & 0 & 0 \\ 0 & R_l & 0 \\ 0 & 0 & R_l \end{bmatrix} \boldsymbol{i_{qd0}} + \boldsymbol{T(\theta)} \begin{bmatrix} L_l & 0 & 0 \\ 0 & L_l & 0 \\ 0 & 0 & L_l \end{bmatrix} \frac{\boldsymbol{d}}{\boldsymbol{dt}} \boldsymbol{T(\theta)^{-1} \cdot i_{qd0}} + \boldsymbol{T(\theta)} \begin{bmatrix} L_l & 0 & 0 \\ 0 & L_l & 0 \\ 0 & 0 & L_l \end{bmatrix} \boldsymbol{T(\theta)^{-1}} \cdot \frac{\boldsymbol{d}}{\boldsymbol{dt}} \boldsymbol{i_{qd0}} \tag{31}$$

Fourthly, the second term is simply arranged by applying (25) and (27), and the third term by (24).

$$v_{zqd0} - v_{lqd0} = \begin{bmatrix} R_l & 0 & 0 \\ 0 & R_l & 0 \\ 0 & 0 & R_l \end{bmatrix} \boldsymbol{i_{qd0}} + \begin{bmatrix} 0 & L_l\omega_e & 0 \\ -L_l\omega_e & 0 & 0 \\ 0 & 0 & 0 \end{bmatrix} \cdot \boldsymbol{i_{qd0}} + \begin{bmatrix} L_l & 0 & 0 \\ 0 & L_l & 0 \\ 0 & 0 & L_l \end{bmatrix} \cdot \frac{\boldsymbol{d}}{\boldsymbol{dt}} \boldsymbol{i_{qd0}} \tag{32}$$

Lastly, the Clark transformation results in the zero-sequence of v_0 and i_0 in the stationary frame to be eliminated in the balanced three-phase system without neutral.

$$\begin{bmatrix} v_{zq} \\ v_{zd} \end{bmatrix} - \begin{bmatrix} v_{lq} \\ v_{ld} \end{bmatrix} = \begin{bmatrix} R_l & L_l\omega_e \\ -L_l\omega_e & R_l \end{bmatrix} \begin{bmatrix} i_q \\ i_d \end{bmatrix} + \begin{bmatrix} L_l & 0 \\ 0 & L_l \end{bmatrix} \frac{d}{dt} \begin{bmatrix} i_q \\ i_d \end{bmatrix} \tag{33}$$

where

v_{zq} and v_{zq} are the grid side $qd0$ voltages, v_{lq} and v_{ld} are the converter side $qd0$ voltages, i_q and i_d are the $qd0$ currents, and ω_e is the electrical angular velocity.

3.3.3 Inner Current Control loop

The inner loop of the VSC controller controls the currents flowing through the AC side of the convert as well as synchronize them with the grid angle, hence called a current controller. It also allows to track the current reference as the control target which is derived from the outer loop which determines the operation mode.

Recalling $v_{zd} = 0$ is guaranteed by the PLL, the final equation of (36) can be written again as

$$\begin{bmatrix} v_{zq} \\ 0 \end{bmatrix} - \begin{bmatrix} v_{lq} \\ v_{ld} \end{bmatrix} = \begin{bmatrix} R_l & L_l\omega_e \\ -L_l\omega_e & R_l \end{bmatrix} \begin{bmatrix} i_q \\ i_d \end{bmatrix} + \begin{bmatrix} L_l & 0 \\ 0 & L_l \end{bmatrix} \frac{d}{dt} \begin{bmatrix} i_q \\ i_d \end{bmatrix} \tag{34}$$

For the independent control of the q and the d components, which corresponds to active and reactive power, respectively, the highlighted coupling terms between q and d components need to be decoupled for their independent control. When outputs of the current controller $\hat{v}_{lq}$ and $\hat{v}_{ld}$ are defined as

$$\begin{bmatrix} \hat{v}_{lq} \\ \hat{v}_{ld} \end{bmatrix} = \begin{bmatrix} R_l & 0 \\ 0 & R_l \end{bmatrix} \begin{bmatrix} i_q \\ i_d \end{bmatrix} + \begin{bmatrix} L_l & 0 \\ 0 & L_l \end{bmatrix} \frac{d}{dt} \begin{bmatrix} i_q \\ i_d \end{bmatrix} \tag{35}$$

the voltages to be applied by converters, v_{lq} and v_{ld}, are arranged in completely decoupled expression by substituting (35) to (32) as shown in (36).

$$\begin{bmatrix} v_{lq} \\ v_{ld} \end{bmatrix} = \begin{bmatrix} -\hat{v}_{lq} + v_{zq} - L_l\omega_e i_q \\ -\hat{v}_{ld} + L_l\omega_e i_d \end{bmatrix} \tag{36}$$

Then, the transfer functions between the voltages to be applied by the inner current controller and the converter currents can be derived by applying the Laplace transformation as

$$\frac{\hat{v}_{lq}(s)}{i_q(s)} = \frac{1}{l_l s + r_l} \tag{37}$$

$$\frac{\hat{v}_{ld}(s)}{i_d(s)} = \frac{1}{l_l s + r_l} \tag{38}$$

From the equation above, the implementation and the structure

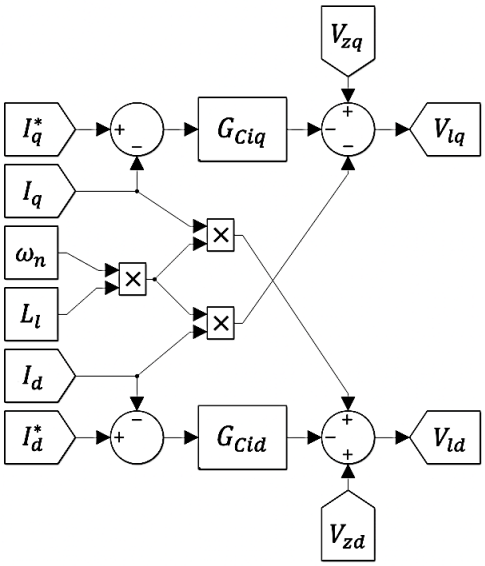

FIGURE 12 INNER CURRENT CONTROL LOOP - IMPLEMENTATION STRUCTURE

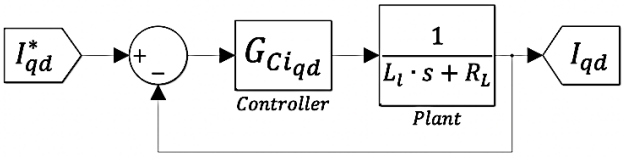

FIGURE 13 INNER CURRENT CONTROL LOOP - DESIGN STRUCTURE

The equation expression of **Figure 13** is

$$\frac{i_{qd}}{i_{qd}^*} = \frac{G_c(s)}{L_l s + R_l + G_c(s)} \tag{39}$$

The closed-loop system for the current PI controller is the second-order system. Nevertheless, the current controller follows the internal model control technique which imposes the first-order response, expressed as

$$\frac{i_{qd}}{i_{qd}^*} = \frac{1}{\tau_{ic} s + 1} \tag{40}$$

The first-order responsive PI controller can be designed as

$$G_{ciq}(s) = G_{cid}(s) = \frac{K_p^{ic} s + K_i}{s} \tag{41}$$

where

the proportional parameter K_p^{ic} and the integral parameter K_i^{ic} can be calculated as

$$K_p^{ic} = \frac{L_l}{\tau_{ic}} \tag{42}$$

$$K_i^{ic} = \frac{R_l}{\tau_{ic}} \tag{43}$$

where

τ_{ic} is the closed-loop time constant of the electrical system, and it usually has 10 times faster value than the converter switching period, the reciprocal of the frequency. In this case, its value is $\tau_{ic} = 0.001\ sec$.

3.4 Operation mode for VSC Control

The VSC operation modes are differentiated depending on the controller design of the cascaded current loop. Four available options typically applied are shown in **Figure 14**

- Active Power (P) and Reactive Power (Q)

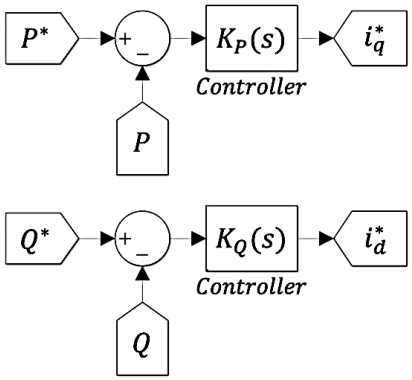

- Active Power (P) and Voltage amplitude (V_{AC})

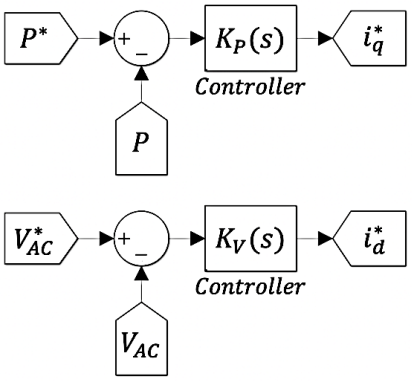

- DC Voltage/amplitude (V_{DC}) and Reactive Power (Q)

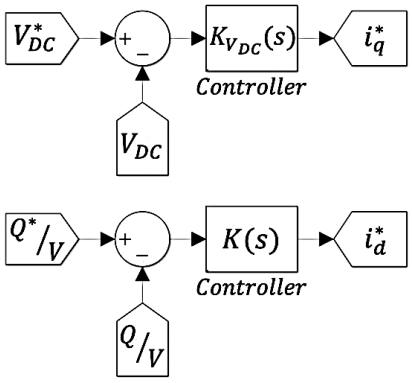

- Grid-forming

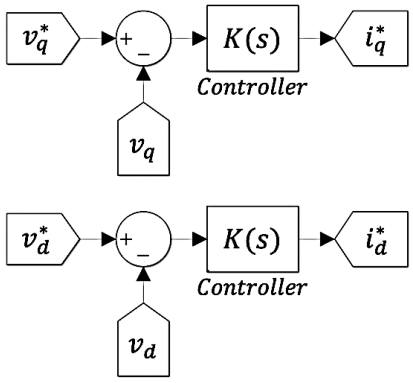

FIGURE 14 MODES OF VSC OPERATION

Depending on which operation mode is to be applied, the DC side of the VSC is modeled differently. In this Master thesis, in the $P-Q$ operation mode, the DC side is considered as a voltage source and the reference currents i_{qd}^* are directly obtained from the reference active and reactive powers, P^* and Q^*, without any controllers. On the other hand, in the $V_{DC}-Q$ mode, the DC side is considered as a current source and the design of the controller to obtain the reference current i_q^* from the reference DC voltage V_{DC}^* is added, whereas the calculation of i_d^* is the same as in the $P-Q$ mode.

3.4.1 $P - Q$ Mode

The first mode to investigate is the active power and reactive power control. This mode is preferably utilized for an energy storage system (ESS), which of the most commercialized is an electrical secondary battery, with its ability to supply constant DC voltage required for the control IGBT valves according to PWM modulation.

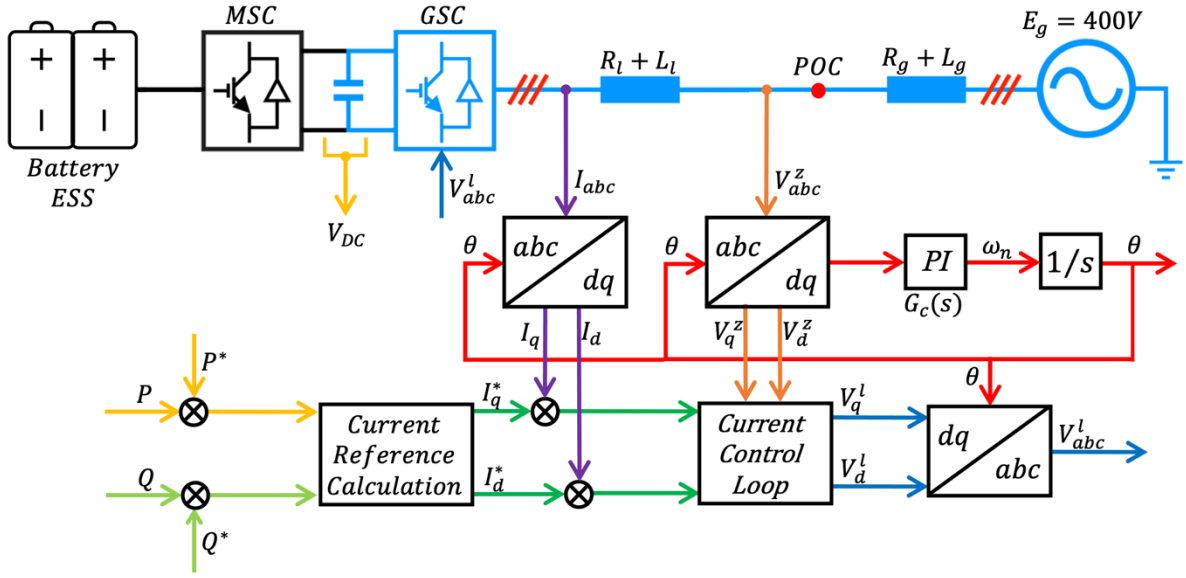

FIGURE 15 GENERAL SCHEME OF THE GRID-CONNECTED VSC CONTROLLER IN $P - Q$ OPERATION MODE

As stated in the instantaneous power theory equation (6) and (7), the desired active and reactive power references P^* and Q^* are expressed as

$$P^* = \frac{3}{2}\left(v_{zq} i_q^* + v_{zd} i_d^*\right) \tag{44}$$

$$Q^* = \frac{3}{2}\left(v_{zq} i_d^* - v_{zd} i_q^*\right) \tag{45}$$

From the PLL which ensures the v_{zd} component of the grid voltage is 0, each second term of (44) and (45) is subtracted, and then, i_q^* and i_d^* can be expressed as (46) and (47) in proportion to active power and reactive power, respectively.

$$i_q^* = \frac{2P^*}{3v_{zq}} \tag{46}$$

$$i_d^* = \frac{2Q^*}{3v_{zq}} \tag{47}$$

Therefore, the straightforward implementation of desired active and reactive power enables the control of the reference currents i_q^* and i_d^* in an open loop with the first-order response.

3.4.2 $V_{DC} - Q$ Mode

The second applicable mode is the DC-link voltage and reactive power control. By regulating the DC voltage of the DC-link capacitor with the external disturbance current I_{DC_m}, active power transmitted between the grid can be controlled, so called $V_{DC} - Q$ operation mode. V_{DC}, the DC voltage applied to the capacitor C_{DC}, is controlled to a constant value, in this case $800\ V$. Such a characteristic allows $V_{DC} - Q$ operation mode to be generally applied to the control of generation sources whose output do not guarantee the supply of constant DC voltage for PWM modulation. In addition to the impact of $P - Q$ control mode, the state-space of the DC-link capacitor is to be added in this mode.

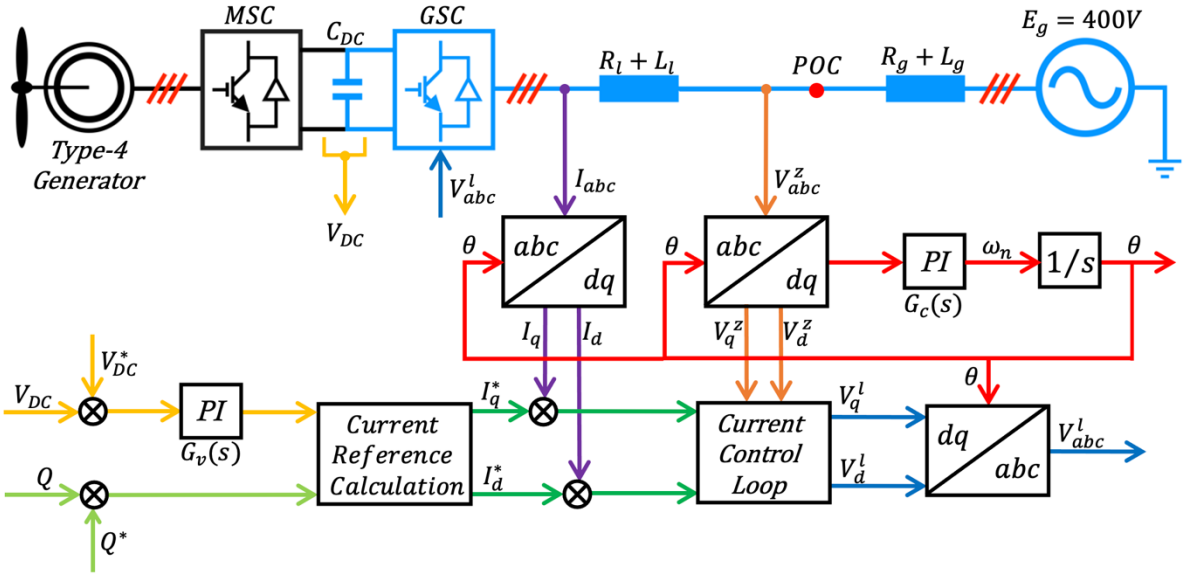

FIGURE 16 GENERAL SCHEME OF THE GRID-CONNECTED VSC CONTROLLER IN $V_{DC} - Q$ OPERATION MODE

From **Figure 10** which represents the simplified scheme of the DC voltage regulated VSC, when assuming the power exchanged between the AC and the DC side is equal, it can be written that

$$I_{DC_l} = \frac{P_{AC}}{V_{DC}}$$

$$I_{DC} = I_{DC_l} - I_{DC_m} = C_{dc}\frac{dV_{DC}}{dt} \tag{48}$$

$$V_{DC} = V_{DC_0} + \frac{1}{C}\int_0^t I_{DC}\,dt = V_{DC_0} + \frac{1}{C}\int_0^t (I_{DC_l} - I_{DC_m})\,dt$$

The reference calculation of the DC link voltage adopts the feedback, or a closed-loop, control.

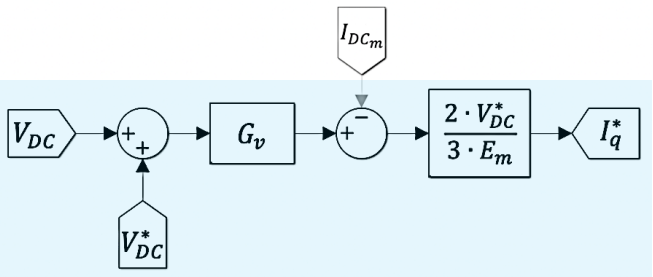

FIGURE 17 OUTER VOLTAGE CONTROL LOOP - IMPLEMENTATION STRUCTURE

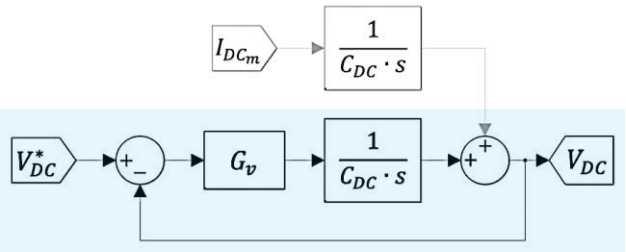

FIGURE 18 OUTER VOLTAGE CONTROL LOOP - DESIGN STRUCTURE

This closed-loop system can be written in the second-order transfer function as

$$V_{dc} = \frac{G_V(s)}{C_{DC}s + G_V(s)} V_{dc}^* + \frac{1}{C_{DC}s + G_V(s)} I_{DC_m}$$
$$\frac{I_{DC_m}}{V_{dc}^*} = \frac{1}{C_{DC}s + G_V(s)} \quad \leftrightarrow \quad \frac{I_{DC_m}}{V_{dc}^*} = \frac{s}{s^2 + 2\xi_V \omega_V s + {\omega_V}^2} \tag{49}$$

When reorganize (49) based on the term of the PI controller $G_V(s)$,

$$G_V(s) = \frac{K_p^V s + K_i^V}{s} \quad \leftrightarrow \quad \frac{I_{DC_m}}{V_{dc}^*} = \frac{s}{C_{DC}s^2 + K_p^V s + K_i^V} \tag{50}$$

where

the proportional factor is $$K_p^V = 2\xi_V \omega_v C_{DC} \tag{51}$$

and the Integral factor is $$K_i^V = {\omega_v}^2 C_{DC} \tag{52}$$

In the model, the design parameters are as follows:

the damping ratio of the voltage controller is $$\xi_V = \frac{1}{\sqrt{2}} \approx 0.7071 \tag{53}$$

and the frequency of the DC controller is $$\omega_V = 2\pi \cdot \frac{1}{\tau_{ic}} \cdot \alpha_V \tag{54}$$

In (50), α_v is introduced as the proportional factor determining the desired angular velocity of the DC voltage controller ω_v. The reason is that the DC voltage loop, which is the upper-level outer loop, must be slower than the lower-level inner current controller so as to ensure the stable system response, and its value as the proportional factor is

$$\alpha_V = 0.05$$

3.5 Non-linear model in $MATLAB/Simulink$

In **Figure 19**, firstly, the grid side converter and the grid are represented with each of resistance and inductance. Secondly, PLL tracks the grid angle, and it is used for the synchronization of grid reference qd −currents flowing through the converter to the converter reference. The $qd-$ reference currents are from active and reactive power which are directly fed to the system in the $\boldsymbol{P-Q}$ operation mode. The output of the inner current control loop, qd −voltages in converter reference are converted to grid reference to be connected to the grid.

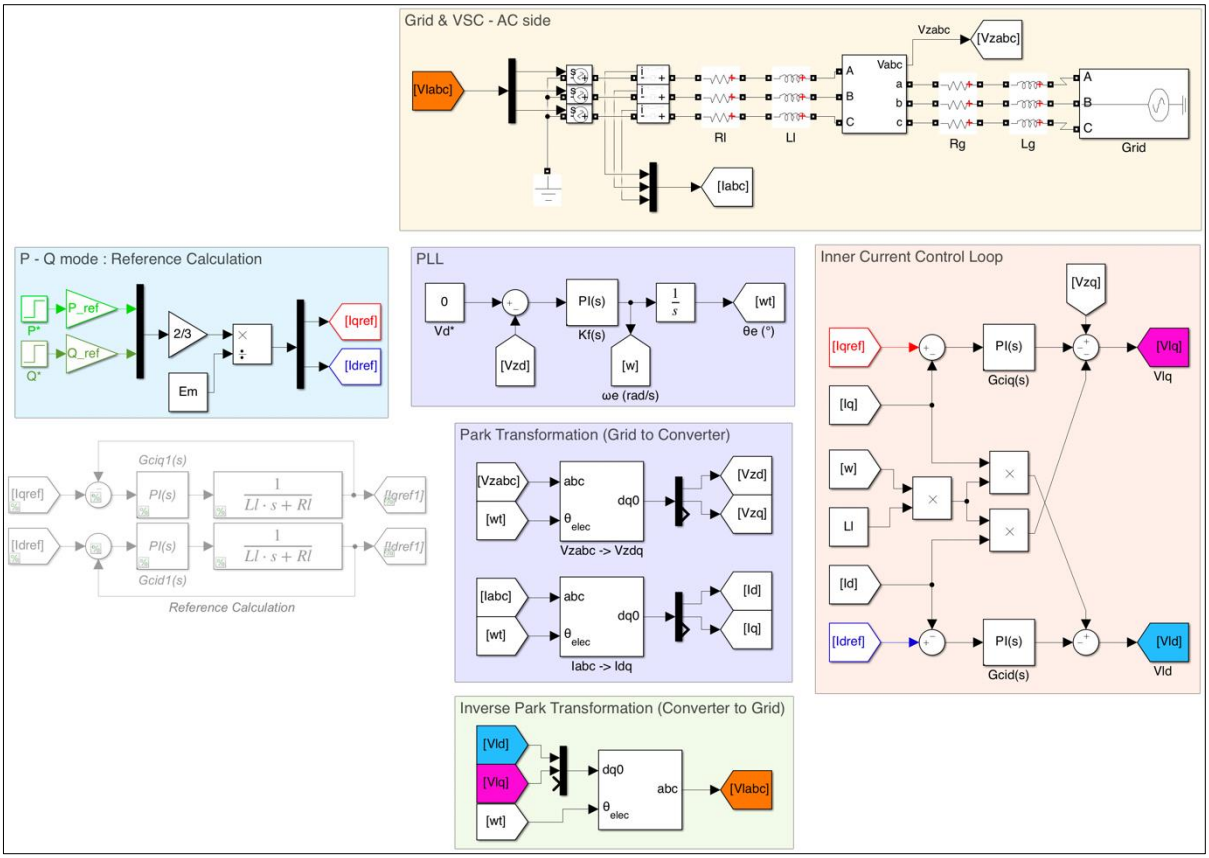

FIGURE 19 NON-LINEAR MODEL WITH $\boldsymbol{P-Q}$ OPERATION MODE

Most of the principal of the operation in $\boldsymbol{V_{DC}-Q}$ mode is the same as $\boldsymbol{P-Q}$ mode, however, the $q-$ reference current is controller with added PI-controller, $G_V(s)$. Also, the DC side equivalent circuit is added including the capacitor, C_{DC}. Therefore, it is needed to consider the bus where the AC power and DC power are equal to each other if any losses are neglected.

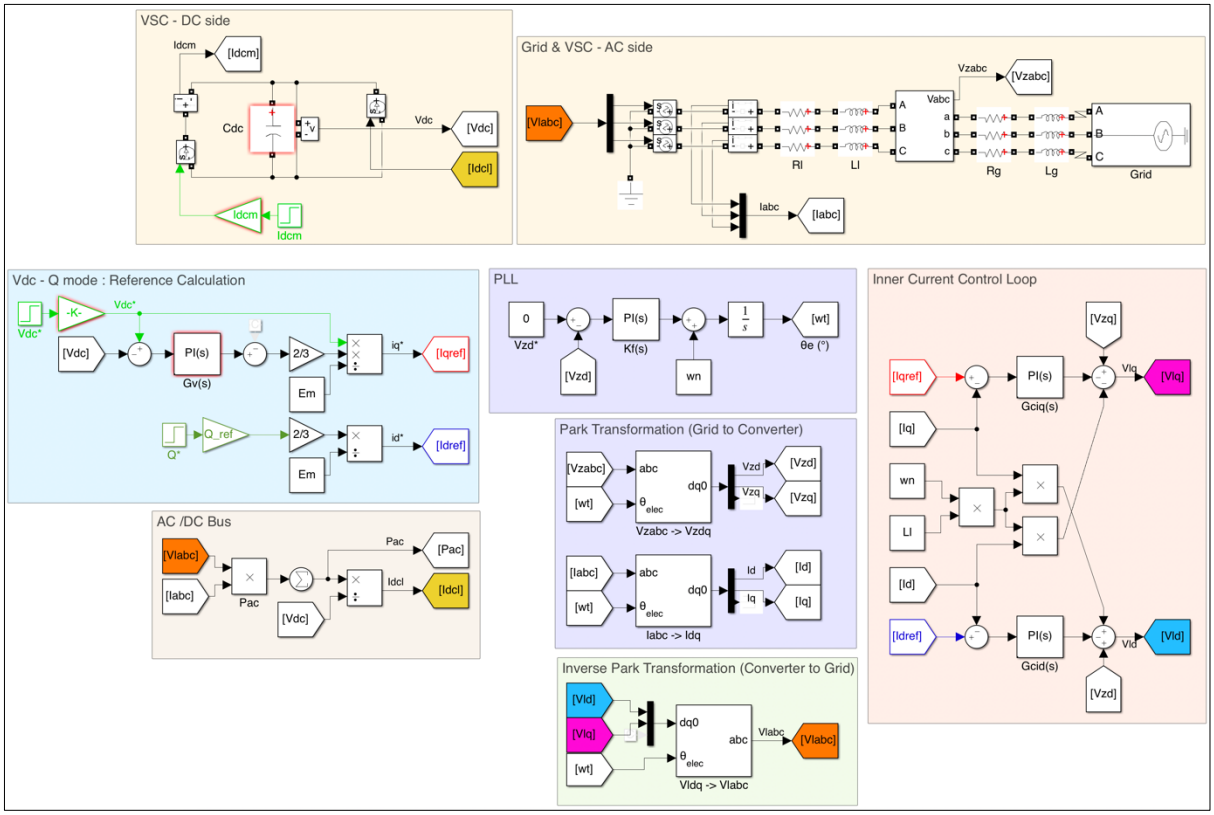

FIGURE 20 NON-LINEAR MODEL WITH $\boldsymbol{V_{DC}-Q}$ OPERATION MODE

4. Linear model of the VSC Controller

4.1 Linearization Process

For control, a linear system is preferred to a nonlinear system. Thus, the non-linear model is to be linearized for the linear model design. In this chapter since the linearization of the VSC in $\boldsymbol{P} - \boldsymbol{Q}$ mode can be applied as part of $\boldsymbol{V_{DC}} - \boldsymbol{Q}$ mode, only the linearization process of the VSC in $\boldsymbol{V_{DC}} - \boldsymbol{Q}$ operation mode is described as possible.

The general equation for the linearization of a function $f(x)$ is:

$$f(x) = f(x_0) + f'(x_0)(x - x_0) \tag{55}$$

where

x is the vector of variables

x_0 is the linearization point

$f'(x_0)$ is the derivative of $f(x)$, defined as the slope of $f(x)$ at point x_0

Figure 21 shows the procedure of obtaining an initial value of each variable at the linearization point, which corresponds to obtaining $f(x_0)$ when $x = x_0$ as same as in (55), at which the time is equal to the last second of the simulation time t_{sim}^{nolin} in $MATLAB/Simulink$.

As $f'(x_0)(x - x_0)$ in (55) can be calculated from the state-space model, the linearization of the VSC controller aa the time interval from $0\ sec$ to $T_{sim}^{(end)} = 3\ seconds$.

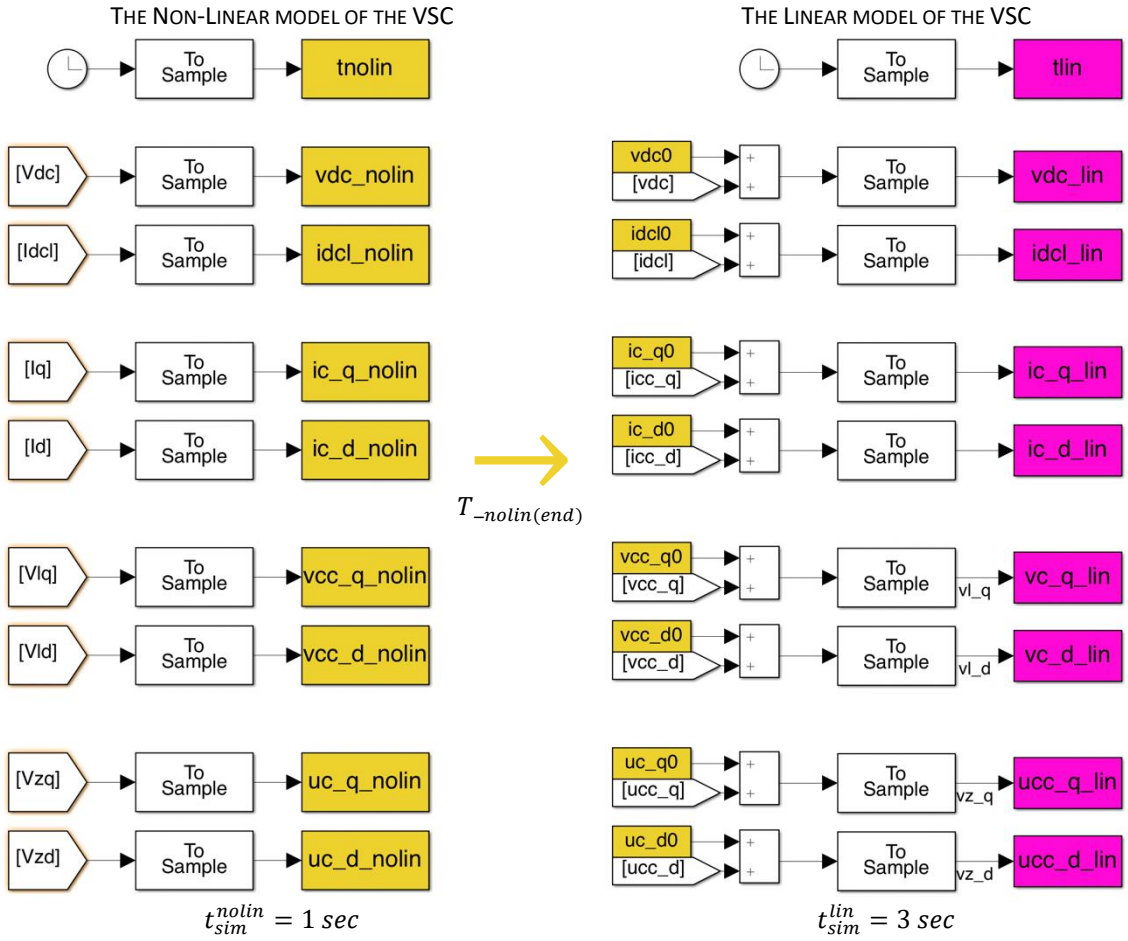

FIGURE 21 PROCEDURE OF OBTAINING INITIAL VALUE AT THE LINEARIZATION POINT

The initial value of each linearized variable, represented as $f(x_0)$ in (55), is calculated as

$$\begin{aligned} I_0^{DC_l} &= I_{DC_l - nolin(end)} \\ V_0^{DC} &= V_{DC\,-nolin(end)} \\ i_{d0}^{c} &= i_q^{c}\ _{-nolin(end)} \\ i_{d0}^{c} &= i_d^{c}\ _{-nolin(end)} \\ v_{q0}^{cc} &= v_q^{cc}\ _{-nolin(end)} \\ v_{d0}^{cc} &= v_d^{cc}\ _{-nolin(end)} \\ u_{q0}^{cc} &= u_q^{c}\ _{-nolin(end)} \\ u_{d0}^{cc} &= u_d^{c}\ _{-nolin(end)} \end{aligned} \tag{56}$$

With these initial values, the linearization of the nonlinear model in the simulation of $3\ seconds$ is performed.

4.2 State-space

For any arbitrary dynamic system, the relationship between its state and its derivatives represents the stability of the system, which is an inherent property. The way the system moves, however, can also be influenced by external inputs being added or removed over time. So, the derivatives of a dynamic system are expressed as a function of both the current state as well as any external inputs.

$$\ddot{p}(t) = -\frac{k}{m}p(t) \quad \leftrightarrow \quad \dot{x} = f(x, u)$$

In state-space representation, it is simply a repacking of the second-order differential equations of the dynamics into a set of the first-order equations that focus on this relationship, and how a system changes in the future.

There are also numerical solution befits when simulating the system as a state-space model since the vector of the derivatives is built first, and then integrates the whole vector to get the states.

Different from a higher order differential equation or a transfer function that looking into the entire dynamics of the system, the state-space equation rather focuses on the dynamics of each state variable and how those variables are related to each other. Repackaging into a matrix form of the series of linear equations allows access to various mathematical tools.

Continuous state-space form for a linear time-invariant (LTI) system is a set of two equations. The first one is the state-space equation built around the state vector $x(t)$ which is the vector of all the state variables. The derivative of the state $\dot{x}(t)$, or how the state vector changes, is a linear combination of current space plus a linear combination of external inputs. The second one is the output equation, a linear combination of states and input. The outputs are not necessarily the state variables, for instance when the $C\ matrix$ is a zero matrix.

$$\begin{aligned} \dot{x}_n(t) &= A_{n\times n} \cdot x_n(t) + B_{n\times l} \cdot u_l(t) \\ y_m(t) &= C_{m\times n} \cdot x_n(t) + D_{m\times l} \cdot u_l(t) \end{aligned} \tag{57}$$

where,

$x_n(t) = "state\ vector"\ of\ dimention\ n$

$y_m(t) = "output\ vector"\ of\ dimension\ m$

$u_l(t) = "input\ vector"\ of\ dimension\ l$

$A = "system\ dynamic\ matrix"\ or\ "plant\ matrix"\ of\ size\ n \times n$

$B =\ control\ \ input\ matrix\ of\ size\ n \times r$

$C = "output\ matrix"\ of\ size\ m \times n$

$D = "feedforward\ matrix"\ of\ m \times l$

The conceptual meaning of each vector and matrixes are as following.

$x(t)$ is the minimum set of state variables that fully describe the variation of the system.

$y(t)$ is the set of vectors of the outputs of the system.

$A\ matrix$ representing the current state describes how the internal states are all connected to each other.

$B\ matrix$ describes how the inputs enter into the system which states are they affecting.

$C\ matrix$ how the states are combined to get the outputs.

$D\ matrix$ used to allow the inputs to bypass the system altogether and feedforward to the output.

4.3 Eigenvectors and Modal matrices

The general explanation of eigenvalues in this chapter refers to [21].

The eigenvalues of $A\,matrix$ are given by the values of the scalar parameter of λ.

$$A\phi = \lambda\phi \tag{58}$$

where

$\boldsymbol{\phi}$ is the *right eigenvector*, a matrix of size $n \times 1$, other than 0

To find the eigenvalues, (58) can be written to

$$(A - \boldsymbol{I}\lambda) \cdot \phi = 0$$

and for a non-trivial solution, (59)

$$det(A - \boldsymbol{I}\lambda) = 0$$

The eigenvalues of $A\,matrix$ is n solutions of λ, which are $\lambda_1,\ \lambda_2,\ \lambda_3, \cdots, \lambda_n$.

For each of ϕ, there exist a matrix of size $1 \times n$, the normalized vector in practice, which satisfies

$$\psi_i \phi_i = 1 \tag{60}$$

where

$i = 1, 2, 3, \cdots, n$

$\boldsymbol{\phi_i}$ is the *right eigenvector*

$\boldsymbol{\psi_i}$ is the *left eigenvector*

For the simple expression of the eigen-properties of $A\,matrix$, when expanding (58) to (60),

$$\begin{gathered} A \cdot \Phi = \Phi \cdot \boldsymbol{\Lambda} \\ \Psi \cdot \Phi = \boldsymbol{I} \quad \text{and} \quad \Psi = \Phi^{-1} \end{gathered} \tag{61}$$

where

$\Phi = [\phi_1,\ \phi_2,\ \phi_3, \cdots, \phi_n]$

$\Psi = [\psi_1,\ \psi_2,\ \psi_3, \cdots, \psi_n]$

$\boldsymbol{\Lambda} =$ diagonal matrix, with the eigenvalues $\lambda_1,\ \lambda_2,\ \lambda_3, \cdots, \lambda_n$ as diagonal element

In follows from (66),

$$\Phi^{-1} A \cdot \Phi = \boldsymbol{\Lambda} \tag{62}$$

By using $MATLAB$, the procedure to obtain $\boldsymbol{\Lambda}$ is very simplified.

4.4 Design of the linear model

4.4.1 Phase Locked Loop (PLL)

The state-space of the PLL is separated into two sub-blocks. The first block corresponds to the loop filter to make the error between the reference and the measured value zero. The input is the change in the reference and the instantaneous grid voltage on the $d-axis$, and the output $\Delta\omega$ is the change in the electrical angular velocity.

$$\begin{aligned}\frac{d}{dt}\begin{bmatrix}\int \Delta v_{zd}^{*} \\ \int \Delta v_{zd}\end{bmatrix} &= \begin{bmatrix}0 & 0 \\ 0 & 0\end{bmatrix}\cdot\begin{bmatrix}\int \Delta v_{zd}^{*} \\ \int \Delta v_{zd}\end{bmatrix} + \begin{bmatrix}1 & 0 \\ 0 & 1\end{bmatrix}\cdot\begin{bmatrix}\Delta v_{zd}^{*} \\ \Delta v_{zd}\end{bmatrix} \\ [\Delta\omega] &= [K_i^{PLL} \quad -K_i^{PLL}]\cdot\begin{bmatrix}\int \Delta v_{zd}^{*} \\ \int \Delta v_{zd}\end{bmatrix} + [K_p^{PLL} \quad -K_p^{PLL}]\cdot\begin{bmatrix}\Delta v_{zd}^{*} \\ \Delta v_{zd}\end{bmatrix}\end{aligned} \tag{63}$$

The second block matches to the voltage-controlled oscillator whose input and the output are $\Delta\omega$ and the change in the grid angle $\Delta\theta$, respectively.

$$\begin{aligned}\frac{d}{dt}[\Delta\theta] &= [0]\cdot[\Delta\theta] + [1]\cdot[\Delta\omega] \\ [\Delta\theta] &= [1]\cdot[\Delta\theta] + [0]\cdot[\Delta\omega]\end{aligned} \tag{64}$$

where

$K_p^{PLL} = \frac{2\xi_{PLL}\omega_n}{E_m}$, $K_i^{PLL} = \frac{K_P^{PLL}}{\tau_{PLL}}$, $\tau_{PLL} = \frac{2\xi_{PLL}}{\omega_n}$ and $\xi = \frac{1}{\sqrt{2}} \approx 0.7071$.

The state-space block diagram of the PLL is shown as

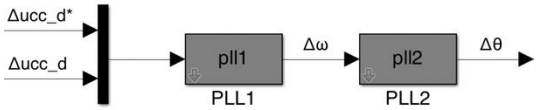

FIGURE 22 PLL - STATE-SPACE BLOCK

4.4.2 Inner Current Controller (IC)

The state-space of the inner current control loop is presented as

$$\begin{aligned}\frac{d}{dt}\begin{bmatrix}\int \Delta i_q^{c*} \\ \int \Delta i_d^{c*} \\ \int \Delta i_q^{c} \\ \int \Delta i_d^{c}\end{bmatrix} &= \begin{bmatrix}0 & 0 & 0 & 0 \\ 0 & 0 & 0 & 0 \\ 0 & 0 & 0 & 0 \\ 0 & 0 & 0 & 0\end{bmatrix}\cdot\begin{bmatrix}\int \Delta i_q^{c*} \\ \int \Delta i_d^{c*} \\ \int \Delta i_q^{c} \\ \int \Delta i_d^{c}\end{bmatrix} + \begin{bmatrix}1 & 0 & 0 & 0 & 0 & 0 \\ 0 & 1 & 0 & 0 & 0 & 0 \\ 0 & 0 & 1 & 0 & 0 & 0 \\ 0 & 0 & 0 & 1 & 0 & 0\end{bmatrix}\cdot\begin{bmatrix}\Delta i_q^{c*} \\ \Delta i_d^{c*} \\ \Delta i_q^{c} \\ \Delta i_d^{c} \\ \Delta v_q^{z} \\ \Delta v_d^{z}\end{bmatrix} \\ \begin{bmatrix}\Delta v_{lq} \\ \Delta v_{ld}\end{bmatrix} &= \begin{bmatrix}-K_i^{ic} & 0 & K_i^{ic} & 0 \\ 0 & K_i^{ic} & 0 & K_i^{ic}\end{bmatrix}\cdot\begin{bmatrix}\int \Delta i_q^{c*} \\ \int \Delta i_d^{c*} \\ \int \Delta i_q^{c} \\ \int \Delta i_d^{c}\end{bmatrix} + \begin{bmatrix}-K_p^{ic} & 0 & K_p^{ic} & -\omega_n L & 1 & 0 \\ 0 & -K_p^{ic} & \omega_n L & K_p^{ic} & 0 & 1\end{bmatrix}\cdot\begin{bmatrix}\Delta i_q^{c*} \\ \Delta i_d^{c*} \\ \Delta i_q^{c} \\ \Delta i_d^{c} \\ \Delta v_q^{z} \\ \Delta v_d^{z}\end{bmatrix}\end{aligned} \tag{65}$$

where

$K_p^{ic} = \frac{l_l}{\tau_{ic}}$ and $K_i^{ic} = \frac{r_l}{\tau_{ic}}$.

The input and the output of the state-space block diagram of the inner current control loop is shown as

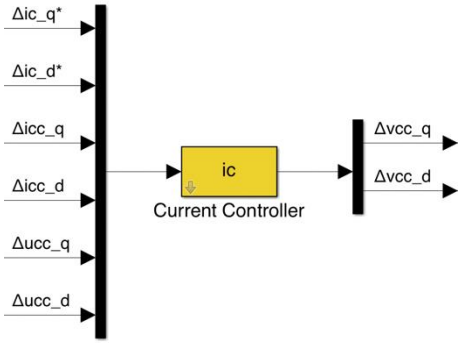

FIGURE 23 INNER CURRENT CONTROL LOOP – STATE-SPACE BLOCK

4.4.3 Grid-connected VSC with inductive filtering components

One difference of the state-space is that V_{z0} of the non-linear model in **Figure 11** is measured at POC, at which the point is after the Thevenin equivalent impedances of R_g and L_g. However, v_{qd}^z is the grid level voltages measured before R_g and L_g. Therefore, the matrixes of A, B, C, and D for the state-space $'filterL'$ differ from those of the non-linear model, as shown in (66).

$$\frac{d}{dt}\begin{bmatrix}\Delta i_q^c\\ \Delta i_d^c\end{bmatrix}=\begin{bmatrix}-\frac{r_{gl}}{L_{gl}} & -\omega_n\\ \omega_n & -\frac{r_{gl}}{L_{gl}}\end{bmatrix}\cdot\begin{bmatrix}\Delta i_q^c\\ \Delta i_d^c\end{bmatrix}+\begin{bmatrix}-\frac{1}{L_{gl}} & 0 & \frac{1}{L_{gl}} & 0\\ 0 & -\frac{1}{L_{gl}} & 0 & \frac{1}{L_{gl}}\end{bmatrix}\cdot\begin{bmatrix}\Delta v_q^c\\ \Delta v_d^c\\ \Delta v_q^z\\ \Delta v_d^z\end{bmatrix}$$

$$\begin{bmatrix}\Delta i_q^c\\ \Delta i_d^c\\ \Delta v_q^z\\ \Delta v_d^z\end{bmatrix}=\begin{bmatrix}1 & 0\\ 0 & 1\\ -\frac{r_gL_l-r_lL_g}{L_{gl}} & 0\\ 0 & -\frac{r_gL_l-r_lL_g}{L_{gl}}\end{bmatrix}\cdot\begin{bmatrix}\Delta i_q^c\\ \Delta i_d^c\end{bmatrix}+\begin{bmatrix}0 & 0 & 0 & 0\\ 0 & 0 & 0 & 0\\ \frac{L_g}{L_{gl}} & 0 & \frac{L_l}{L_{gl}} & 0\\ 0 & \frac{L_g}{L_{gl}} & 0 & \frac{L_l}{L_{gl}}\end{bmatrix}\cdot\begin{bmatrix}\Delta v_q^c\\ \Delta v_d^c\\ \Delta v_q^z\\ \Delta v_d^z\end{bmatrix} \quad (66)$$

The state-space block diagram of the inductive filter is shown as

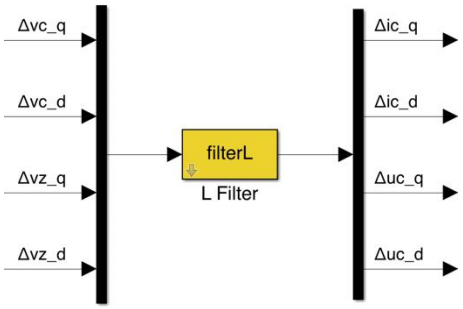

FIGURE 24 GRID-VSC CONNECTED L-FILTER – STATE-SPACE BLOCK

4.4.4 Angle rotation between the grid and the converter

4.4.4.1 Conversion from v_{qd}^{cc}(converter) to v_{qd}^{c}(grid) - the Inverse Park transformation

Since the current controller outputs follow the converter reference, the inverse Park transformation by $\Delta\theta$ is applied to transform the output of the state -space $'ic'$, from the converter reference to the grid references. Applying the linearization process, the expression of the transformation is

$$\begin{bmatrix}\Delta v_q^c\\ \Delta v_d^c\end{bmatrix} = \begin{bmatrix}0\\0\end{bmatrix}\cdot[\quad] + \begin{bmatrix}\cos\theta_e & \sin\theta_e & -\sin\theta_e\cdot v_{q0}^{cc} + \cos\theta_e\cdot v_{d0}^{cc}\\ -\sin\theta_e & \cos\theta_e & -\cos\theta_e\cdot v_{q0}^{cc} - \sin\theta_e\cdot v_{d0}^{cc}\end{bmatrix}\cdot\begin{bmatrix}\Delta v_q^{cc}\\ \Delta v_d^{cc}\\ \Delta\theta\end{bmatrix} \tag{67}$$

where

$\Delta\theta = \theta_{cc} - \theta_c = \theta_{cc}$ as the grid reference angle $\theta_c = 0\,°$ by the PLL, and θ_e is the error of the angle, which is very close to 0, between the desired and the actual angle. In the model, it is set as $\theta_e = 10^{-36}\,°$.

The Park Transformation state-space block diagram of the converter output voltage is

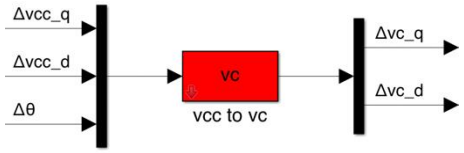

FIGURE 25 ANGLE ROTATION OF THE VOLTAGE FROM CONVERTER TO GRID – STATE-SPACE BLOCK

4.4.4.2 Conversion from u_{qd}^{c}(grid) to u_{qd}^{cc}(converter) - the Park transformation

Opposite from the process in the conversion from v_{qd}^{cc}(converter) to v_{qd}^{c}(grid) - the inverse Park transformation, the grid voltages as outputs of the state-space $'filterL'$ follows the grid reference. Therefore, they need to be converted to the converter reference to be input to the state-space $'ic'$. The equation (68) shows the Park transformation process rotates by $\Delta\theta$.

$$\begin{bmatrix}\Delta u_q^{cc}\\ \Delta u_d^{cc}\end{bmatrix} = \begin{bmatrix}0\\0\end{bmatrix}\cdot[\quad] + \begin{bmatrix}\cos\theta_e & -\sin\theta_e & -\sin\theta_e\cdot u_{q0}^{c} - \cos\theta_e\cdot u_{d0}^{c}\\ \sin\theta_e & \cos\theta_e & \cos\theta_e\cdot u_{q0}^{c} - \sin\theta_e\cdot u_{d0}^{c}\end{bmatrix}\cdot\begin{bmatrix}\Delta u_q^{c}\\ \Delta u_d^{c}\\ \Delta\theta\end{bmatrix} \tag{68}$$

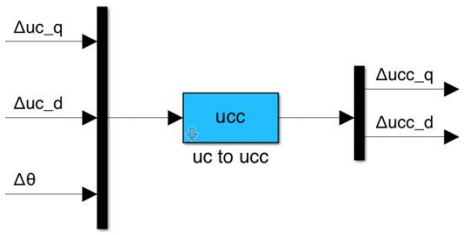

FIGURE 26 ANGLE ROTATION OF THE VOLTAGE FROM GRID TO CURRENT CONTROLLER – STATE-SPACE BLOCK

4.4.4.3 Conversion from i_{qd}^{c}(grid) to i_{qd}^{cc}(converter) - the Park transformation

The same method is applied to the transformation of the converter reference currents i_{qd}^{cc} to the grid reference currents i_{qd}^{c} as

$$\begin{bmatrix}\Delta i_q^{cc}\\ \Delta i_d^{cc}\end{bmatrix} = \begin{bmatrix}0\\0\end{bmatrix}\cdot[\quad] + \begin{bmatrix}\cos\theta_e & -\sin\theta_e & -\sin\theta_e\cdot i_{q0}^{c} - \cos\theta_e\cdot i_{d0}^{c}\\ \sin\theta_e & \cos\theta_e & \cos\theta_e\cdot i_{q0}^{c} - \sin\theta_e\cdot i_{d0}^{c}\end{bmatrix}\cdot\begin{bmatrix}\Delta i_q^{c}\\ \Delta i_d^{c}\\ \Delta\theta\end{bmatrix} \tag{69}$$

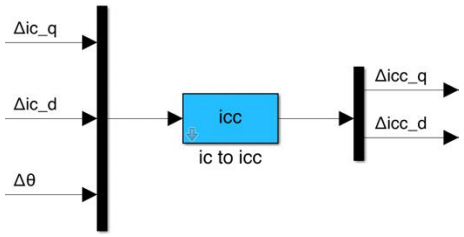

FIGURE 27 ANGLE ROTATION OF THE CURRENT FROM GRID TO CURRENT CONTROLLER – STATE-SPACE BLOCK

4.4.5 AC/DC Bus

From (6) and (7), the linearization of active and reactive power equations can be derived as

$$P = \frac{3}{2}\left(v_q i_{q0} + v_{q0} i_q + v_d i_{d0} + v_{d0} i_d\right) \tag{70}$$

$$Q = \frac{3}{2}\left(v_q i_{q0} + v_{q0} i_q - v_d i_{d0} - v_{d0} i_d\right) \tag{71}$$

Then, the state-space of the power exchanged between the AC and the DC side can be expressed as

$$\begin{aligned} \frac{d}{dt}[\Delta v_{dc}] &= \left[-\frac{P_{c0}}{C_{dc} \cdot {v_{dc0}}^2}\right] \cdot [\Delta v_{dc}] + \begin{bmatrix} \frac{1}{C_{dc}} & \frac{3v_{q0}^{cc}}{2C_{dc}v_{dc0}} & \frac{3v_{d0}^{cc}}{2C_{dc}v_{dc0}} & \frac{3i_{q0}^{c}}{2C_{dc}v_{dc0}} & \frac{3i_{d0}^{c}}{2C_{dc}v_{dc0}} \end{bmatrix} \cdot \begin{bmatrix} \Delta i_{dcm} \\ \Delta i_q^{cc} \\ \Delta i_d^{cc} \\ \Delta v_q^c \\ \Delta v_d^c \end{bmatrix} \\ \begin{bmatrix} \Delta v_{dc} \\ \Delta i_{dcl} \end{bmatrix} &= \begin{bmatrix} 1 \\ -\frac{P_{c0}}{{v_{dc0}}^2} \end{bmatrix} \cdot [\Delta v_{dc}] + \begin{bmatrix} 0 & 0 & 0 & 0 & 0 \\ 0 & \frac{3v_{q0}^{cc}}{2v_{dc0}} & \frac{3v_{d0}^{cc}}{2v_{dc0}} & \frac{3i_{q0}^{c}}{2v_{dc0}} & \frac{3i_{d0}^{c}}{2v_{dc0}} \end{bmatrix} \cdot \begin{bmatrix} \Delta i_{dcm} \\ \Delta i_q^{cc} \\ \Delta i_d^{cc} \\ \Delta v_q^c \\ \Delta v_d^c \end{bmatrix} \end{aligned} \tag{72}$$

The state-space block of the AC/DC Bus is

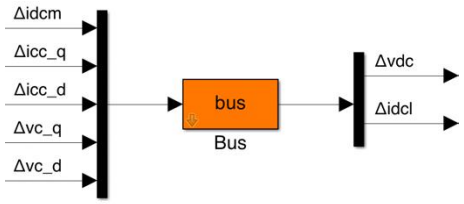

FIGURE 28 AC/DC BUS – STATE-SPACE BLOCK

4.4.6 VSC Control Mode for Reference Calculation

4.4.6.1 $\boldsymbol{P} - \boldsymbol{Q}$ Mode

An open loop of straightforward, or feedforward, implementation for the reference currents calculation from the active and the reactive power is applied in $\boldsymbol{P} - \boldsymbol{Q}$ mode whose equivalent state-space form of **Figure 29** is A, B, and $C\ matrix$ are all zero matrices, and its $D\ matrix$ is the gain whose value is $\frac{2}{3E_m}$.

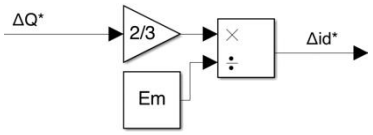

FIGURE 29 $\boldsymbol{P-Q}$ OPERATION MODE - FEEDFORWARD IMPLEMENTATION STRUCTURE

4.4.6.2 $\boldsymbol{V_{DC}-Q}$ Mode

The expression of $\boldsymbol{V_{DC}-Q}$ mode in state-space form is

$$\frac{d}{dt}\begin{bmatrix}\int v_{dc}^{*} \\ \int v_{dc}\end{bmatrix} = \begin{bmatrix}0 & 0 \\ 0 & 0\end{bmatrix}\cdot\begin{bmatrix}\int v_{dc}^{*} \\ \int v_{dc}\end{bmatrix} + \begin{bmatrix}1 & 0 \\ 0 & 1\end{bmatrix}\cdot\begin{bmatrix}v_{dc}^{*} \\ v_{dc}\end{bmatrix}$$
$$\left[i_q^{*}\right] = \begin{bmatrix}\frac{2v_{dc}^{*}}{3E_m}K_i^v & -\frac{2v_{dc}^{*}}{3E_m}K_i^v\end{bmatrix}\cdot\begin{bmatrix}\int v_{dc}^{*} \\ \int v_{dc}\end{bmatrix} + \begin{bmatrix}\frac{2v_{dc}^{*}}{3E_m}K_p^v & -\frac{2v_{dc}^{*}}{3E_m}K_p^v\end{bmatrix}\cdot\begin{bmatrix}v_{dc}^{*} \\ v_{dc}\end{bmatrix} \quad (73)$$

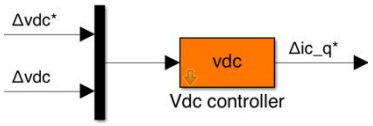

FIGURE 30 $\boldsymbol{V_{DC}-Q}$ OPERATION MODE - STATE-SPACE BLOCK

4.5 Linear model in $MATLAB/Simulink$

Figure 31 and **Figure 32** show the design of the linear state-space models of the $\boldsymbol{P-Q}$ operation mode and the $\boldsymbol{V_{DC}-Q}$ operation mode, respectively.

In **Figure 31**, each variation in active and reactive power is feed-forwarded to the current controller in the form of a current calculated by dividing each power by $\frac{3}{2}E_m$, refer to (46) and (47). The number of the state-spaces and eigenvalues of the $\boldsymbol{P-Q}$ operation mode is 8.

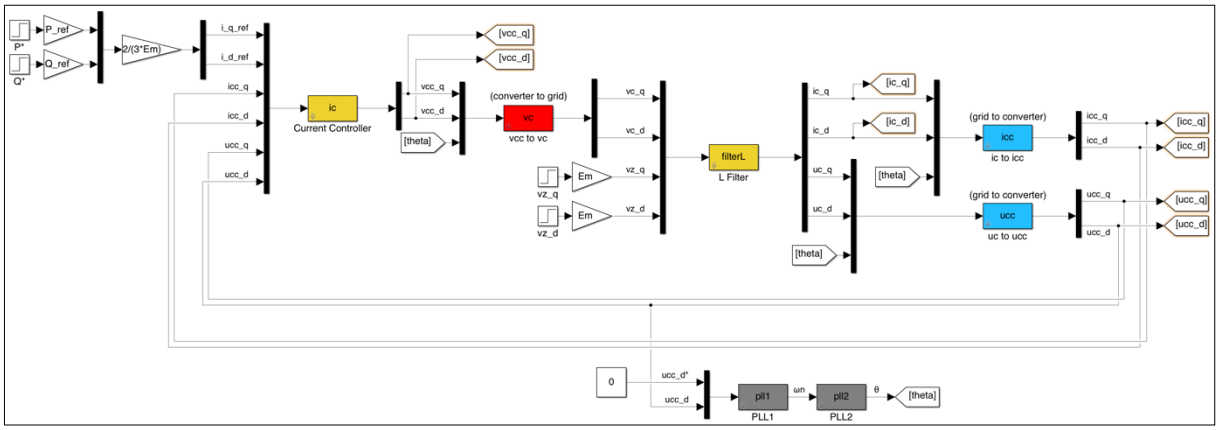

FIGURE 31 LINEAR MODEL WITH $\boldsymbol{P-Q}$ OPERATION MODE

In **Figure 32**, depending on the variation of I_{DC_m}, the value of V_{DC} changes which results in the change of the reference current i_q^*. The procedure to calculate i_q^{c*} is exactly same to that of the $\boldsymbol{P-Q}$ operation mode, the feedforward implementation. As a result, due to the addition of the state-space block v_{DC}, the number of state-spaces and eigenvalues in the $\boldsymbol{V_{DC}-Q}$ operation mode is 9.

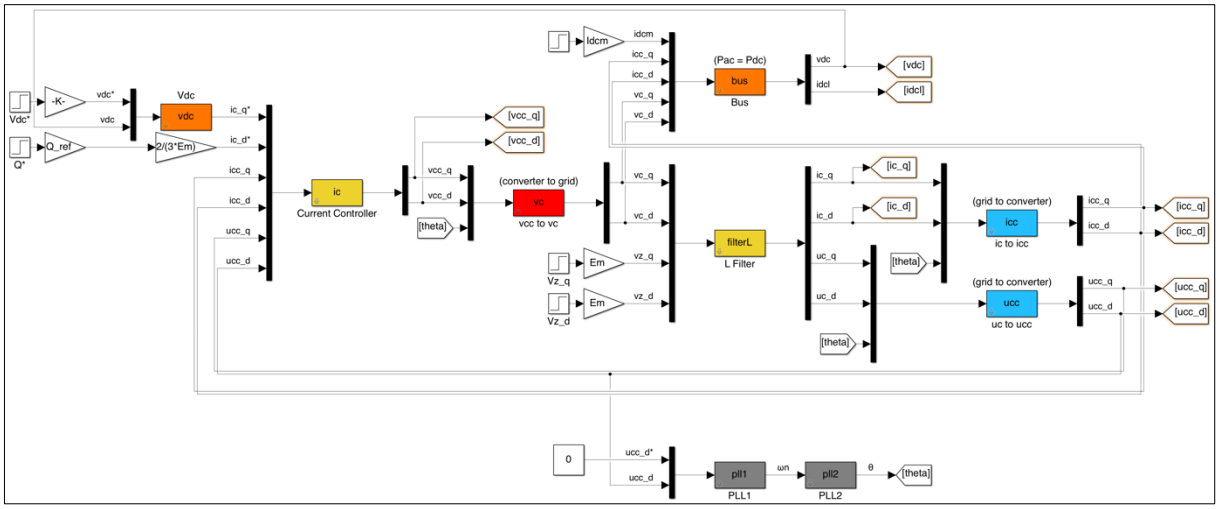

FIGURE 32 LINEAR MODEL WITH $\boldsymbol{V_{DC}-Q}$ OPERATION MODE

4.6 Validation of the Linear VSC models

Figure 33 to **Figure 38** represent the results from two kinds of simulations of the linear and the nonlinear model with two different operation modes, with zoom in the section from $1.995\,sec$ to $2.05\,sec$. One is the case which the external disturbance current I_{DCm} has the step variable of 1% for the active power variation, and the other is the case when 1% step-up of Q is applied for the reactive power variation. It is observed that the currents and voltages in $qd-$frame from two models are exactly matched in both cases of I_{DCm} and Q variations. Consequently, it is validated that the linearization of the non-linear VSC model within the simulation time is successful.

I_{DCm} : 1% step up

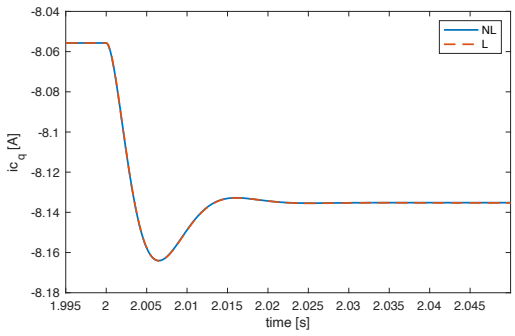

Q : 1% step up

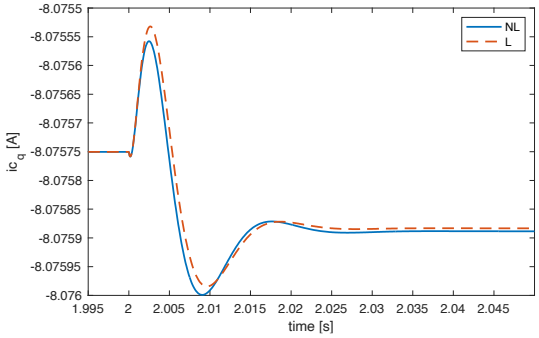

FIGURE 33 SIMULATION RESULTS OF THE CURRENTS $-\boldsymbol{i_q^c}$

I_{DCm} : 1% step up

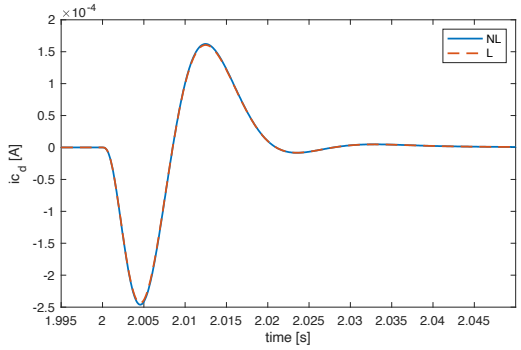

Q : 1% step up

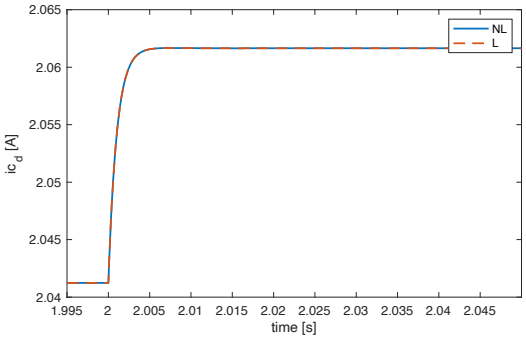

FIGURE 34 SIMULATION RESULTS OF THE CURRENTS $-\boldsymbol{i_d^c}$

I_{DCm} : 1% step up

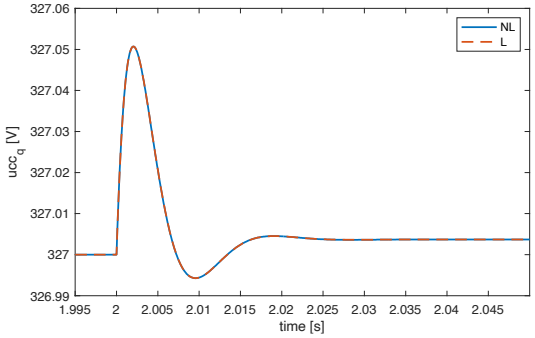

Q : 1% step up

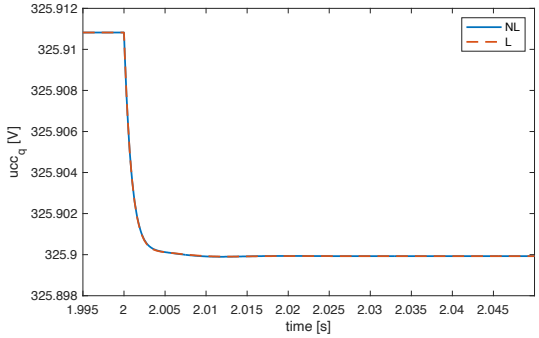

FIGURE 35 SIMULATION RESULTS OF THE CURRENT CONTROLLER INPUT VOLTAGE $-\boldsymbol{u_q^{cc``}}$

I_{DCm} : 1% step up

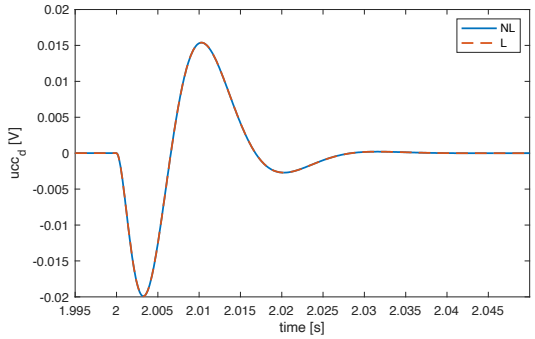

Q : 1% step up

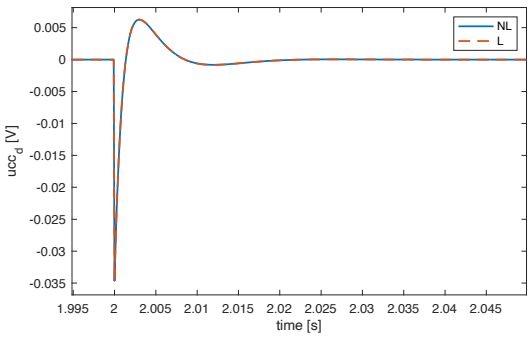

FIGURE 36 SIMULATION RESULTS OF THE CURRENT CONTROLLER INPUT VOLTAGE $-\boldsymbol{u_d^{cc}}$

I_{DCm} : 1% step up

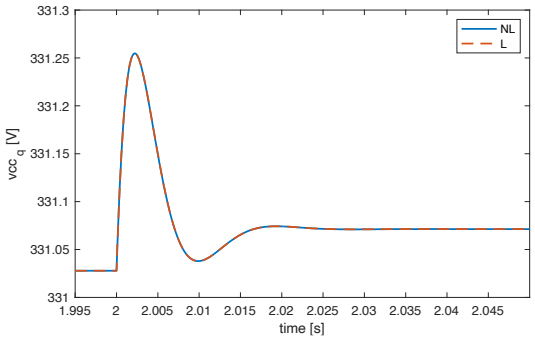

Q : 1% step up

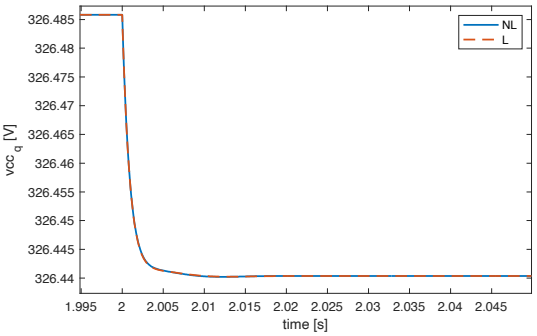

FIGURE 37 SIMULATION RESULTS OF THE CURRENT CONTROLLER OUTPUT VOLTAGE $-\boldsymbol{v_q^{cc}}$

I_{DCm} : 1% step up

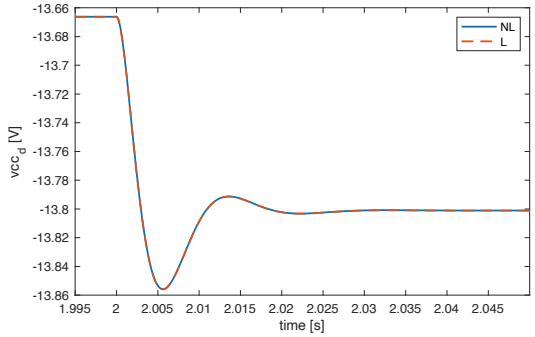

Q : 1% step up

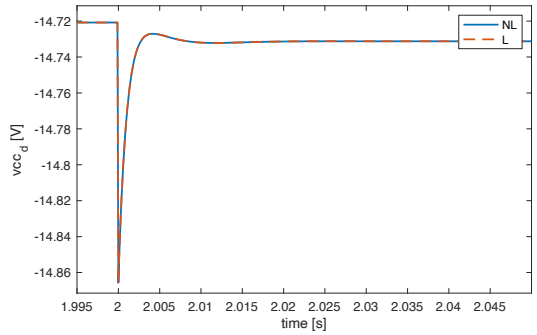

FIGURE 38 SIMULATION RESULTS OF THE CURRENT CONTROLLER OUTPUT VOLTAGE $-\boldsymbol{v_d^{cc}}$

I_{DCm} : 1% step up

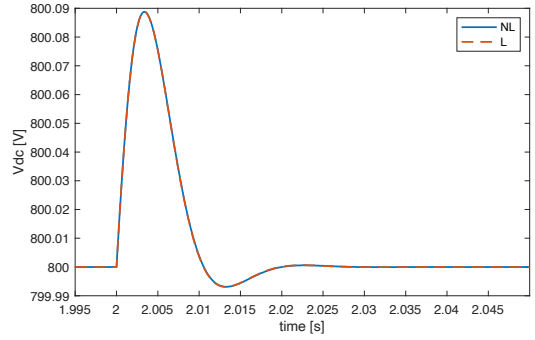

Q : 1% step up

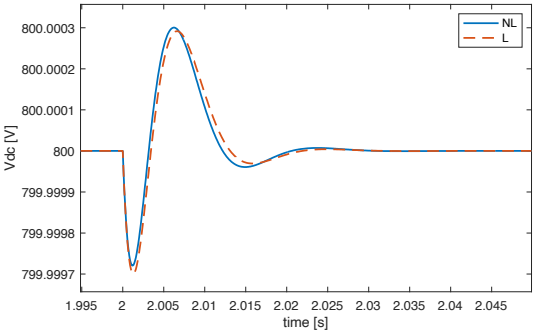

FIGURE 39 SIMULATION RESULTS OF THE CURRENT CONTROLLER OUTPUT VOLTAGE $-\boldsymbol{V_{DC}}$

I_{DCm} : 1% step up

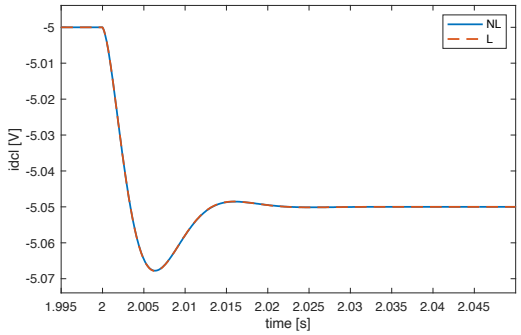

Q : 1% step up

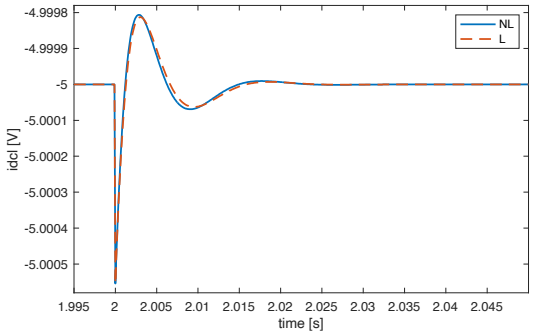

FIGURE 40 SIMULATION RESULTS OF THE CURRENT CONTROLLER OUTPUT VOLTAGE $-\boldsymbol{I_{DC_l}}$

5. Case Studies and Comparison

In the simulation, the 1% step-up of the external disturbance direct current I_{DCm}, whose initial value is 5A, is applied at 2 seconds. This chapter focuses on the investigation of the effect of each control parameter of the designed VSC controller on the responses of currents i_{qd}^{c} and the voltages u_{qd}^{cc} and v_{qd}^{cc}.

It is well known that how each gain parameter affects control in a PID control system, as shown in **Figure 41**.

Increase of	**Rise Time** t_R	**Overshoot / Oscillation** os / M_P	**Settling time** t_{SS}	**Steady-state Error** e_{SS}	**Stability**
K_P	Decrease ↘	Increase ↗	Small Change	Decrease ↘	Degrade ↘
K_I	Decrease ↘	Increase ↗	Increase ↗	Great Decrease ↘ / Eliminate	Degrade ↘
K_D	Minor Change / Small Decrease ↘	Decrease ↘	Decrease ↘	Small Change / None (Theoretical)	Improve ↗ (if K_D is small)

FIGURE 41 EFFECTS OF INCREASING GAINS OF PID CONTROL INDEPENDENTLY [22,23]

In **5.1**, the changes in the current and voltage responses of the designed VSC controller for each case of changing the control parameters are compared, referring to the description in **Figure 41**.

Lastly, in **5.3**, as the way of examining the effect of changes in state variables on impedance, a bode plot showing the value of admittance in the frequency range of $10^{-1}\,Hz$ to $10^{4}\,Hz$ is used.

5.1 Changes in Control Parameters

5.1.1 Variation of Short Circuit Power S_{SC}

The decrease in S_{sc} results in the increase in L_g and R_g, refer to (12) and (13), which is defined as a weak grid. As the grid impedances increase, the oscillation amplitudes of voltages and currents decrease. The comparison of cases when S_{sc} is 5 times larger and 5 times smaller are compared in **Figure 42**.

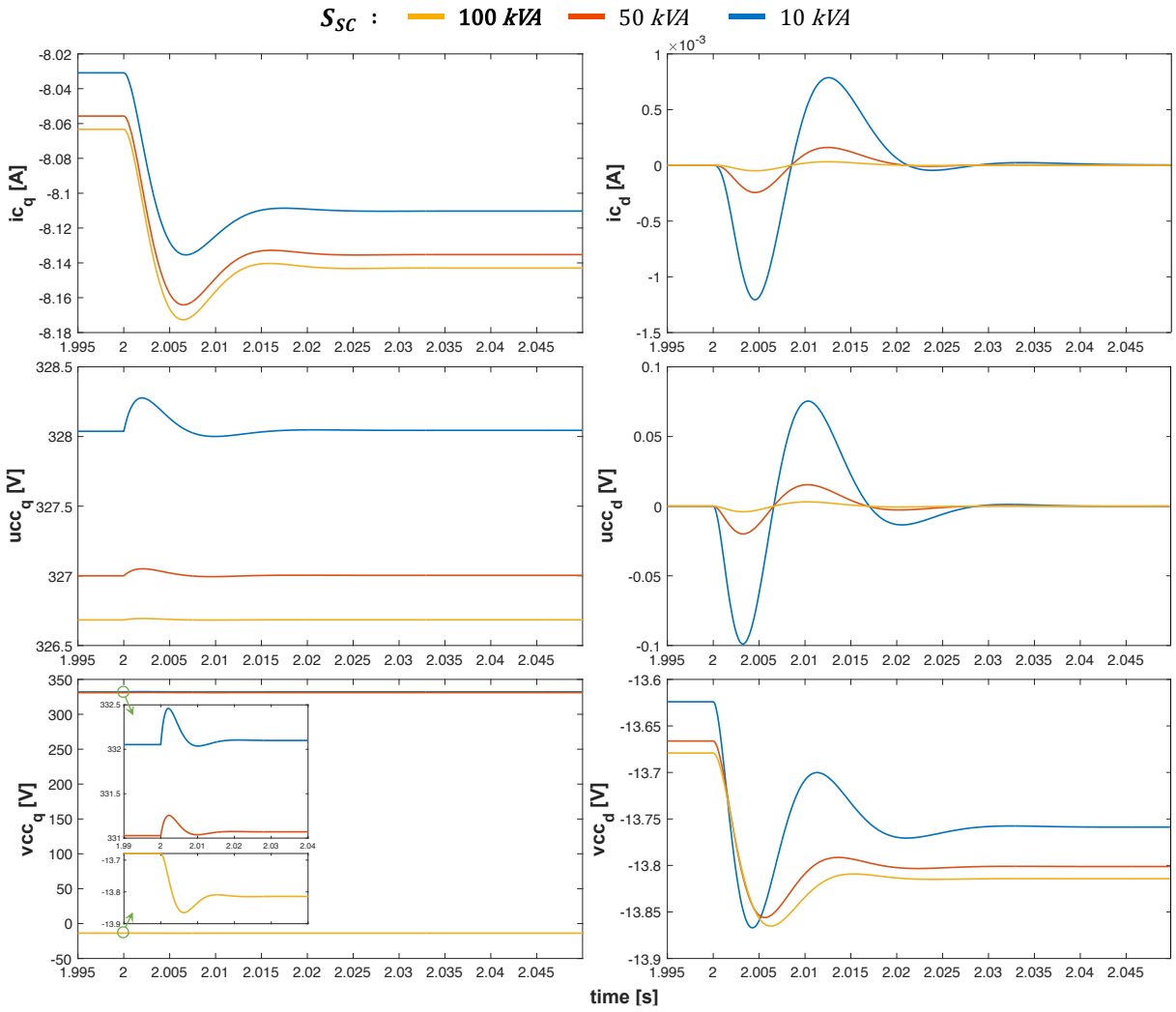

FIGURE 42 THE CASE OF S_{SC} VARIATION

5.1.2 Variation of Current Controller – Time Constant τ_{ic}

τ_{ic}, determining the time of output reaching 62.3% of the steady-state value, also affects the system stability. Therefore, as τ_{ic} increases, each settling time t_{SS} for current i_{qd}^{c} and voltages v_{qd}^{cc} and u_{qd}^{cc}, to reach the steady-state become larger, as shown in **Figure 43**.

However, the larger the value of τ_{ic}, the smaller the peak value of current i_{qd}^{c} while the larger the peak value of voltages v_{qd}^{cc} and u_{qd}^{cc}.

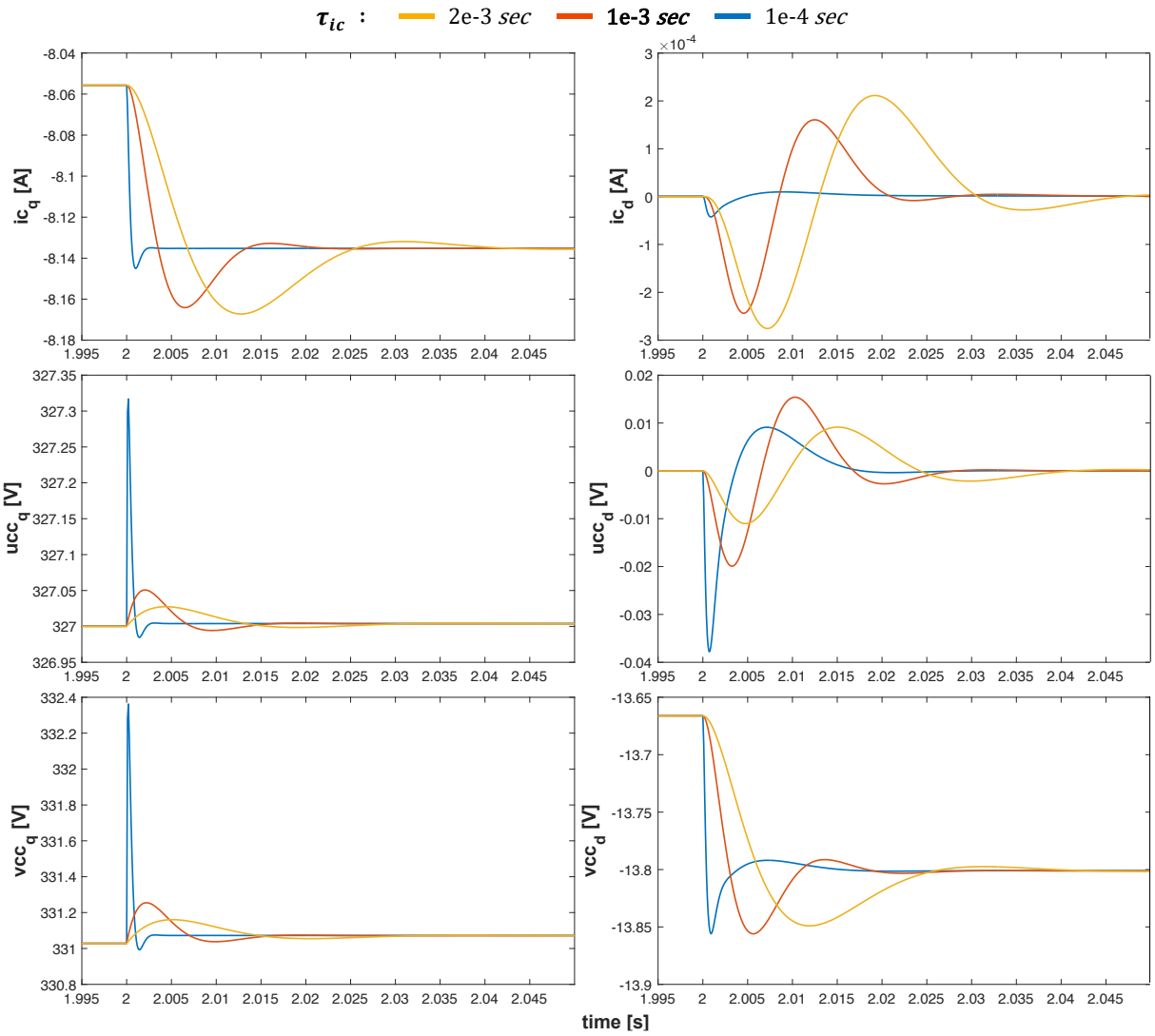

FIGURE 43 THE CASE OF τ_{ic} VARIATION

5.1.3 Variation of Grid Nominal Frequency ω_n

According to the controller design, ω_n is inversely proportional to τ_{PLL}, and directly proportional to K_p^{PLL} and the square root of K_i^{PLL}.

Thus, as ω_n decreases, the overshoot is expected to increase. In the case of i_{qd}^c and v_{qd}^{cc}, the prediction is true, but the overshoot of u_{qd}^{cc} exceptionally decreases, as shown in **Figure 44**.

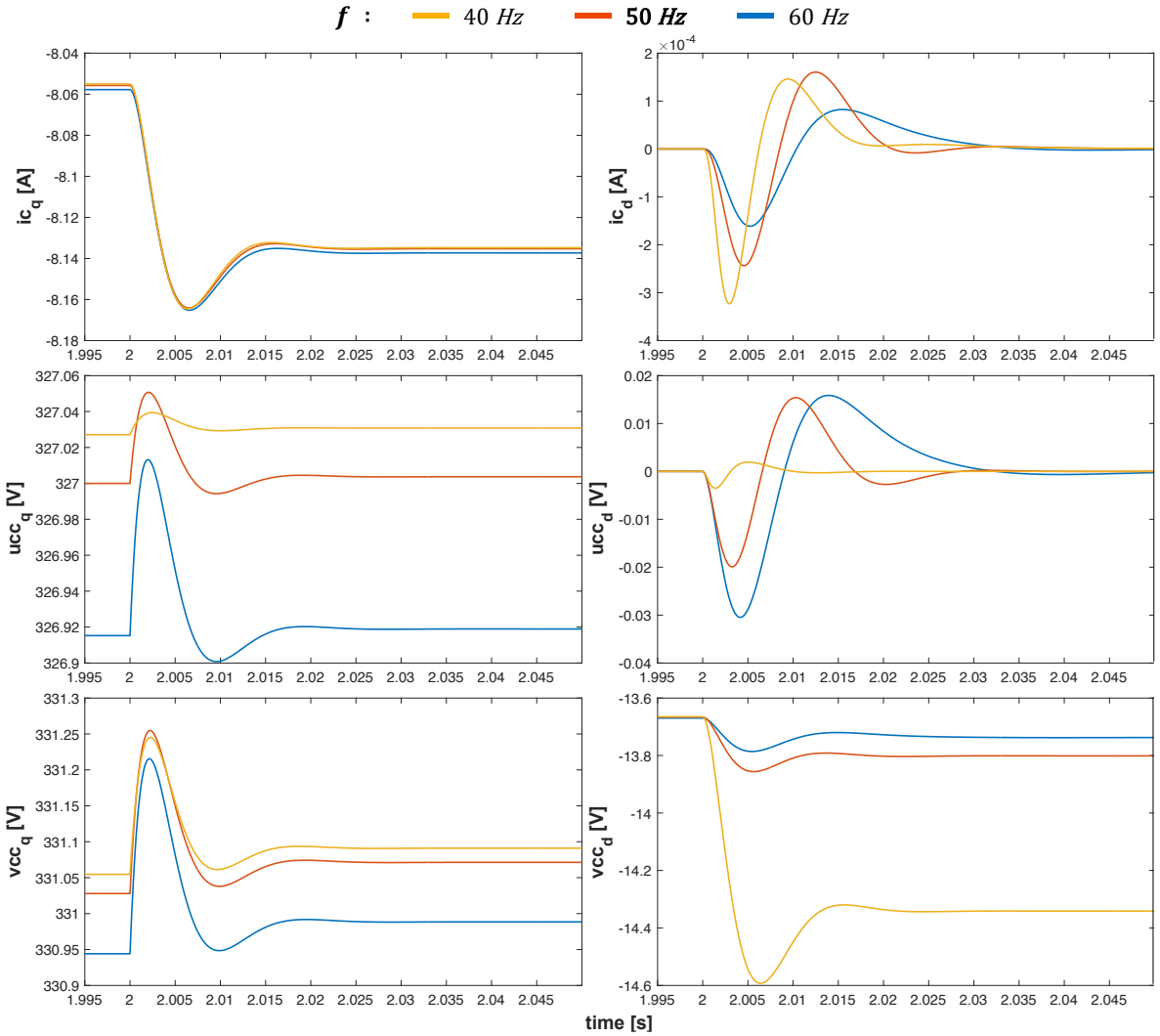

FIGURE 44 THE CASE OF ω_n VARIATION

From the gain parameters of the PLL expressed in (17) to (20), the following relations can be derived. When ω_n increases, τ_{PLL} decreases, whereas K_p^{PLL} and K_i^{PLL} increases, whose impacts on the controller are described in **Figure 41**.

5.1.4 Variation of DC Voltage Controller – Frequency ω_V

As the frequency of the voltage controller ω_V increases, so do the gain parameters K_p^V and K_i^V whose relations are expressed in (51) to (54). The increase of parameters makes the maximum oscillation larger and settles to the steady-state faster. The comparison when the proportional factor of the DC voltage controller α_V varies from 0.04 to 0.06, given that the initial value is 0.05.

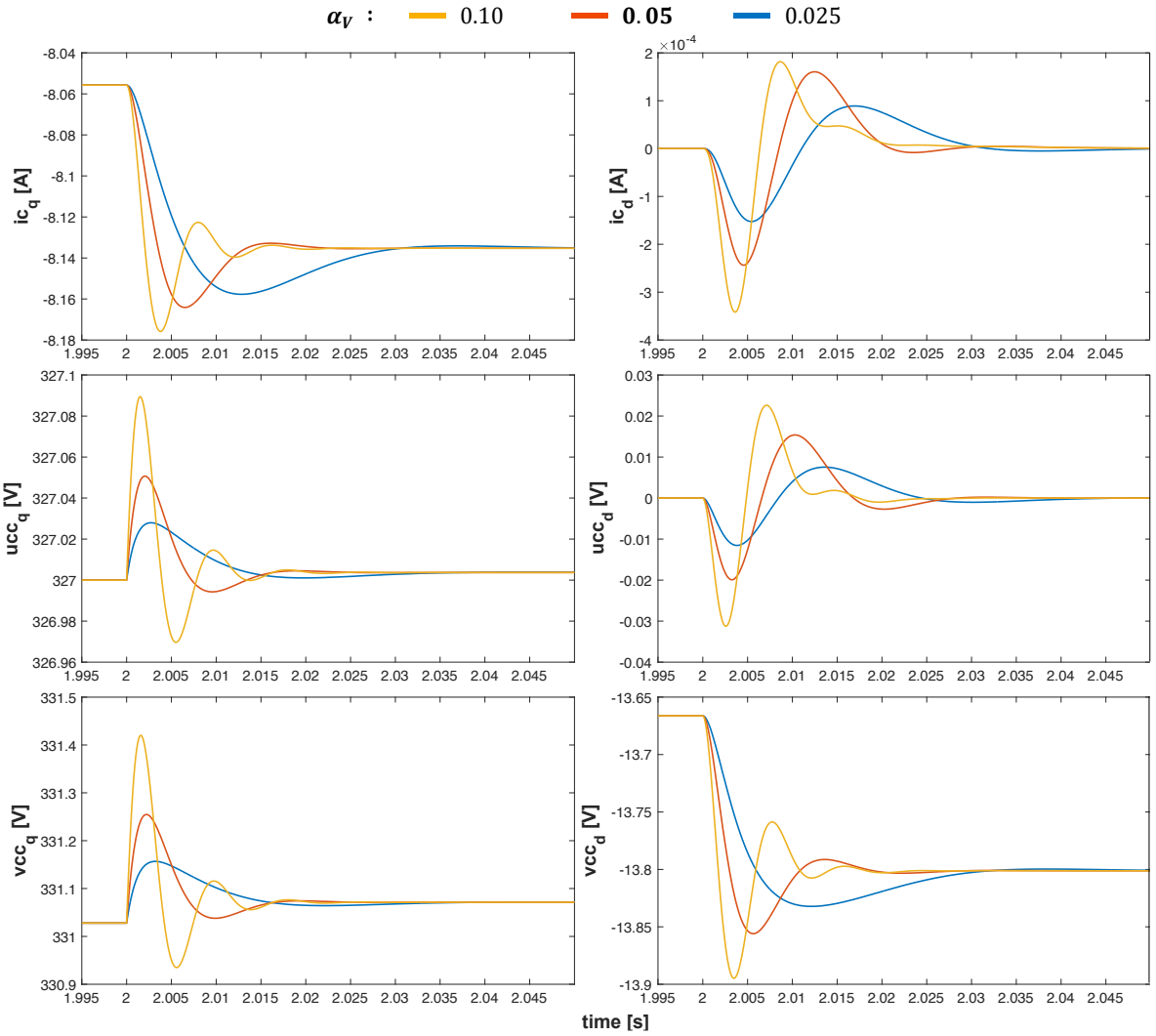

FIGURE 45 THE CASE OF ω_V VARIATION

5.1.5 Variation of Phase Locked Loop – Damping Ratio ζ_{PLL}

When noted from (17) to (20) again, the significant effects of increasing ζ_{PLL} are the increases in τ_{PLL}, and K_p^{PLL}. This results in a larger overshoot, a steeper slope of which is $1/\tau_{PLL}$, the decrease of the settling time in the d −coordinate for current i_d^c, and voltages v_d^{cc} and u_d^{cc} as ζ_{PLL} decreases, as shown in **Figure 46**.

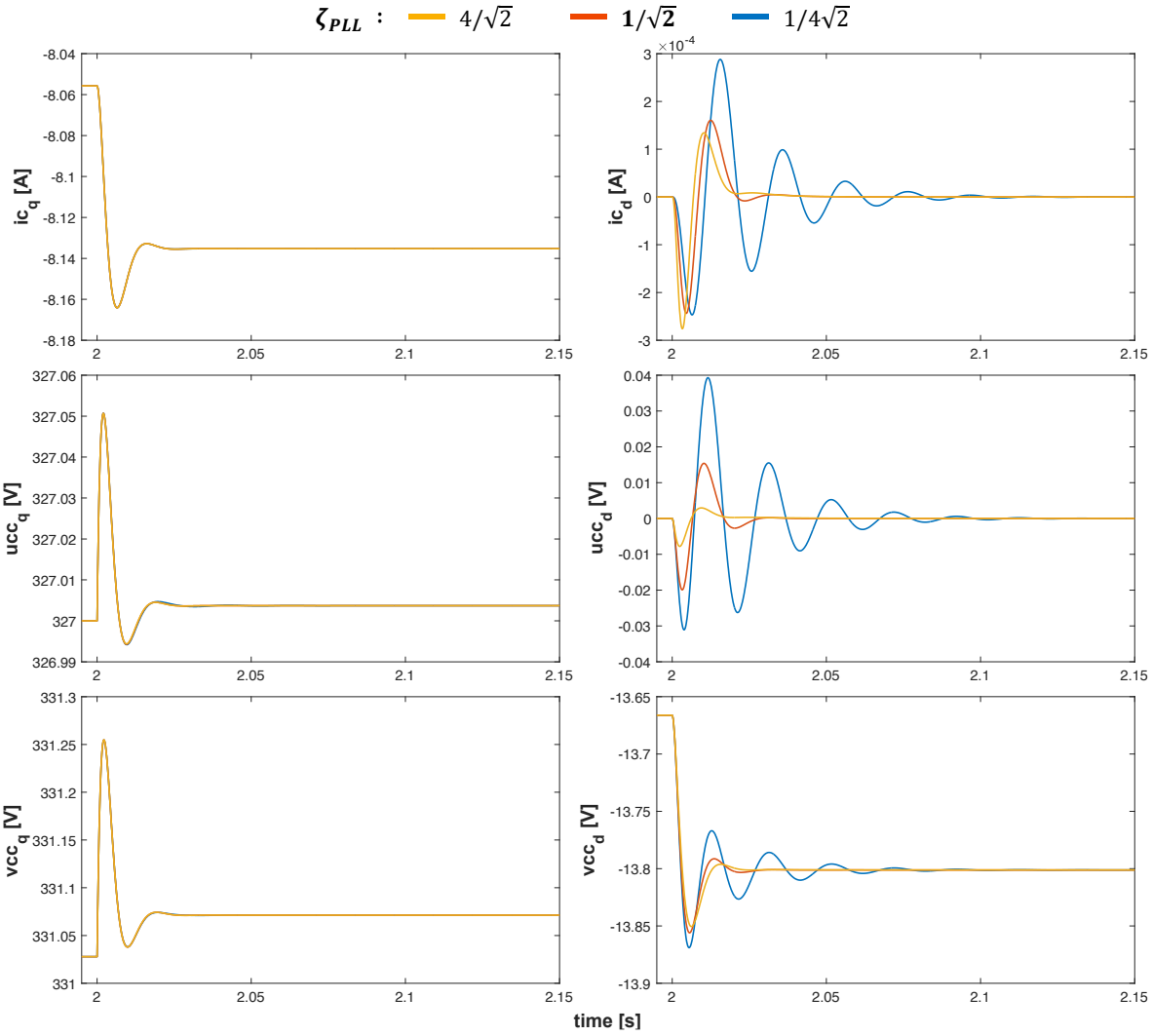

FIGURE 46 THE CASE OF ζ_{PLL} VARIATION

5.1.6 Variation of DC Voltage Controller – Damping Ratio ζ_V

The damping ratio of the DC voltage controller ξ_V is proportional to K_p^V refer to (51), and affects current i_{qd}^c, voltages v_{qd}^{cc} and u_{qd}^{cc} in the dq −coordinate, as shown in **Figure 47**. The currents and the voltages tend to oscillate faster as ξ_V increases. However, regarding overshoots, the $d-$coordinate current i_d^c and the q −coordinate voltages v_q^{cc} and u_q^{cc} have larger overshoots whereas the others have smaller overshoots in the same condition at which ξ_V increases.

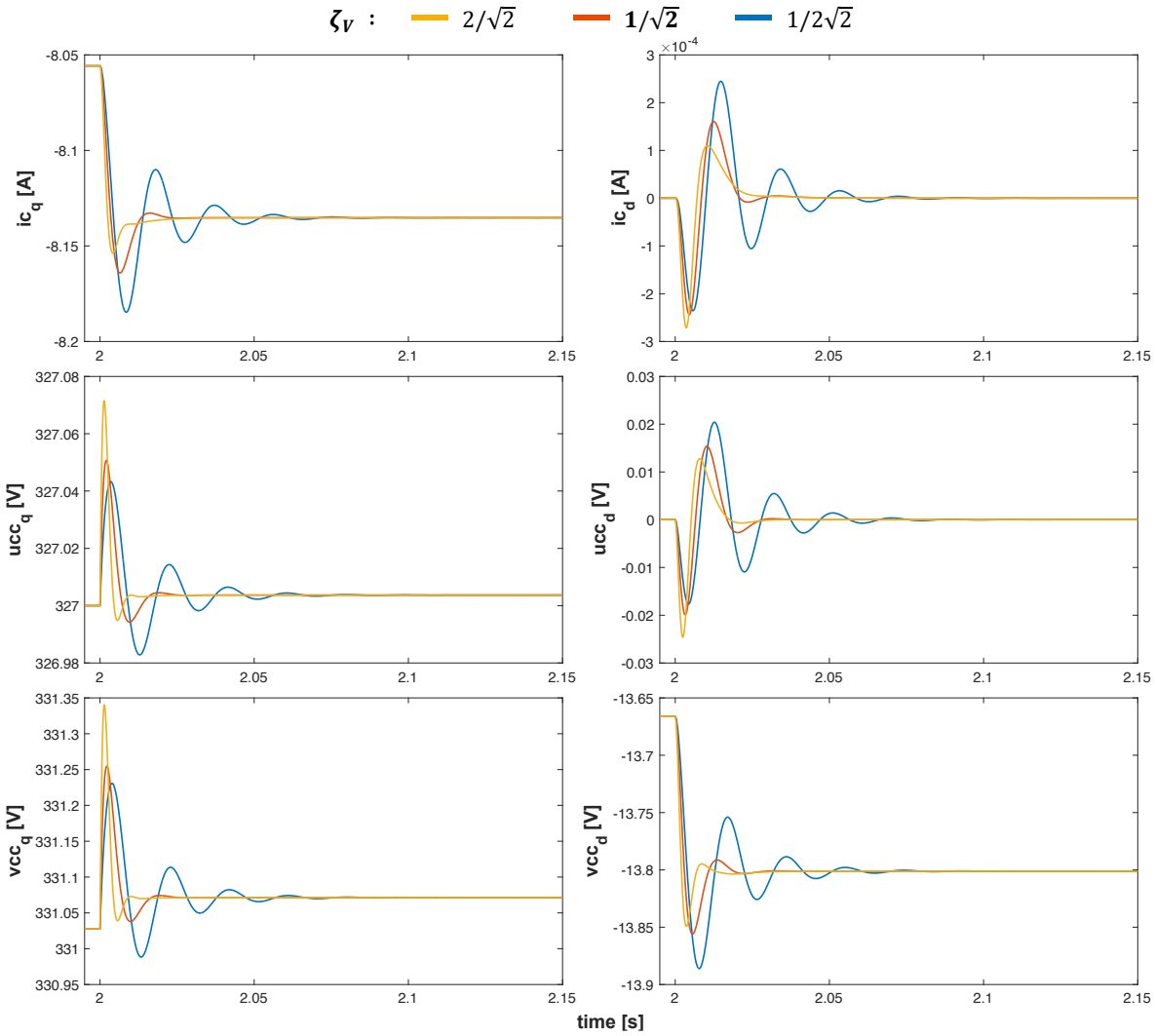

FIGURE 47 THE CASE OF ξ_V VARIATION

5.2 Eigenvalue Analysis

In this chapter, the impact of changing each parameter of the controller is analyzed through the eigenvalue analysis.

The eigenvalues of the $A\ matrix$ are the poles of the system, and the location of the poles dictates the stability of a linear system. The step response of a second-order system as a function of eigenvalues and damping ratio is shown in **Figure 48**. One or more positive real parts of an eigenvalue represent the instability of the system.

Eigenvalue	Effect on system when disturbed	ξ
a) All real, positive	Exponential increase, driven away from the steady-state value	-
b) All real, negative	Overdamped, driven back to the steady-state value	$\xi > 1$
	Critically damped, driven back to the steady-state value	$\xi = 0$
c) 0	Static, remains at position to which it was disturbed	-
d) Identical to another eigenvalue	Effects cannot be determined	-
e) Complex, one or more positive real	Oscillates around steady-state value with increasing amplitude	-
f) Complex, one or more negative real	Underdamped, oscillates around steady-state value with decreasing amplitude	$0 < \xi < 1$
g) Imaginary	Undamped, oscillates around steady-state value with constant amplitude	$\xi = 0$

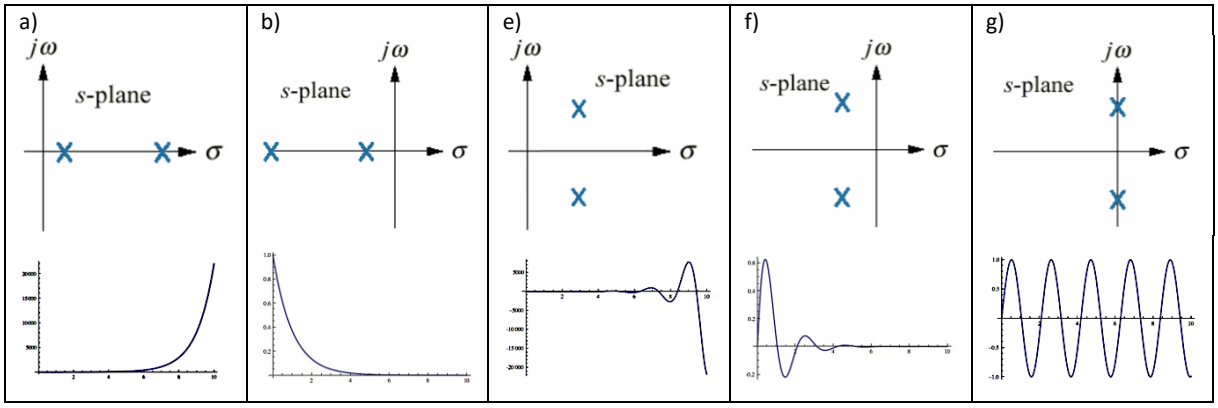

FIGURE 48 STEP RESPONSE OF A SECOND-ORDER SYSTEM [24]

From the state-space model, as shown in **Figure 32**, the whole system can be expressed with one unified state-space by interconnecting all state-spaces. The configuration of state variables, inputs, and outputs of the state-space is shown in **Figure 49**.

State-space	***State x***	***Input u***	***Output y***
PPL 1	$\int u_d^{cc*}$, $\int u_d^{cc}$	u_d^{cc*}, u_d^{cc}	ω_n
PPL 2	θ	ω_n	θ
filter L	i_q^c , i_d^c	v_q^z, v_d^z, v_q^c, v_d^c	i_q^c, i_d^c, u_q^c, u_d^c
icc		i_q^c, i_d^c, θ	i_q^{cc}, i_d^{cc}
ucc		u_q^c, u_d^c, θ	u_q^{cc}, u_d^{cc}
ic	$\int i_q^{c*}$, $\int i_d^{c*}$, $\int i_q^c$, $\int i_d^c$	i_q^{c*}, i_d^{c*}, i_q^{cc}, i_d^{cc}, u_q^c, u_d^c	v_q^{cc} , v_d^{cc}
vc		v_q^{cc}, v_d^{cc}, θ	v_q^c, v_d^c
bus	v_{DC}	i_{DC_m}, i_q^{cc}, i_d^{cc}, v_q^c, v_d^c	v_{DC}, i_{DC_l}
vdc	$\int v_{DC}{}^*$, $\int v_{DC}$	$v_{DC}{}^*$, v_{DC}	i_q^{c*}

Figure 49 STATE-SPACE VARIABLES FOR EIGENVALUE ANALYSIS

5.2.1 S_{sc} Variation

Refer to the grid modeling done, from (12) and (13), the decrease in S_{sc} means the increase in the grid impedance, referred to as the weak grid.

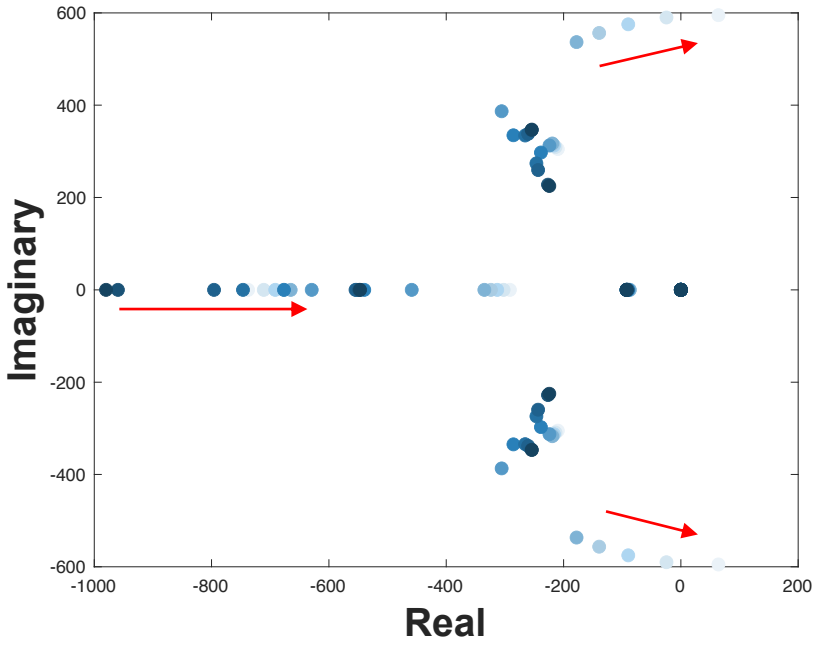

100 kVA	x 10		x 5		x 1		x 0.8		x 0.6		x 0.4		x 0.2		x 0.18		x 0.16		x 0.14		x 0.12	
lambda	Re	Im	Re	Im	Re	Im	Re	Im	Re	Im	Re	Im	Re	Im	Re	Im	Re	Im	Re	Im	Re	Im
λ_1	-980	0	-960	0	-796	0	-746	0	-677	0	-635	0	-178	537	-139	556	-90	575	-25	590	57	615
λ_2	-547	0	-548	0	-555	0	-553	0	-540	0	-280	448	-178	-537	-139	-556	-90	-575	-25	-590	57	-615
λ_3	-254	347	-254	346	-260	338	-265	334	-285	335	-280	-448	-665	0	-677	0	-691	0	-711	0	-774	0
λ_4	-254	-347	-254	-346	-260	-338	-265	-334	-285	-335	-394	0	-219	317	-218	315	-216	313	-214	309	-196	290
λ_5	-224	225	-226	228	-243	260	-246	274	-239	297	-221	318	-219	-317	-218	-315	-216	-313	-214	-309	-196	-290
λ_6	-224	-225	-226	-228	-243	-260	-246	-274	-239	-297	-221	-318	-335	0	-324	0	-313	0	-302	0	-290	0
λ_7	0	0	0	0	-0	0	0	0	0	0	0	0	0	0	-0	0	0	0	0	0	0	0
λ_8	-92	0	-92	0	-91	0	-91	0	-90	0	-89	0	-87	0	-87	0	-87	0	-87	0	-87	0
λ_9	93	0	-93	0	-93	0	-93	0	-93	0	-93	0	-93	0	-93	0	-93	0	-93	0	-93	0

FIGURE 50 EIGENVALUE - S_{SC} VARIATION

Figure 50 gives the change of eigenvalues when S_{sc} varies from 10 times to 0.12 times the initial value of $100\ kVA$. As a whole, eigenvalues move toward left as S_{sc} decreases, which causes larger overshoot with slower response of oscillation. The most important result in **Figure 50** is that λ_1 and λ_2 come to have the real positive parts, implying the grid system become unstable as grid impedance increases.

5.2.2 τ_{ic} Variation

The variation in the time constant of the inner current controller τ_{ic} determines how fast the output of the controller reach the $63.2\ \%$ of the targeted steady-state value.

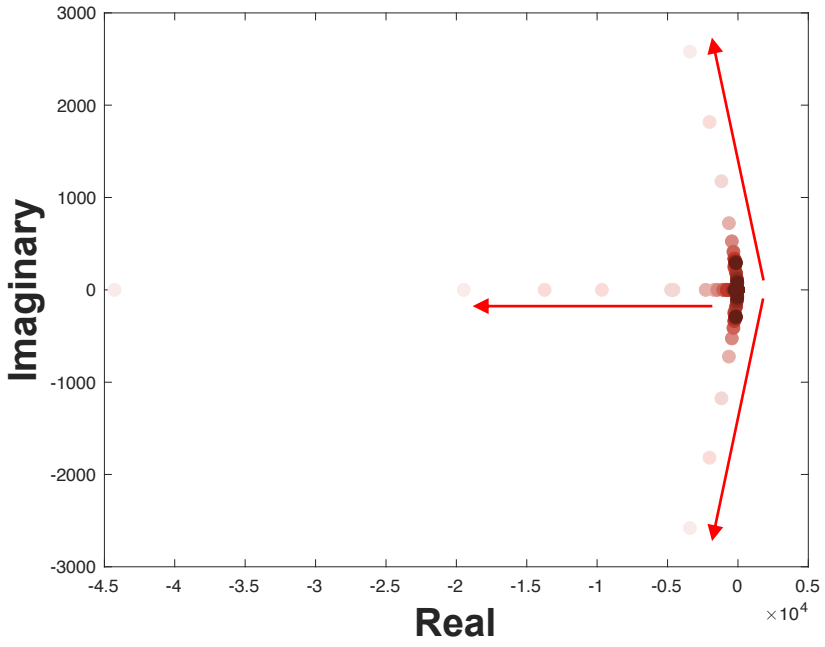

0.001	x 5		x 4		x 3		x 2		x 1		x 0.8		x 0.6		x 0.4		x 0.2		x 0.1		x 0.05	
lambda	Re	Im	Re	Im	Re	Im	Re	Im	Re	Im	Re	Im	Re	Im	Re	Im	Re	Im	Re	Im	Re	Im
λ_1	-149	288	-160	298	-180	307	-217	308	-796	0	-1047	0	-1464	0	-2291	0	-4757	0	-9664	0	-44277	0
λ_2	-149	-288	-160	-298	-180	-307	-217	-308	-555	0	-717	0	-1011	0	-1699	0	-4586	0	-13732	0	-19481	0
λ_3	-211	0	-236	0	-278	0	-368	0	-260	338	-325	413	-433	526	-641	722	-1174	1176	-2020	1817	-3414	2581
λ_4	0	0	-57	92	-78	122	-266	0	-260	-338	-325	-413	-433	-526	-641	-722	-1174	-1176	-2020	-1817	-3414	-2581
λ_5	-44	74	-57	-92	-78	-122	-121	179	-243	260	-242	247	-238	239	-233	232	-228	228	-226	226	-225	225
λ_6	-44	-74	-0	0	-0	0	-121	-179	-243	-260	-242	-247	-238	-239	-233	-232	-228	-228	-226	-226	-225	-225
λ_7	-80	0	-84	0	-178	0	-0	0	-0	0	-0	0	-0	0	0	0	0	0	-0	0	-0	0
λ_8	-111	0	-136	0	-87	0	-89	0	-91	0	-91	0	-92	0	-92	0	-92	0	-92	0	-93	0
λ_9	-93	0	-93	0	-93	0	-93	0	-93	0	-93	0	-93	0	-93	0	-93	0	-93	0	-93	0

FIGURE 51 EIGENVALUE - τ_{ic} VARIATION

In **Figure 51**, it is seen that the change of τ_{ic}, from 5 times to 0.05 times the initial value of $0.001\ sec$, does not affect the stability.

However, the significance of the figure is the radical movement of the pair of the poles. A vertical direction that the absolute value of the imaginary part increases means the overshoot is increasing but the envelop is the same. Moreover, it also moves a bit to the left so the envelop of the oscillation is affected by the change in τ_{ic}.

In addition, the rapid movement in a horizontal direction to the left which the real part decreases, yields the response damps out faster as τ_{ic} decreases when the frequency is constant.

5.2.3 ω_n Variation

The observation of the electrical angular velocity of the grid ω_n when it changes from 7.25 times to 0.5 times the initial value, of which is $2 \cdot \pi \cdot 50 \approx 314.1592$ is presented in **Figure 52**.

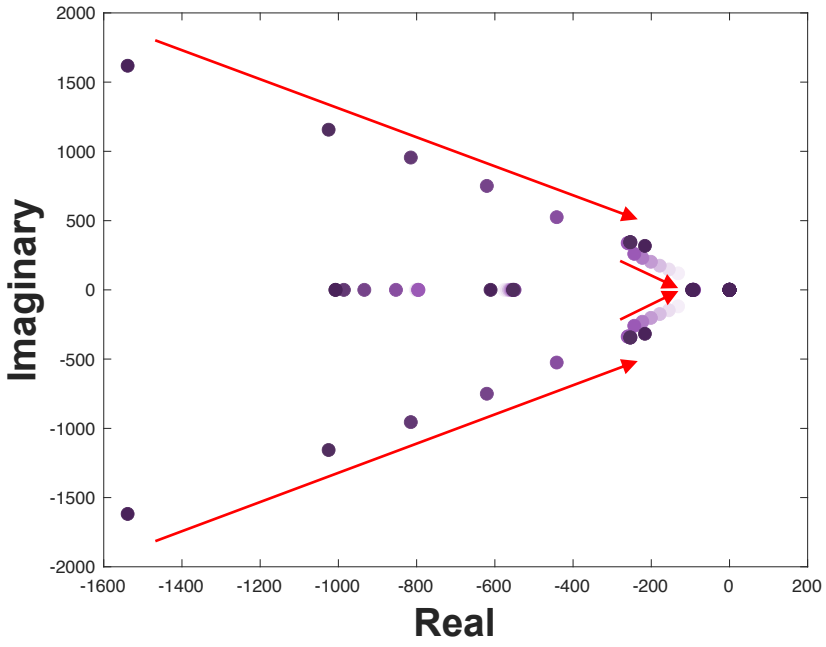

50 Hz	x 7.25		x 5		x 4		x 3		x 2		x 1		x 0.9		x 0.8		x 0.7		x 0.6		x 0.5	
lambda	Re	Im	Re	Im	Re	Im	Re	Im	Re	Im	Re	Im	Re	Im	Re	Im	Re	Im	Re	Im	Re	Im
λ_1	-1539	1618	-1025	1156	-815	955	-620	750	-853	0	-796	0	-795	0	-796	0	-797	0	-799	0	-802	0
λ_2	-1539	-1618	-1025	-1156	-815	-955	-620	-750	-442	525	-555	0	-557	0	-560	0	-564	0	-569	0	-575	0
λ_3	-1007	0	-1008	0	-986	0	-934	0	-442	-525	-260	338	-259	338	-258	337	-258	336	-257	334	-257	331
λ_4	-611	0	-554	0	-552	0	-551	0	-549	0	-260	-338	-259	-338	-258	-337	-258	-336	-257	-334	-257	-331
λ_5	-216	317	-254	344	-254	344	-254	344	-253	342	-243	260	-223	231	-201	203	-178	175	-155	147	-131	119
λ_6	-216	-317	-254	-344	-254	-344	-254	-344	-253	-342	-243	-260	-223	-231	-201	-203	-178	-175	-155	-147	-131	-119
λ_7	0	0	0	0	0	0	-0	0	-0	0	-0	0	-0	0	0	0	-0	0	-0	0	0	0
λ_8	-96	0	-95	0	-94	0	-94	0	-93	0	-91	0	-91	0	-91	0	-90	0	-90	0	-91	0
λ_9	-93	0	-93	0	-93	0	-93	0	-93	0	-93	0	-93	0	-93	0	-93	0	-93	0	-93	0

FIGURE 52 EIGENVALUE - ω_n VARIATION

There are two of remarkable pairs moving toward 0 with decrease in real and imaginary parts. The radial movements of these two sets of poles verifies the trend in **Figure 44**, which is the variation in overshoots and the faster oscillation response as ω_n decreases.

5.2.4 ω_V Variation

Refer to (54), ω_V is proportional to α_V. So, it can be said that **Figure 53** gives the transitions of eigenvalues when the frequency of the DC voltage controller changes from 4 times to 0.01 times the initial value of ω_V when $\alpha_V = 0.05$.

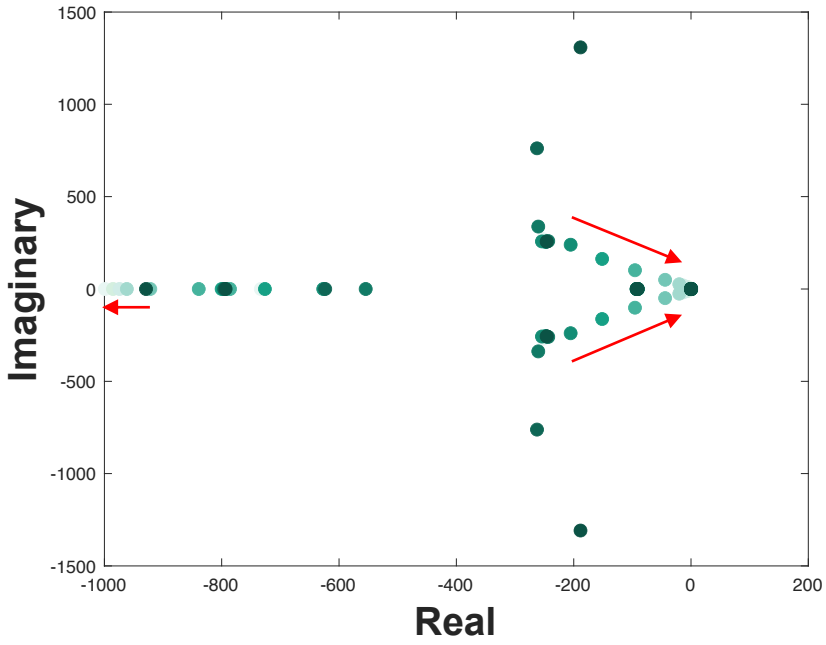

α_V =0.05	x 4		x 2		x 1		x 0.8		x 0.6		x 0.4		x 0.2		x 0.1		x 0.07		x 0.04		x 0.01	
lambda	Re	Im	Re	Im	Re	Im	Re	Im	Re	Im	Re	Im	Re	Im	Re	Im	Re	Im	Re	Im	Re	Im
λ_1	-188	1308	-263	762	-796	0	-797	0	-800	0	-786	0	-791	0	-792	0	-974	0	-985	0	-999	0
λ_2	-188	-1308	-263	-762	-555	0	-627	0	-726	0	-839	0	-922	0	-962	0	-789	0	-790	0	-733	0
λ_3	-793	0	-795	0	-260	338	-254	258	-249	256	-248	256	-247	256	-247	257	-247	257	-247	257	-253	270
λ_4	-929	0	-624	0	-260	-338	-254	-258	-249	-256	-248	-256	-247	-256	-247	-257	-247	-257	-247	-257	-253	-270
λ_5	-246	257	-246	257	-243	260	-205	240	-152	163	-96	102	0	0	-0	0	0	0	0	0	0.815	1.94
λ_6	-246	-257	-246	-257	-243	-260	-205	-240	-152	-163	-96	-102	-44	50	-20	26	-13	18.4	-6.09	11.3	0.815	-1.94
λ_7	0	0	-0	0	-0	0	-0	0	0	0	0	0	-44	0	-20	-26	-13	-18.4	-6.09	-11.3	0	0
λ_8	-91	0	-91	0	-91	0	-91	0	-91	0	-91	0	-91	0	-91	0	-90.9	0	-90.9	0	-90.9	0
λ_9	-93	0	-93	0	-93	0	-93	0	-93	0	-93	0	-93	0	-93	0	-92.6	0	-92.6	0	-92.6	0

FIGURE 53 EIGENVALUE - ω_V VARIATION

Observing the eigenvalues' trend as ω_V decreases, one of pairs of eigenvalues head to the origin and it proves the more rapid system response, and it is induced that the other eigenvalue moving left along the real axis brings out the increase in overshoot as shown in **Figure 45**.

When ω_V decreases until its value become 0.01 times the initial value, λ_5 and λ_6 come to have positive real parts, so the system is unstable.

5.2.5 ξ_{PLL} Variation

In **Figure 54**, the movements of eigenvalues when ξ_{PLL} changes from 4 time to 0.03 times the initial value of $1/\sqrt{2}$ are plotted.

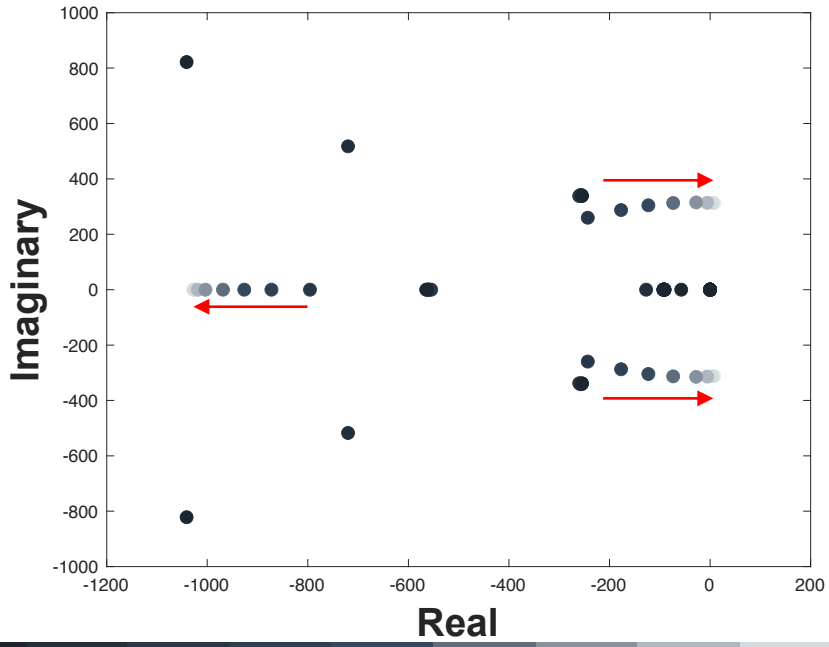

$1/\sqrt{2}$	x 4		x 2		x 1		x 0.8		x 0.6		x 0.4		x 0.2		x 0.1		x 0.05		x 0.04		x 0.03	
lambda	Re	Im	Re	Im	Re	Im	Re	Im	Re	Im	Re	Im	Re	Im	Re	Im	Re	Im	Re	Im	Re	Im
λ_1	-1041	822	-720	517	-796	0	-872	0	-927	0	-969	0	-1004	0	-1019	0	-1026	0	-1028	0	-1029	0
λ_2	-1041	-822	-720	-517	-555	0	-558	0	-559	0	-560	0	-561	0	-561	0	-561	0	-561	0	-563	0
λ_3	-563	0	-565	0	-260	338	-258	342	-123	304	-74	313	-28	315	-6	314	4.88	313	7.01	312	8.94	313
λ_4	-255	339	-255	338	-260	-338	-258	-342	-123	-304	-74	-313	-28	-315	-6	-314	4.88	-313	7.01	-312	8.94	-313
λ_5	-255	-339	-255	-338	-243	260	-177	287	-256	341	-256	341	-255	340	-255	340	-255	340	-255	340	-255	339
λ_6	-0	0	-0	0	-243	-260	-177	-287	-256	-341	-256	-341	-255	-340	-255	-340	-255	-340	-255	-340	-255	-339
λ_7	-91	0	-127	0	-0	0	-0	0	-0	0	-0	0	0	0	-0	0	0	0	0	0	0	0
λ_8	-57	0	-91	0	-91	0	-91	0	-91	0	-91	0	-91	0	-91	0	-91	0	-91	0	-91	0
λ_9	-93	0	-93	0	-93	0	-93	0	-93	0	-93	0	-93	0	-93	0	-92.6	0	-93	0	-93	0

FIGURE 54 EIGENVALUE - ξ_{PLL} VARIATION

The instability of the system is found from the positive real values of λ_3 and λ_4 when ξ_{PLL} become less than or equal to 0.04 times its initial value.

Considering the result from **Figure 46**, another pair of eigenvalues moving toward left along the real part axis would represent the increasing overshoot and slower response of the system as ξ_{PLL} decreases.

5.2.6 ξ_V Variation

Figure 55 shows the change of ξ_V from 10 times to 0.2 times the $1/\sqrt{2}$, which is the initial set value.

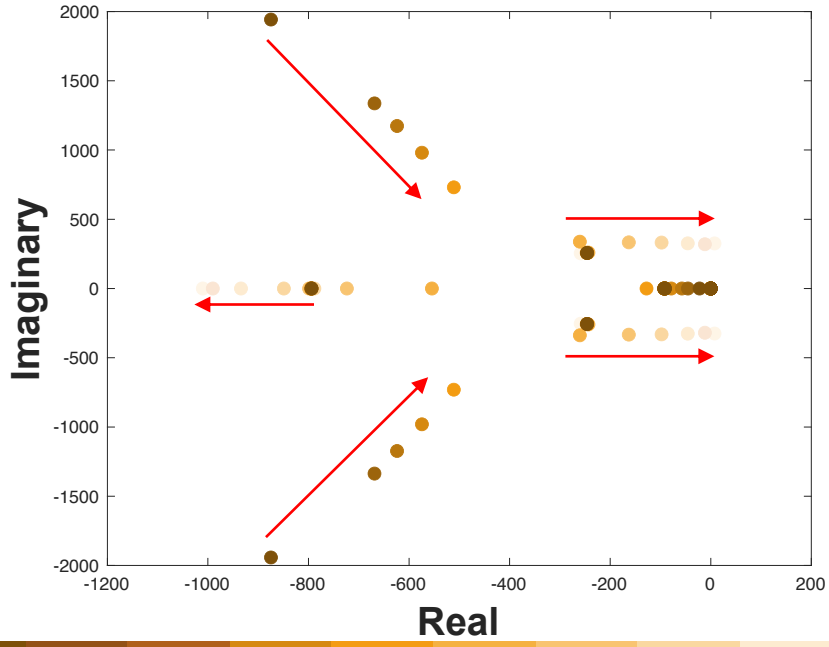

$1/\sqrt{2}$	x 10		x 5		x 4		x 3		x 2		x 1		x 0.8		x 0.6		x 0.4		x 0.25		x 0.2	
lambda	Re	Im	Re	Im	Re	Im	Re	Im	Re	Im	Re	Im	Re	Im	Re	Im	Re	Im	Re	Im	Re	Im
λ_1	-875	1942	-669	1336	-624	1173	-574	980	-794	0	-796	0	-799	0	-788	0	-792	0	-793	0	-1010	0
λ_2	-875	-1942	-669	-1336	-624	-1173	-574	-980	-511	731	-555	0	-724	0	-849	0	-934	0	-990	0	-795	0
λ_3	-794	0	-794	0	-794	0	-794	0	-511	-731	-260	338	-247	259	-247	257	-247	257	-247	257	-259	254
λ_4	-246	256	-246	256	-246	256	-246	256	-246	256	-260	-338	-247	-259	-247	-257	-247	-257	-247	-257	-259	-254
λ_5	-246	-256	-246	-256	-246	-256	-246	-256	-246	-256	-243	260	-163	333	-98	331	-46	326	-12	319	7.453	325
λ_6	0	0	-0	0	-0	0	-0	0	0	0	-243	-260	-163	-333	-98	-331	-46	-326	-12	-319	7.453	-325
λ_7	-22	0	-45	0	-57	0	-79	0	-128	0	-0	0	0	0	0	0	-0	0	0	0	0	0
λ_8	-91	0	-91	0	-91	0	-91	0	-91	0	-91	0	-91	0	-91	0	-91	0	-91	0	-90.5	0
λ_9	-93	0	-93	0	-93	0	-93	0	-93	0	-93	0	-93	0	-93	0	-93	0	-93	0	-92.6	0

FIGURE 55 EIGENVALUE - ξ_V VARIATION

First, it is obvious that the system becomes unstable when ξ_V less than or equal to 0.2 times the initial value of $1/\sqrt{2}$ by the pair of eigenvalues, λ_5 and λ_6.

Second, the movement of a pair of eigenvalues along the radial line to the direction which both the absolute values of the real and the imaginary parts decrease brings out slower response and oscillation for longer times.

Lastly, the movement of the poles to the left along the real part axis as means the decrease in overshoot, nevertheless the dynamic behavior when the damping ratio decreases brings out the increase of overshoot, which cannot be determined only by the results from **Figure 55**.

5.3 Bode Plot Analysis

Recalling **2.2.1**, the stability problems related to power electronics such as converters and inverters are classified as sub-synchronous resonance, near-synchronous resonance, and super-synchronous resonance, depending on the frequency of the oscillations. Super-synchronous resonance usually arises from the faster control loop such as an inner current loop or a phase-locked loop (PLL), and its frequency ranges from hundreds to ten thousand Hz. As in the case which the three-phase voltage or current system is dealt with, near-synchronous resonance occurs in slower control loop intended to control phaser quantities, active and reactive power control, or the frequency of the DC bus voltage, which are referred to as sub-synchronous oscillation (SSO) in dq −coordinate [25].

The composition of the unified state-space interconnecting all state-spaces shown in **Figure 32** is already presented in **Figure 49**. To represent the admittance on the Bode plot, a new state-space is needed whose desired input and output are selected as v_{qd}^{z} and i_{qd}^{c}, respectively, creating a transfer function of admittance, $H(j\omega)$.

When the frequency of the sine function waveform, which is the input signal, is changed, only the magnitude and phase of the steady-state output are changed. As such, a graph showing the magnitude and phase of the system transfer function with respect to the frequency of the sinusoidal input in the frequency domain is called a Bode plot.

In Bode plot, there are two y-axes, one is magnitude in log-scale of decibel (dB), whose definition is (74). The advantage of using log-scale is that the magnitude can be simply interpreted as a linear combination of terms of zero and pole.

$$\mathrm{L}_{dB} = 20 \cdot log_{10} H(j\omega) \tag{74}$$

The other is phase in degree (°) representing the phase difference between input and output. Lastly, the x-axis of Bode plot is plotted with the frequency ranging from $10^{-1}\ Hz$ to $10^{4}\ Hz$.

Compared to other methods such as Nyquist plot, the representation of characteristics of the system determined by zero and poles of the transfer function offers intuitive information needed for the design of active or passive filters by the combination of low pass, high pass, and band pass.

In this chapter, admittances of the VSC model are measured by the combinations of voltages and currents in qd −coordinate, which are inputs and outputs, respectively. They are to be named as Y_{qq}, Y_{qd}, Y_{dq}, and Y_{dd}.

$$\begin{aligned} Y_{qq} &= \frac{i_q^c}{v_q^z} \\ Y_{qd} &= \frac{i_d^c}{v_q^z} \\ Y_{dq} &= \frac{i_q^c}{v_d^z} \\ Y_{dd} &= \frac{i_d^c}{v_d^z} \end{aligned} \tag{75}$$

5.3.1 S_{sc} Variation

In Y_{qq}, the magnitude is constant, but starts to increase from a frequency region of $10\ Hz$ or higher to have a maximum magnitude around $320\ Hz$. As S_{sc} decreases, the value of the frequency reaching the maximum magnitude decreases. Similarly, the phase change in Y_{qq} keeps constant but become negative when frequency becomes larger than $10\ Hz$ implying the output i_q^c is lagging the input v_q^z.

Different from Y_{qq}, in case of Y_{qd}, Y_{dq}, and Y_{dd}, the frequency at which the magnitude has a maximum value increases as S_{sc} decreases from $100\ kVA$ to $50\ kVA$ and $10\ kVA$. Each of significant change of the phase in Y_{qd}, Y_{dq}, and Y_{dd} is at the frequency around $30\ Hz$, of which the phase difference has a maximum value.

As a consequence of **Figure 56**, Y_{qq} is the least affected while Y_{dq} is the most affected by the change in S_{sc}.

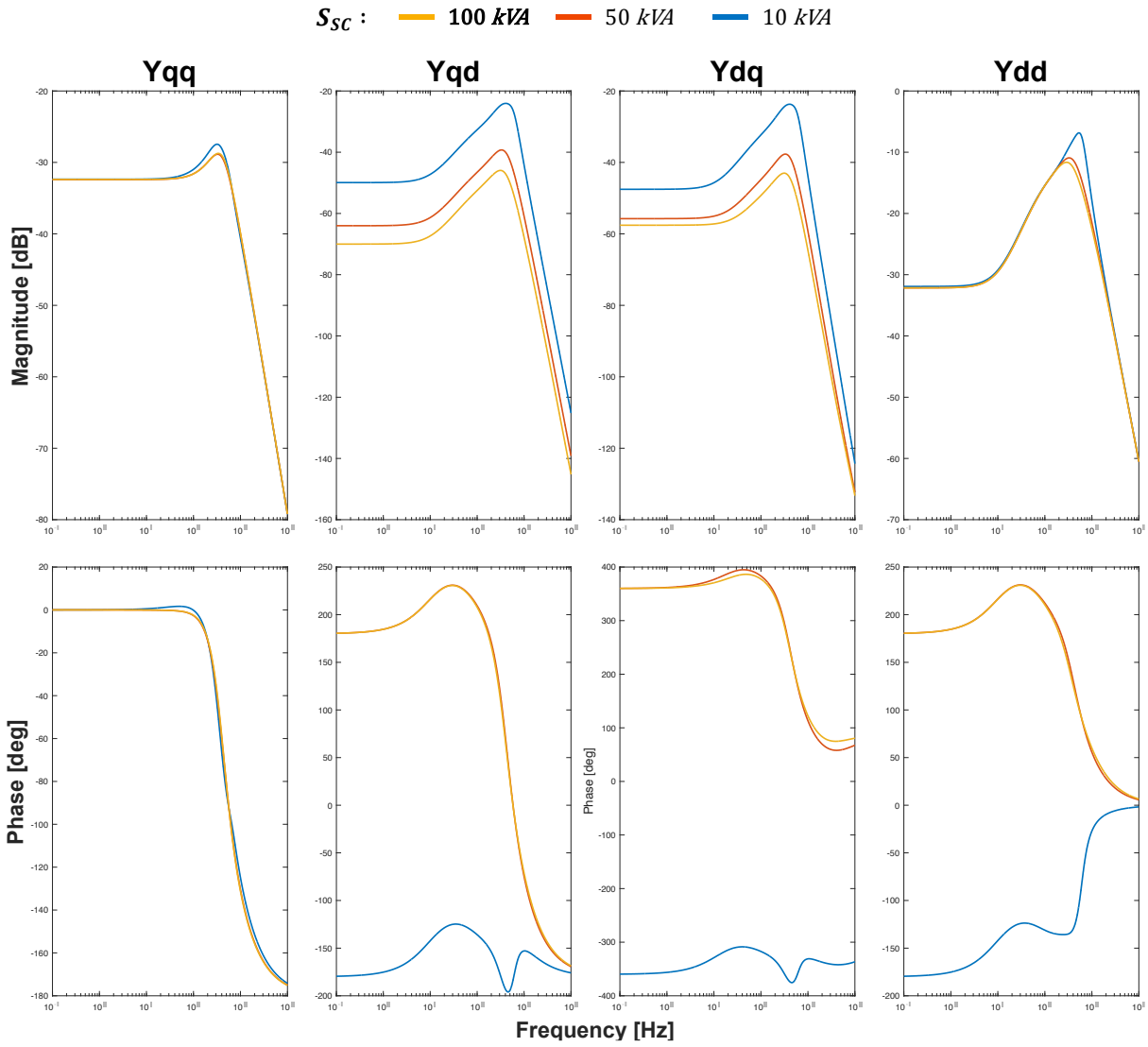

FIGURE 56 BODE PLOT - S_{sc} VARIATION

5.3.2 τ_{ic} Variation

The greater the value of τ_{ic}, the greater the peak value of both the magnitude and the phase. Also, as τ_{ic} increases, the value of the frequency reaching the maximum magnitude and phase becomes lower.

As τ_{ic} increases, it can be seen that the section of the frequency where the magnitude and the phase change become wider, requiring the consideration of dynamic responses of the system in wider range of frequencies.

The most drastic change in the magnitude and the phase is observed in Y_{dd}, whereas the most moderate change is observed in Y_{qq}.

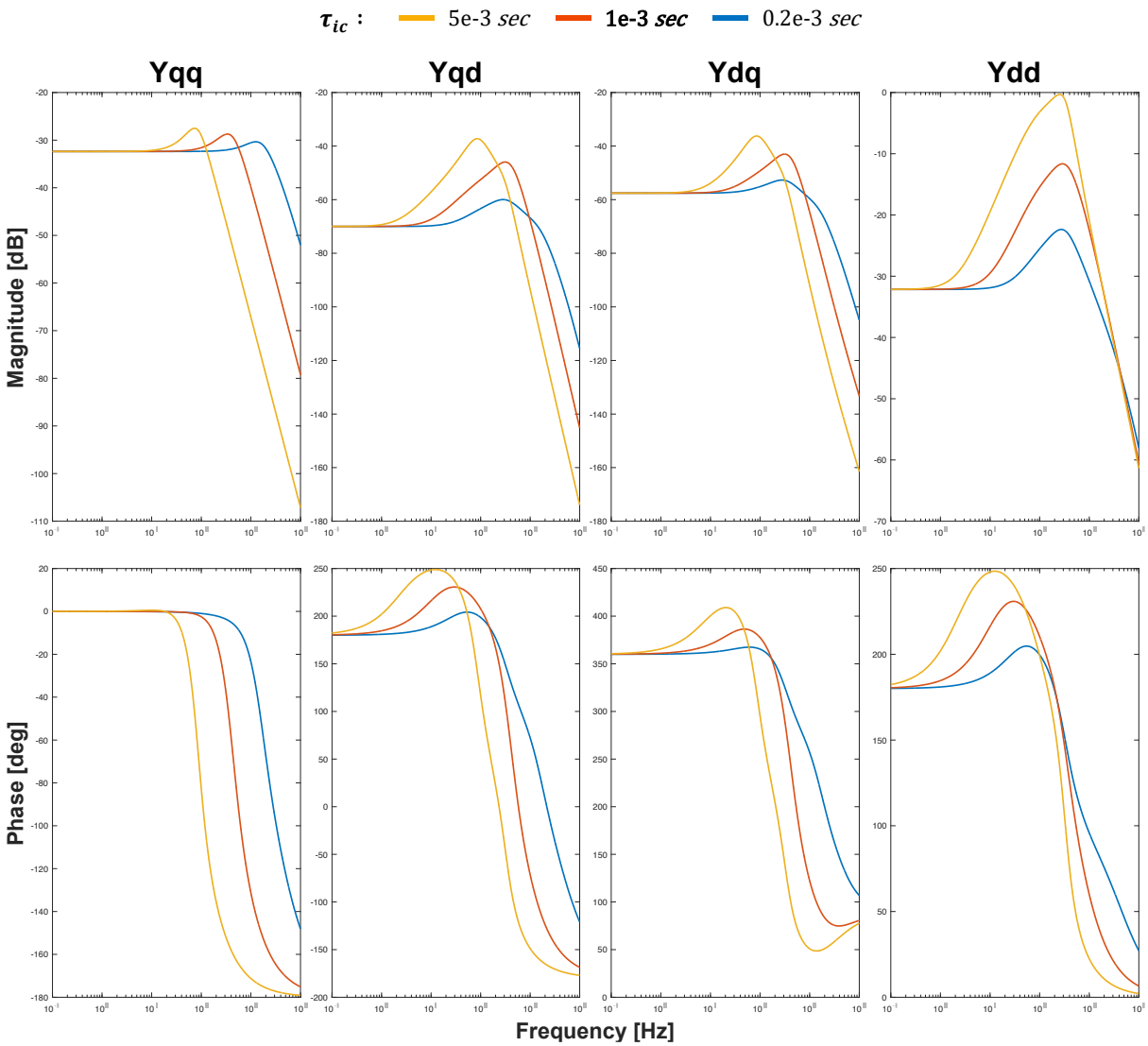

FIGURE 57 BODE PLOT - τ_{ic} VARIATION

5.3.3 ω_n Variation

In **Figure 58**, except for Y_{dq}, it is seen that the influence of the change in ω_n on the admittance is less noticeable than other parameters. Still, it is observed that the increase of ω_n brings out the increase of the maximum magnitude and phase as well as the frequency at which is the point.

Y_{dq} is showing quite a different response from other three. In the magnitude, the increase in frequency causes higher constant value at lower frequency range from $10^{-1}\ Hz$ to $10\ Hz$ and gentle slope at higher frequency from $300\ Hz$ to $10\ kHz$. Its phase difference become closer to $0°$ as ω_n differs.

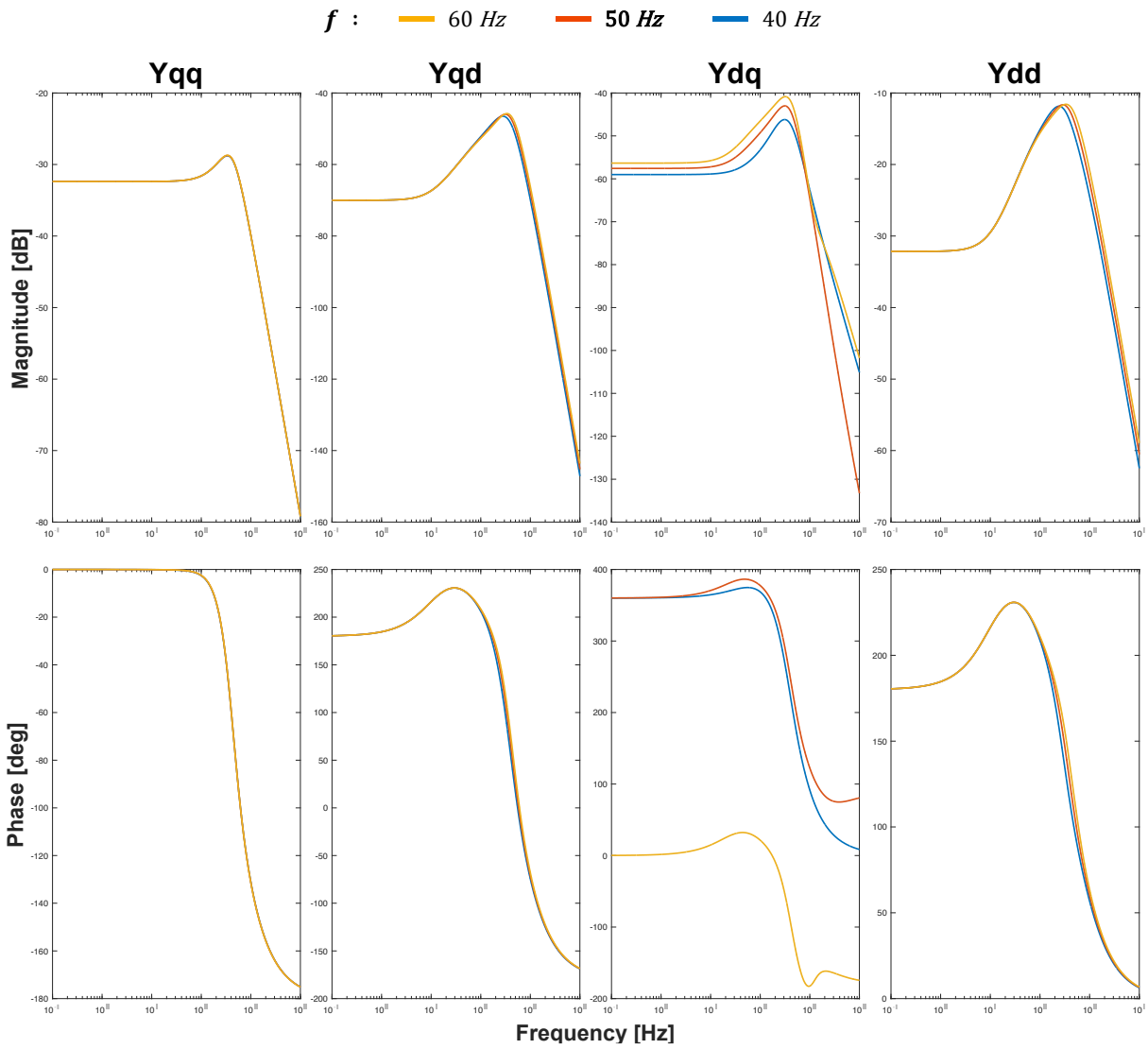

FIGURE 58 BODE PLOT - ω_n VARIATION

5.3.4 ω_V Variation

In **Figure 59**, it is firstly found that Y_{dd} is nearly affected by ω_V.

Looking into Y_{qq}, its responses of the magnitude and the phase keep in constant at lower frequency from $10^{-1}\ Hz$ to $20\ Hz$. In higher frequency range, the magnitude increases more rapidly until it reaches the peak, at which the frequency is higher as ω_V increases. After taking each of vertex, the magnitude of Y_{qq} decreases with almost equal slope, maintaining the difference between cases of different ω_V. When it comes to the phase change of Y_{qq}, it shows exponential response when α_V is 0.1 or 0.05. However, in case of $\alpha_V = 0.025$, the phase response shows a product of a linear function and an exponential function, $ax \cdot e^x$.

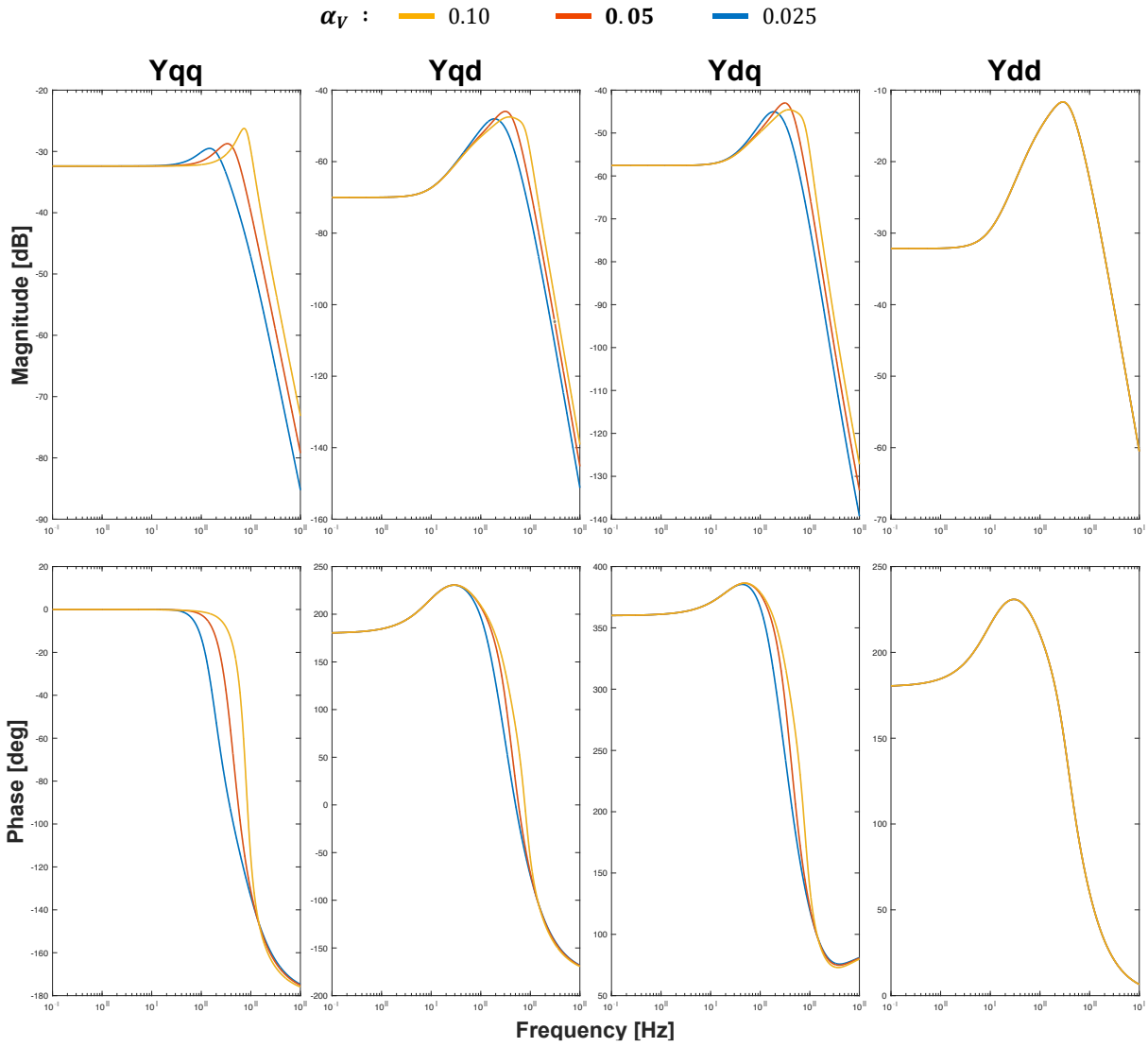

FIGURE 59 BODE PLOT - ω_V VARIATION

The trend of magnitudes found in the crossing terms of admittances Y_{qd} and Y_{dq} is that the frequency at which the peak magnitude exists becomes smaller as α_V decreases. The change of phases of Y_{qd} and Y_{dq} take the form of a product of a quadradic function and an exponential function, $ax^2 \cdot e^x$, while the average of the phase difference is larger when the value of α_V is larger.

5.3.5 ξ_{PLL} Variation

Figure 60 compares the system responses by bode plots of each admittance when ξ_{PLL} changes to 4 times and 0.25 times the initial value.

The change in Y_{qq} depending on the increase or decrease of ξ_{PLL} is the smallest. In the lower frequency from $10^{-1}\ Hz$ to $10\ Hz$, there is no variety of change in magnitudes. Different from Y_{qd}, Y_{dq}, and Y_{dd} which have larger peak values of magnitude when ξ_{PLL} is smaller, the larger the ξ_{PLL}, the larger the resonant peak in Y_{qq}.

In case of Y_{qd}, Y_{dq}, and Y_{dd}, the magnitudes increase until they reach each resonant peak at the frequency between $300\ Hz$ and $400\ Hz$. After the peak point, the smaller the ξ_{PLL}, the faster the magnitude decreases, and finally, in the higher frequency region of 400 Hz or higher, there is an intersection at frequency between $450\ Hz$ to $470\ Hz$ where the magnitude for the 4 times the initial value of ξ_{PLL} is the largest.

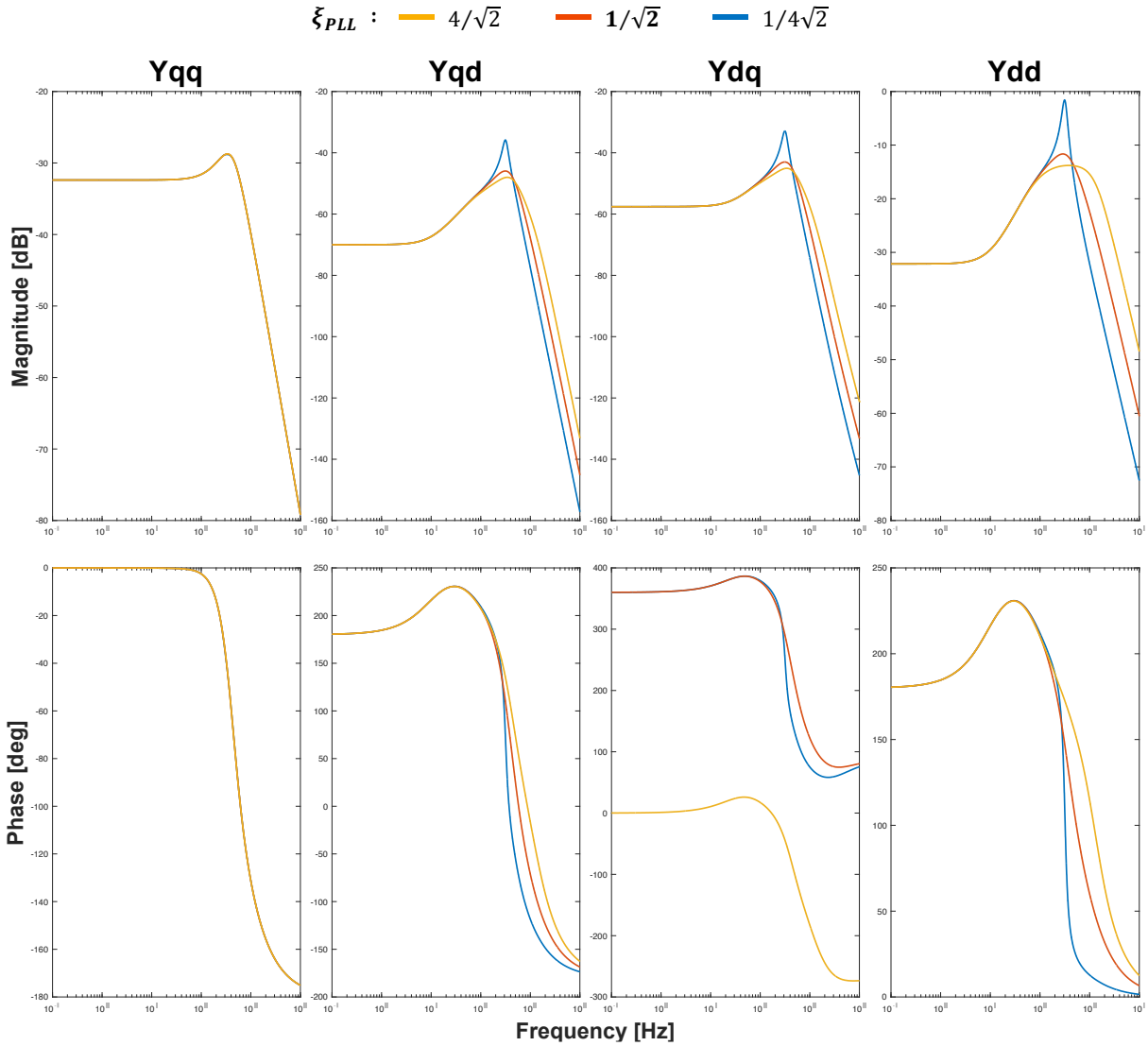

FIGURE 60 BODE PLOT - ξ_{PLL} VARIATION

The phase derivation of Y_{qq} is exactly the same regardless of the change in ξ_{PLL}. Also, in Y_{qd} and Y_{dd}, the larger ξ_{PLL} increases the phase, whereas in Y_{dq}, the smaller ξ_{PLL} increases the phase.

5.3.6 ξ_V Variation

In **Figure 61**, different from the case of ξ_{PLL}, Y_{dd} is the least affected by ξ_V showing very small derivative of magnitude and no change in phase derivation. Still, each magnitude keeps constant at lower frequency and starts to increase until it come to the peak point, and then, starts decreasing.

The resonant peaks of magnitude and phase is larger as ξ_V is smaller in all admittances. After the peak point, the smaller the ξ_V, the faster the magnitude decreases, so the order of the magnitude values according to ξ_V is reversed.

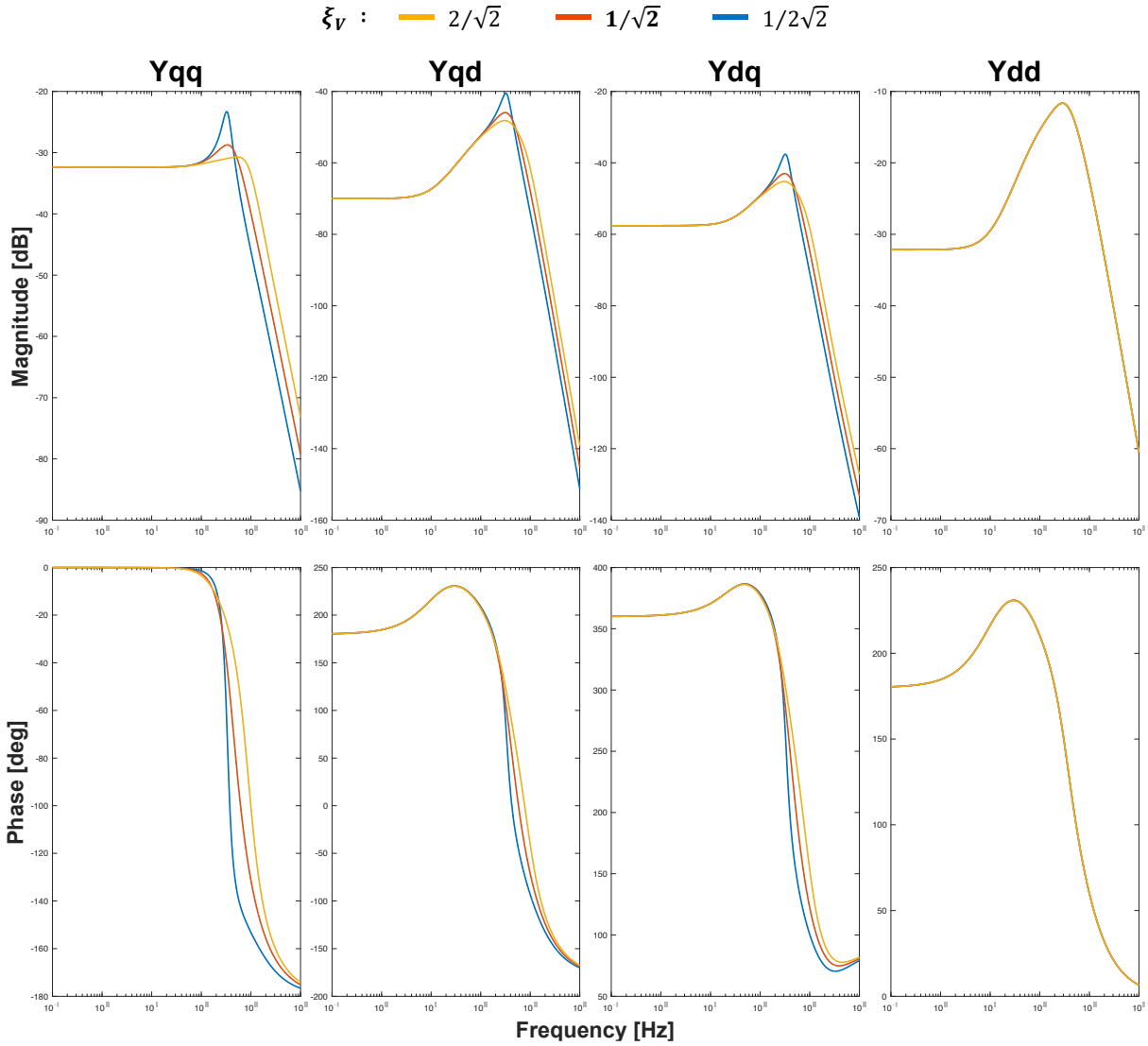

FIGURE 61 BODE PLOT - ξ_V VARIATION

A common finding in the phase change of the four admittances is that the smaller ξ_V is, the larger the peak value of the phase is.

The phase of Y_{qq} is constant in lower frequency from $10^{-1}\,Hz$ to $30\,Hz$ and then it decreases in exponential form. At the admittances Y_{qd} and Y_{dq}, a phase change is detected over all frequency ranges.

6. Conclusion

6.1 Review of the case studies

The results of **5.1** show how the control parameters affect the control of currents and voltages of the designed VSC model and represent how the system could be analyzed based on the consideration of the impact of the integral and the proportional factor of a PI controller on the response of oscillations of currents and voltages of the system.

In **5.2**, the changes of eigenvalues with respect to the change in each parameter are investigated. The transition of eigenvalues manifests the stability of the system, finding the instability cases with the decrease in the value of each parameter, S_{SC}, ω_V, ξ_{PLL}, and ξ_{PLL}. Although no stability issues have been found with the respect to the observed range of ω_n, the movement of the two eigenvalues towards the imaginary axis suggest the possibility of them to have positive real part, which implies the instability of the system. However, τ_{ic} is the only parameter to be concluded that it does not affect the stability when considering the movements of all eigenvalues heading to the left or upward, bringing out more rapid damping with larger overshoot.

In **5.3**, the impedance-based representation of the system was analyzed through the Bode plot showing the magnitude and the phase change of admittances with frequency. The system response was analyzed by dividing the section into three frequency ranges. The focus was on which frequencies the magnitude and the phase have their maximum values and how the magnitude and the phase are affected when each parameter increases and decreases. Notable changes occurred mainly in the cross terms, Y_{qd} and Y_{dq}, except for τ_{ic} in which all four admittance changes were clearly visible. For example, there were little change in Y_{qq} regardless of the increase or the decrease of ω_n and ξ_{PLL}, while little change in Y_{dd} was found for the variation of ω_V and ξ_V. Another finding from the results is that the magnitude of admittance is greater as S_{SC}, ξ_{PLL}, and ξ_V are small, and τ_{ic}, ω_n, and ω_V are large.

6.2 Completion and Discussion

The eigenvalue analysis, or the root locus analysis tracking the movement of eigenvalues for the stability analysis, has proved its simplicity and feasibility as a tool to analyze the impact of the designed VSC model on the grid. Nevertheless, the need for detailed design specifications of the controller is still a big disadvantage considering the current industry situation presented in **1.2**.

In this Master thesis, the designs of the VSC models are based on the d-q domain and so does the impedance-based analysis. It has often been thought that d-q Impedance method has the disadvantage that Nyquist criterion for a Single-Input Single-Output (SISO) system and bode plots cannot be used for the stability analysis of three-phase AC systems [25], which can be overcome with symmetric systems using a complex representation.

Therefore, by modeling the linear model with the state-space method, stated in **4.2**, the disadvantage of d-q domain model has been eliminated, while maintaining its advantage of supporting a Multi-Input Multi-Output (MIMO) system. In other words, the applied method meets the purpose of presenting a reliable data-driven stability analysis method in power systems without detailed design specifications of power electronics by regarding subsystems as a black-box which does not require for any knowledge on control parameters.

Also, the results have proved obviously that impedance-based analysis is useful enough to deal with the grid stability problem related to high levels of power electronics, due to its easiness to observe the derivatives of magnitude and phase in relation to voltage and current with respect to a wide range of frequencies just in a single plot as well as the convenience of the measurement of voltages and currents at any point to be inspected by power system operators.

Nevertheless, neither the eigenvalue analysis nor the impedance-based representation in this master thesis do not provide information about which and how much each state variable of the control system affects the system when its step variation is given. The investigation of the participation factors can supplement such a problem. Also, the perfect design should consider the effects of the modulation process to convert DC to AC producing

harmonics and imperfect sinusoidal waveshapes which affect the result of the stability analysis. However, the significance of the master thesis lies on proving the validity of the impedance-based stability analysis in the industrial field by presenting the procedure for designing the average VSC model and comparing its results with the impedance-based analysis and the eigenvalue analysis.

Bibliography

[1] Adrian Whiteman, Dennis Akande, Nazik Elhassan, Gerardo Escamilla, Arvydas Lebedys, and Iana ArkhipovaIrene. "Renewable Capacity Statistics 2021,"(PDF). IRENE, Abu Dhabi, 2021, ISBN 978-92-9260-342-7

[2] G. Venkataramanan and C. Marnay, "A larger role for microgrids," in IEEE Power and Energy Magazine, vol. 6, no. 3, pp. 78-82, May-June 2008, doi: 10.1109/MPE.2008.918720.

[3] B. Kroposki, R. Lasseter, T. Ise, S. Morozumi, S. Papathanassiou and N. Hatziargyriou, "Making microgrids work," in IEEE Power and Energy Magazine, vol. 6, no. 3, pp. 40-53, May-June 2008, doi: 10.1109/MPE.2008.918718.

[4] S. Shah, P. Koralewicz, V. Gevorgian, H. Liu and J. Fu, "Impedance Methods for Analyzing Stability Impacts of Inverter-Based Resources: Stability Analysis Tools for Modern Power Systems," in IEEE Electrification Magazine, vol. 9, no. 1, pp. 59, March 2021, doi: 10.1109/MELE.2020.3047166.

[5] Ortiz L., Orizondo R., Águila A., González J. W., López G. J. & Isaac I., "Hybrid AC/DC microgrid test system simulation: grid-connected mode," Heliyon, vol. 5, no. 12, pp. 21, 2019, doi: 10.1016/j.heliyon.2019.e02862

[6] Stamatiou Georgios, Techno-Economical Analysis of DC Collection Grid for Offshore Wind Parks, MSc Thesis, The University of Nottingham, Sep 2010, doi: 10.13140/RG.2.1.1902.6649.

[7] J. Pan, R. Nuqui, K. Srivastava, T. Jonsson, P. Holmberg and Y. Hafner, "AC Grid with Embedded VSC-HVDC for Secure and Efficient Power Delivery," 2008 IEEE Energy 2030 Conference, 2008, pp. 1-6, doi: 10.1109/ENERGY.2008.4781042.

[8] M. Cheah-Mane, J. Song, R. Ferrer-San-Jose, E. Prieto-Araujo and O. Gomis-Bellmunt, "Analysis of hybrid LCC-VSC HVDC transmission system configurations," 15th IET International Conference on AC and DC Power Transmission (ACDC 2019), 2019, pp. 1-6, doi: 10.1049/cp.2019.0071.

[9] Grigsby, L.L., "Power System Stability and Control," 3rd Ed, CRC Press, Ch.8, pp. 7-9, 2012, doi.org/10.4324/b12113

[10] Hatziargyriou, Nikos D., Jovica V. Milanović, Claudia Rahmann, Venkataramana Ajjarapu, Claudio A. Cañizares, István Erlich, David. J. Hill, Ian A. Hiskens, I. Kamwa, Bikash Chandra Pal, Pouyan Pourbeik, J. Gasca, Alexander M. Stankovic, Thierry Van Cutsem, Vijay Vittal and Costas D. Vournas. "Stability definitions and characterization of dynamic behavior in systems with high penetration of power electronic interfaced technologies." in IEEE Power System Dynamic Performance (PSDP) Committee, Apr 2020.

[11] Grigsby, L.L., "Power System Stability and Control," 3rd Ed, CRC Press, 2012, Ch.8, pp. 3, doi.org/10.4324/b12113

[12] J. Sun, "Small-signal methods for AC distributed power systems– a review," *IEEE Trans. Power Electron*., Nov. 2009, vol. 24, pp. 2545-2554.

[13] S. Shah, et el, "Impedance Methods for Analyzing Stability Impacts of Inverter-Based Resources: Stability Analysis Tools for Modern Power Systems," (PDF), NREL, NSF Workshop, Chicago, Illinois, 31st Oct – 1st Nov 2019

[14] Shahil Shah, Przemyslaw Koralewicz, Vahan Gevorgian, and Robb Wallen, "Impedance Measurement of Wind Turbines Using a Multimegawatt Grid Simulator,"(PDF) 18th Wind Integration Workshop, Oct 16-18 2019, NREL/CP-5D00-74890

[15] Middlebrook, R., "Input filter considerations in design and application of switching regulators", 1976

[16] M. Belkhayat, "Stability criteria for ac power systems with regulated loads." Ph. D. dissertation. Purdue Univ., West Lafayette, IN, USA, Dec. 1997.

[17] J. Sun and H. Liu, "Sequence Impedance Modeling of Modular Multilevel Converters," in IEEE Journal of Emerging and Selected Topics in Power Electronics, vol. 5, no. 4, pp. 1427-1443, Dec. 2017, doi: 10.1109/JESTPE.2017.2762408.

[18] S. Shah and L. Parsa, "Small-signal modeling of single-phase PLLs using harmonic signal-flow graphs," 2017 IEEE Energy Conversion Congress and Exposition (ECCE), 2017, pp. 4989-4995, doi: 10.1109/ECCE.2017.8096844.

[19] Ghimire, Santosh & Alizadeh, Seyed, "Developing a Decision Tree Algorithm for Wind Power Plants Siting and Sizing in Distribution Networks," Energies. 14. 2293 doi: 10.3390/EN14082293.

[20] Se-Kyo Chung, "A phase tracking system for three phase utility interface inverters" in IEEE Transactions on Power Electronics, vol.15, no.3, pp.431-438, May 2000

[21] P. Kundur, “Power System Stability and Control,” McGraw- Hill, New York, Ch.2, pp. 707-709, 1994.

[22] Kiam Heong Ang; Chong, G.; Yun Li (2005). "PID control system analysis, design, and technology," (PDF). IEEE Transactions on Control Systems Technology. 13 (4): 559–576. doi:10.1109/TCST.2005.847331. S2CID 921620.

[23] Jinghua Zhong (Spring 2006). "PID Controller Tuning : A Short Tutorial"

[24] Obando, Larry Francis, ed. “UNDERDAMPED SECOND-ORDER SYSTEM.” dademuchconnection, Figure 4.11, Nov 14, 2017. https://dademuch.com/category/matematica-aplicada-appd-math/page/5/.

[25] S. Shah, P. Koralewicz, V. Gevorgian, H. Liu and J. Fu, "Impedance Methods for Analyzing Stability Impacts of Inverter-Based Resources: Stability Analysis Tools for Modern Power Systems," in IEEE Electrification Magazine, vol. 9, no. 1, pp. 54-56, March 2021, doi: 10.1109/MELE.2020.3047166.

Appendix

Clarke Transformation

The Clarke transformation is to be used to simplify the analysis of three-phase circuits by transforming abc to $\alpha\beta 0$ frame, which is defined as

$$[x_{\alpha\beta 0}] = [T_{\alpha\beta 0}][x_{abc}] \tag{1}$$

$$[x_{abc}] = [T_{\alpha\beta 0}]^{-1}[x_{\alpha\beta 0}] \tag{2}$$

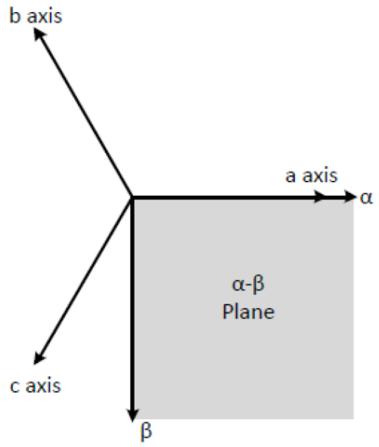

FIGURE 1 CLARKE TRANSFORMATION

The example of the balanced three-phase system with its amplitude of the admitted peak voltage applied in the grid model, $E_m = \frac{\sqrt{2}}{\sqrt{3}} \cdot 400 \approx 325$, is shown as

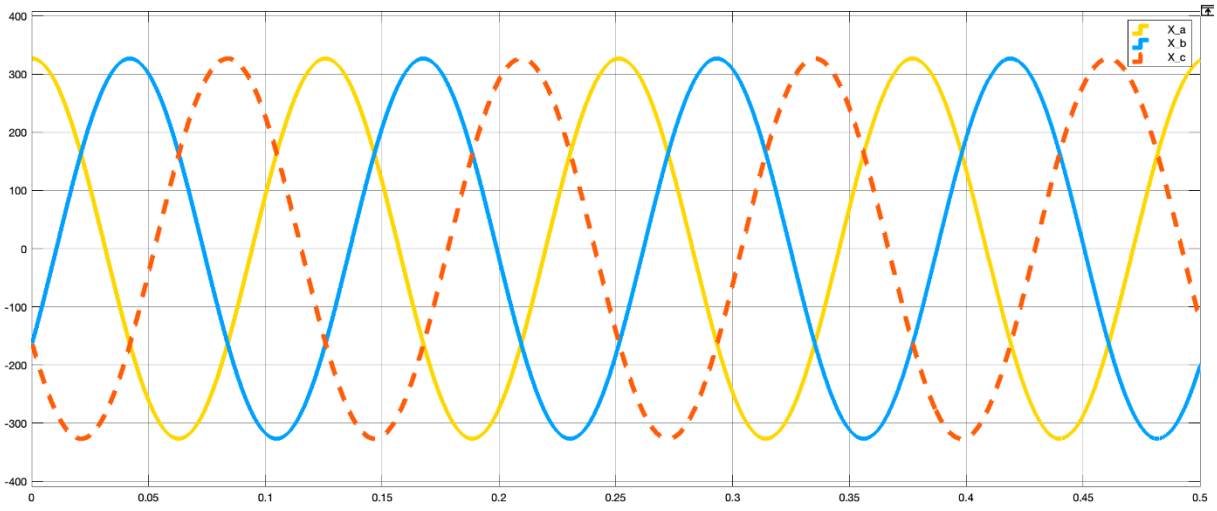

FIGURE 2 THE BALANCED THREE-PHASE SYSTEM

The expressions of the Clarke transformation can be written as

$$[x_{\alpha\beta 0}] = [K_C] \cdot [x_{abc}] \quad \leftrightarrow \quad \begin{bmatrix} x_\alpha \\ x_\beta \\ x_0 \end{bmatrix} = \begin{bmatrix} \frac{2}{3} & -\frac{1}{3} & -\frac{1}{3} \\ 0 & -\frac{1}{\sqrt{3}} & \frac{1}{\sqrt{3}} \\ \frac{1}{3} & \frac{1}{3} & \frac{1}{3} \end{bmatrix} \begin{bmatrix} x_a \\ x_c \\ x_c \end{bmatrix} \tag{3}$$

$$[x_{abc}] = [K_C]^{-1} \cdot [x_{\alpha\beta 0}] \quad \leftrightarrow \quad \begin{bmatrix} x_a \\ x_b \\ x_c \end{bmatrix} = \begin{bmatrix} 1 & 0 & 1 \\ -\frac{1}{2} & -\frac{\sqrt{3}}{2} & 1 \\ -\frac{1}{2} & \frac{\sqrt{3}}{2} & 1 \end{bmatrix} \begin{bmatrix} x_\alpha \\ x_\beta \\ x_0 \end{bmatrix} \tag{4}$$

where x_a, x_b, x_c is the instantaneous values of voltage or current in the abc frame and x_α, x_β, x_0 are the transformed quantities of abc in the $\alpha\beta 0$ frame.

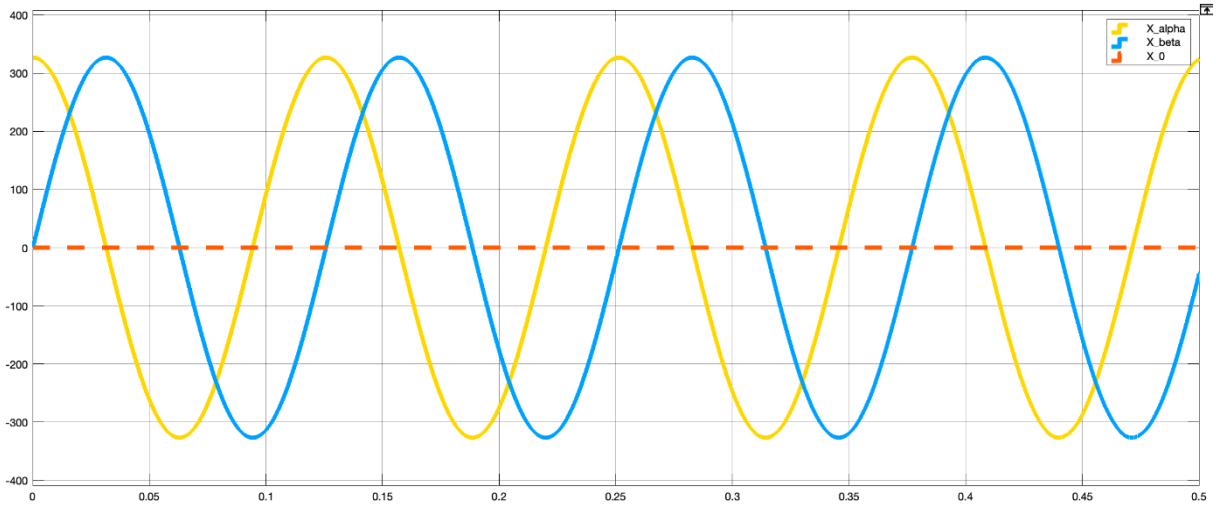

FIGURE 3 CLARKE TRANSFORMATION OF THE BALANCED THREE-PHASE SYSTEM

Park Transformation

For the controller design, the Park transformation is useful, by transforming vectors in stationary reference $\alpha\beta 0$ −frame to constant quantities in rotating reference $qd0$ −frame.

$$\begin{aligned}\left[x_{qd0}\right] &= [K_P][x_{\alpha\beta 0}] \\ \left[x_{\alpha\beta 0}\right] &= [K_P]^{-1}[x_{qd0}]\end{aligned} \tag{5}$$

The rotation matrix of the angle θ for the alignment of an α −reference to q −axis is expressed as

$$[K_P] = \begin{bmatrix}\cos(\theta) & -\sin(\theta) & 0 \\ \sin(\theta) & \cos(\theta) & 0 \\ 0 & 0 & 1\end{bmatrix} \tag{6}$$

and its geometric representation is

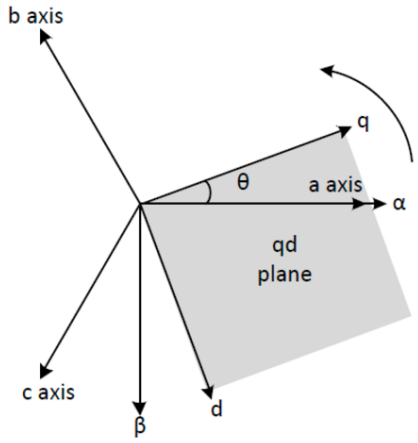

FIGURE 4 PARK TRANSFORMATION BY $\boldsymbol{q}$ −AXIS ALIGNMENT

The combination matrix of the Clarke and the Park transformation $T(\theta)$ can be written as

$$T(\theta) = \frac{2}{3}\begin{bmatrix}\cos(\theta) & \cos\left(\theta - \frac{2\pi}{3}\right) & \cos\left(\theta + \frac{2\pi}{3}\right) \\ \sin(\theta) & \sin\left(\theta - \frac{2\pi}{3}\right) & \sin\left(\theta + \frac{2\pi}{3}\right) \\ \frac{1}{2} & \frac{1}{2} & \frac{1}{2}\end{bmatrix} \tag{7}$$

And the inverse matrix, $T^{-1}(\theta)$ is represented as

$$T^{-1}(\theta) = \begin{bmatrix}\cos(\theta) & \sin(\theta) & 1 \\ \cos\left(\theta - \frac{2\pi}{3}\right) & \sin\left(\theta - \frac{2\pi}{3}\right) & 1 \\ \cos\left(\theta + \frac{2\pi}{3}\right) & \sin\left(\theta + \frac{2\pi}{3}\right) & 1\end{bmatrix}\begin{bmatrix}x_\alpha \\ x_\beta \\ x_0\end{bmatrix} \tag{8}$$

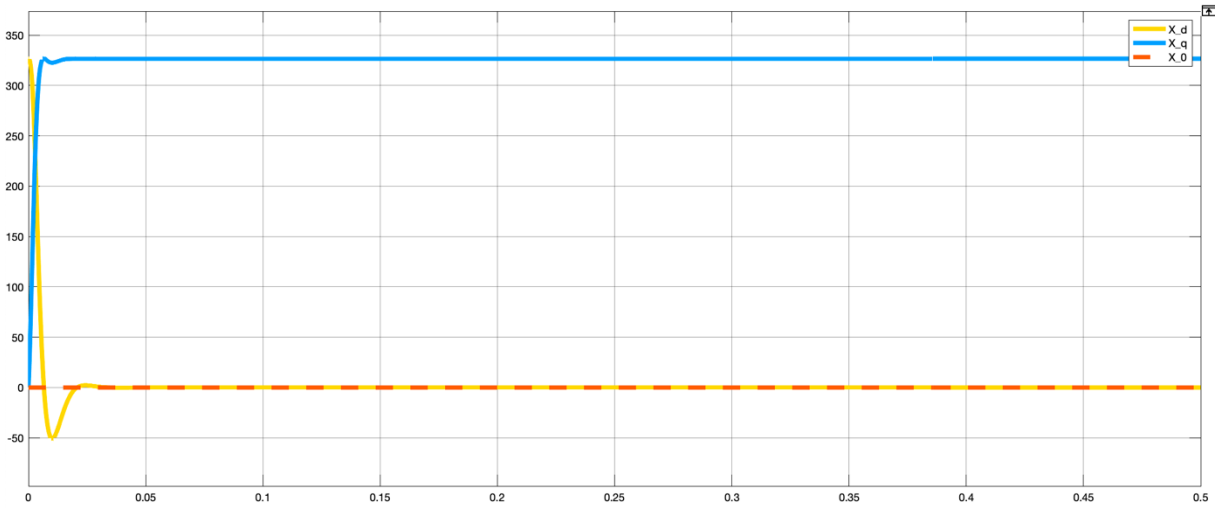

FIGURE 5 TRANSFORMATION BY $\boldsymbol{T(\theta)}$ OF THE BALANCED THREE-PHASE SYSTEM